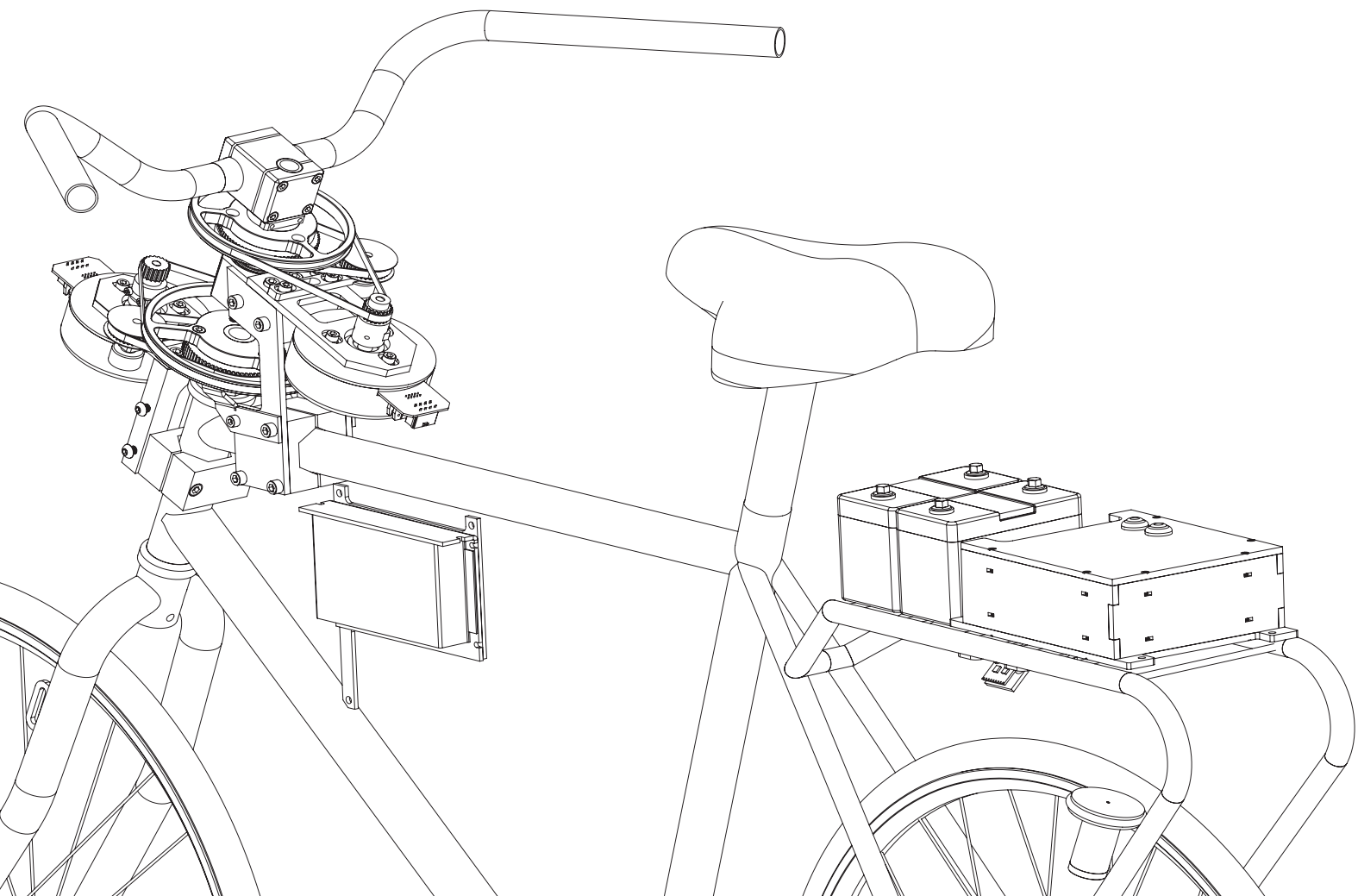


Department of Precision and Microsystems Engineering

Dynamics and Control of a Steer-by-Wire Bicycle

N. Appelman

Report no : MSD 2012.029
Coach : Dr. Ir. A.L. Schwab
Professor : Prof. Ir. R.H. Munnig Schmidt
Specialisation : Mechatronic System Design
Type of report : Master of Science Thesis
Date : 27 November 2012



Dynamics and Control of a Steer-by-Wire Bicycle

Lateral Stability Enhancement
for Application on Bicycles

N. Appelman

Master of Science Thesis

Dynamics and Control of a Steer-by-Wire Bicycle

Lateral Stability Enhancement for Application on Bicycles

MASTER OF SCIENCE THESIS

For the degree of Master of Science in Mechanical Engineering at Delft
University of Technology

N. Appelman

November 27, 2012

Faculty of Mechanical, Maritime and Materials Engineering (3mE)
Delft University of Technology



Copyright © Precision and Microsystems Engineering - Mechatronic System Design
All rights reserved.

Abstract

Already for some time, electronic enhancements regarding vehicle behavior has made its way into the aviation and automotive industry by the term "by-wire" technology. Electronic sensors and actuators are used to replace traditional mechanical systems in which software is used to operate the actuators in a way that is not possible with traditional mechanical systems.

The use of steer-by-wire technology can also offer great opportunities on single-track vehicles like motorcycles, scooters and bicycles. Single-track vehicles can be highly unstable, especially at low forward speeds and they require a relative high amount of rider control. By replacing the mechanical connection between the handlebar- and steering-assembly with electronic actuators, a controller can be used to control the dynamic behavior of the bicycle based on additional sensor information.

This research has focused on the modeling and simulation of a steer-by-wire control strategy to modify and enhance the lateral stability of a bicycle at low forward speeds. Case studies show additional capabilities of a steer-by-wire system on bicycles to influence its dynamic behavior, by providing a dynamic response comparable to a bicycle with a virtually different geometry or even the ability to stabilize an inherently unstable bicycle. A steer-by-wire bicycle prototype was designed and build by replacement of the mechanical connection between handlebar- and steering-assembly by electronic actuators and a custom digital controller. The steer-by-wire bicycle prototype equipped with sensors, measuring the forward speed- and roll-rate is subsequently used to experimentally evaluate the proposed control algorithms.

Test results obtained from experiments conducted by the steer-by-wire bicycle prototype equipped with a stabilizing controller algorithm, show the ability to stabilize the lateral motion of the bicycle-rider combination at low forward speeds as predicted by numerical simulations. Rider steer effort is reduced which makes the bicycle more easy to ride and could lead to future implementation on bicycles tailored for elderly or those physically impaired. The importance of steer torque feedback is indicated by comparison of steer effort measurement results between experiments with and without steer torque feedback at the handlebar.

Table of Contents

Preface	v
1 Introduction	1
1-1 Steer-by-Wire on Bicycles?	1
1-2 Report Structure	2
2 The Concept of Steer-by-Wire	3
2-1 Brief Historical Overview	3
2-1-1 Aviation industry	3
2-1-2 Automotive industry	4
2-2 Steer-by-Wire and Single-Track Vehicles	5
2-3 Steer-by-Wire Bicycle	6
2-4 Summary	9
3 Bicycle Modeling	11
3-1 Benchmark Bicycle model	11
3-2 Steer-by-Wire Bicycle model	14
3-3 Summary	17
4 System Modeling and Simulation	19
4-1 Controllability	20
4-2 Handlebar Tracking	21
4-3 Lateral Stability Enhancement	25
4-3-1 Low Speed Stabilization	26
4-4 Pole Placement	27
4-4-1 Virtual Head Angle Bicycle	30
4-4-2 Stable Backwards Bicycle	32
4-5 Steer Torque Feedback	34
4-6 Summary	37

5 Steer-by-Wire Implementation	39
5-1 Software	41
5-1-1 Development tool selection	41
5-2 Electronics	42
5-2-1 Controller selection	42
5-2-2 IO-board design	45
5-2-3 Power source selection	49
5-3 Electromechanics	50
5-3-1 Sensor selection	50
5-3-2 Actuator selection	59
5-4 Firmware	69
5-4-1 Principal Control structure	70
5-4-2 Auxiliary Control structure	71
5-5 Summary	72
6 Experimental Tests	73
6-1 Steer Torque Feedback Steer-by-Wire Bicycle	73
6-2 Low Speed Stabilization	74
6-2-1 Test procedure	75
6-2-2 Data analysis	76
6-3 Self Stability	87
6-4 Summary	87
7 Conclusions and Recommendations	89
7-1 Conclusions	89
7-1-1 Vehicle dynamics	89
7-1-2 Bicycle-rider interaction	90
7-2 Recommendations	90
7-2-1 Vehicle dynamics research	91
7-2-2 Bicycle-rider interaction research	91
7-2-3 Prototype improvements	91
Bibliography	93
A Steer-by-wire bicycle component layout	95
B Electronic circuit layout	97
B-1 IO-board circuit layout	97
B-2 Power-wiring layout	100
B-3 Sensor-wiring layout	101
C Component specifications	105
D CAD drawings	113
E Simulink firmware function-block layout	125

Preface

In front of you lies the work which finishes an important part of my life, and to be able to finish my education with the design and actual realization of a true mechatronic prototype is something I had never expected to do, but always hoped for. Mechanics and electronics both has fascinated me from the very beginning and to be in the position to combine those fields of interest with a practical application on bicycles, makes it a wonderful experience. The perspective of being able to apply a new technology in a highly conservative field of application, caused me to take up the challenge of developing a steer-by-wire bicycle prototype at the Bicycle Lab of the TU Delft.

The actual realization of a functional prototype was a challenge in itself, as unforeseen issues always tend to upset a previously devised approach. However, the ample freedom I received during this project has been a great contribution to translate my views, ideas and theory into something tangible which can potentially change our notion of single-track vehicles in the near future.

Along the way I have received help from people all around me, who gave their advice and shared their views and experience. First and foremost I would like to thank my supervisor Dr.Ir. Arend L. Schwab for guiding me trough the whole process, sharing his sound knowledge, experience and endless enthusiasm in the field of bicycle dynamics and in particular this steer-by-wire bicycle project. I would like to thank Dr.Ir. Jodi D.G. Kooijman for his valuable support, enthusiasm and kind presence at the TU Delft Bicycle Lab as well as the other (visiting) lab members with whom we have shared great moments together. At the TU Delft workshop a big thanks to Ing. Jan van Frankenhuyzen, Andries Oort and René van der Schuur for their support during construction of the steer-by-wire bicycle prototype.

A special mention to Lubin Kerhuel who kindly provided a license-copy of the firmware development software, as well as Super-B who provided the Lithium-Ion batteries to power the steer-by-wire bicycle prototype.

A special thanks goes out to my parents for their patience and support during my study and additional years of extracurricular activities at the university, which has contributed greatly in my personal- and professional development in becoming a mechanical engineer.

Chapter 1

Introduction

1-1 Steer-by-Wire on Bicycles?

Modern electronic control systems have made a big impact in recent decades, especially in the aviation and automotive industry. Aircraft equipped with computer controlled autopilots have changed the way pilots were used to fly. Vehicle safety systems have become more important since passenger cars are being equipped with safety features like airbags, anti-lock brakes and electronic stability control systems. These electronic systems have increased safety, comfort, performance, design freedom, reliability and has reduced manufacturing costs.

Electronic enhancements regarding vehicle behavior have made its way into the aviation and automotive industry by the term 'by-wire' technology. It covers technology like fly-by-wire, drive-by-wire, brake-by-wire and steer-by-wire. Electronic sensors and actuators are used to replace traditional mechanical systems, and software running on a controller is used to operate the actuators in a way that is not possible with traditional mechanical systems. As this technology is already widely used in aviation and emerging in the automotive industry, the application of steer-by-wire technology also offers great opportunities on single-track vehicles like motorcycles, scooters and bicycles.

The dynamic behavior of single-track vehicles like bicycles depends on mass- and geometrical-properties as well as the forward speed of the bicycle. At low forward speeds the dynamic behavior can be highly unstable. By actuating on the two main degrees of freedom defined by the steer- and roll-angle of the bicycle, the (unstable) dynamic behavior can be influenced which we probably all know from experience by turning the handlebars or leaning the bicycle in a turn. Implementing by-wire technology on bicycles makes it possible to control its dynamic behavior by actuating on the steer angle of the bicycle with the use of an actuator connected to the steering assembly. A true advantage of a steer-by-wire system is undoubtedly the mechanical decoupling of the handlebar- and steering assembly which allows for scalable control input between the rider and controller. The application of a steer-by-wire system and the benefits this technology can provide is not strictly preserved to bicycles. Larger single-track vehicles like motorcycles and scooters can also benefit from the advantages this technology offers.

In scientific literature, no experimental research is known which actually evaluates a steer-by-wire system on single-track vehicles other than a few theoretical publications proposing enhancements in motorcycle handling [Marumo and Nagai, 2007] [Katagiri et al., 2009]. Small and light vehicles like bicycles are highly suitable for experimental research of steer-by-wire technology on single-track vehicles, as the power- and torque requirements remain relatively low and theoretical models are able to closely predict the uncontrolled dynamic behavior [Meijaard et al., 2007].

This report describes the design and actual implementation of a steer-by-wire system on bicycles with the focus on improvement of the lateral stability. The recent trend observed in the bicycle industry by the addition of an electric motor and batteries to assist the driver by providing an additional peddling torque, makes it a perfect platform for future integration of steer-by-wire technology on bicycles.

1-2 Report Structure

This report is structured by a small introduction given in chapter 2 which gives a brief historical background on steer-by-wire technology. Chapter 3 introduces a recent bicycle model expanded with an additional degree-of-freedom to allow for a mechanically decoupled handlebar assembly. System modeling and time simulations in chapter 4 cover various control strategies to enhance the lateral stability of the bicycle, as well as strategies to provide the bicycle with a different virtual geometry and stabilization of a backwards driven bicycle. The design and construction of the steer-by-wire bicycle prototype is covered in chapter 5, followed by experimental tests in chapter 6 to evaluate the control algorithms covered previously. To conclude this report, research findings, conclusions and recommendations for future research are given in chapter 7.

The Concept of Steer-by-Wire

In the following section a more detailed view is given on steer-by-wire technology. A brief historical overview shows the evolution of steering systems in recent decades, as steer-by-wire technology found its way into a wide field of application originating from aviation and progressing to the automotive industry. In the subsequent section the focus on the application of a steer-by-wire system on single-track vehicles is discussed. In the last section a more detailed view on steer-by-wire and its application on bicycles is given.

2-1 Brief Historical Overview

2-1-1 Aviation industry

The first true by-wire technology was developed in aviation where the hydraulic and mechanical connections between the input device of the pilot and the actuators to the wings have been replaced by electric wires. Those systems are called fly-by-wire systems. The controller located between the input device of the pilot and electronic actuators, decide in which way to move the wings which make the aircraft move in the desired way. Historically, analogue and digital fly-by-wire systems can be distinguished. Analogue fly-by-wire systems still have the mechanical actuators in place and are electronically operated, while digital fly-by-wire systems make use of exclusively electronic actuators.

Fly-by-wire systems have slowly evolved from early autopilots in the 1940s to advanced control systems seen in aviation today [Schmitt et al., 1998]. The autopilot is probably the first system introduced in aviation to assist the pilot during flight. The first autopilot was designed and build for use in World War II. It provided a stable platform for the bomber to engage its target. The autopilot was an electrical system using potentiometers connected to a gyroscope. The potentiometers were connected to amplifiers which in turn operate the elevator, rudder and ailerons using servomotors or solenoids. In those early years, not only the technical realization was an obstacle but also the need to convince pilots that it is safe to fly an aircraft without mechanical linkages to the controls.

The first aircraft that was designed and flown with an analog fly-by-wire flight control system was the 1958 Avro Canada CF-105 Arrow fighter aircraft. This system was equipped with redundant safety systems, was designed to be integrated with a computerized navigation and provided tactile feedback to the pilot with the use of mechanical springs on the operating controls. The first digital fly-by-wire aircraft was an Ought F-8C Crusader modified by NASA in 1972. Although the tactile feedback was still a mechanical solution by a dummy weight placed on the control stick giving tactile feedback proportional to the airplanes acceleration [Tomayko, 2000]. In 1977 NASA equipped its Space Shuttle Orbiter with an all digital fly-by-wire system to control its attitude in space.

As fly-by-wire technology evolved from military and aerospace industry, the first production airliner using analogue fly-by-wire technology was the Concorde introduced in 1969 [Tischler, 1996]. The first commercial airliner equipped with digital fly-by-wire technology was the Airbus A320 introduced in 1984 which is still in use today.

2-1-2 Automotive industry

Cars were initially steered by a tiller device, similar to that used to control a boats rudder. The basic design of automotive steering systems has changed little since the invention of the steering hand-wheel itself. The input from the driver is transmitted by a rotating shaft through some reduction mechanism into a turning motion of the wheels. One of the first applications of an automobile steering wheel was already in 1894 on Alfred Vacheron's race-car, which preceded the 1898 introduced Panhard which incorporated hand wheel steering on a commercial vehicle.

The following prominent development in the history of the automobile was the introduction of hydraulic power steering. Engineer Francis W. Davis began exploring how steering could be made easier and in 1926 he demonstrated the first power steering system. As this was more or less a proof of concept, it was not before 1951 that Chrysler introduced the first commercially available passenger car with hydraulic power steering, the Chrysler Imperial.

As vehicles have become increasingly more heavy and tires more wide, the need for power steer systems have increased to reduce the physical effort. Using hydraulic pressure supplied by a pump, power steer systems amplify the torque required by the driver to turn the steering wheels. In this way the steering effort is reduced improving comfort and safety. A pressure relief valve in the hydraulic circuit adds the option to adjust the amount of assisted steer torque. This can even be made dependent on the speed of the vehicle and driver preference. The recent application of electric power-steer does away with the hydraulic pump with providing the steering torque by an electric motor to assist the steering motion. This concept first appeared in 1990, introduced by Honda on the NSX sports-car. The benefits of using an electronic assisted steering system instead of hydraulic assisted systems are multiple. Less environmental impact due to the absence of hydraulic fluids, space savings, less costly and an increase in fuel economy. In 2000 Honda launched the S2000, a sports car with a variable gear ratio steering system. It provided a variable ratio between the hand-wheel position and steering wheels position by using a planetary gearwheel arrangement actuated by an electric motor. In this way it was possible to adjust the ratio to suit different driving conditions.

BMW introduced an active steering system in 2003 in their 5-series, which coupled the actuation of the electronic variable steering system to the electronic stability control system of the

vehicle. This gave way to actively control the directional stability of the car by positioning the steering wheels more effectively and more quickly than a human driver can do based on additional sensor information.

The next step in steering technology was the elimination of the mechanical steering shaft by an all electronic system. Some prototype passenger cars already utilize by-wire technology for advanced operation of the brakes and the throttle valve on the engine [Seidel, 2009]. None of these systems offer the technical advantages as steer-by-wire does. Completely replacing the mechanical steering column with an electronic system offers several benefits in terms of:

- ▷ *Design freedom* - By eliminating the steering column, the space around the engine in a passenger car can be utilized more efficiently and also simplifies the placement of the steering hand-wheel. It even can be made modular to be placed on the right or left depending on the country at which the car is used.
- ▷ *Operation* - Interior design is not restricted to the use of a steering column layout and even a joystick can be used as in input to the car, which is more like airplanes and trains are operated.
- ▷ *Comfort* - Without the mechanical connection between the front wheels and the interior of the car, noise and vibrations can be kept outside the driver compartment more easily. Because of the need for a stiff connection between the steering wheels and the hand-wheel to improve road feel, vibrations with specific frequencies are transmitted easily from the wheels to the driving compartment. Removing this stiff, mechanical connection does away with the transmission of undesirable vibrations causing noise, increasing comfort and driving pleasure.
- ▷ *Safety* - In addition during a frontal crash the absence of the steering column makes it less likely to cause serious injury to the driver by intrusion of mechanical objects into the driver compartment. Car manufacturers have been trying to minimize the risk using telescopic steering column designs but these systems do not entirely eliminate the risk of intrusion of objects during a frontal crash.
- ▷ *Features* - Incorporating the steering system with additional control systems in the car can enhance driving performance and safety. A variable ratio between the hand-wheel and steering wheels makes it possible to adjust the driving experience and comfort at high and low speeds. A variable steering effort can improve rider feel at different driving speeds, for instance when parking or highway driving. The most significant benefit of steer-by-wire is undoubtedly the ability to overrule the driver input and make a more sensible decision based on parameters from additional sensors in the car far more quickly than a human driver can do. In this way steer-by-wire can be fully integrated in a vehicle dynamics control system. Which in turn can improve comfort and safety intensively.

2-2 Steer-by-Wire and Single-Track Vehicles

Improvements in vehicle safety, performance, and comfort are already slowly being introduced in the four-wheeled automotive world. Passenger car drivers already benefit from the advanced

possibilities those control systems can give and steer-by-wire offers a great improvement in a lot of aspects. Pilots of fighter- and passenger aircraft already make great use of fly-by-wire systems for decades, without them it would not even be possible to fly those aircraft.

Motorcycles can be equipped with steering dampers on the steering assembly to passively attenuate unstable motions. The use of such a passive system is limited, especially if compared with the possibilities that a steer-by-wire system can give. Motorcycles can benefit from such an active control system when integrated in a dynamic stability system improving safety and comfort. In recent literature however, only two references can be found by [Marumo and Nagai, 2007] and [Katagiri et al., 2009] proposing a steer-by-wire system for motorcycles to enhance its dynamic behavior. It remains questionable if the removal of the counter steering behavior as proposed by [Marumo and Nagai, 2007] will be beneficial. The possibility of a lane keeping assistance system on motorcycles by [Katagiri et al., 2009] on the other hand can greatly improve safety. This is also demonstrated by [Seiniger et al., 2011] by actively assisting the motorcycle rider's steer input to hold its driving path during extensive in-corner braking manoeuvres.

The application of a steer-by-wire system on bicycles is less evident, but can also greatly improve the lateral stability over a wide range of forward speeds. The dynamic behavior can be changed with the ease of downloading a new control system in the controller without changing the physical geometry of the bicycle. The bicycle can be designed to everyone's needs with focus on elderly and people with a physical handicap having trouble riding a conventional bicycle [Astrom et al., 2005].

2-3 Steer-by-Wire Bicycle

Although steering systems found on airplanes, cars, motorcycles and bicycles physically differ from each other, their operation remains the same. Considering ground vehicles move in a single, two-dimensional plane, the input device by the driver is used to change the angular position of the vehicle with respect to an external reference point. This angular position is also known as the yaw angle of the vehicle. Cars, motorcycles and bicycles are ground vehicles, who only require a single degree-of-freedom to change the yaw-angle of the vehicle, and subsequently only need a single degree-of-freedom control which is provided by the steering wheels. As the scope of this report is about single-track vehicles, consider a regular bicycle steering system shown in figure 2-1a and its steer-by-wire equivalent shown in figure 2-1b.

A conventional steering system can be visualized as a chain of interconnected mechanical parts consisting of the handlebar, the steering shaft and the front fork. As in a true mechatronic implementation, the steer-by-wire bicycle has the mechanical steering shaft replaced by two actuators and two angular position sensors connected to a controller. The steering actuator is used to rotate the front wheel in the desired position in which the angular-position sensor is used in a feedback configuration. On the handlebar side, an identical approach applies as the handlebar actuator applies a reaction torque to the driver in order to provide some level of haptic feedback, resembling the reaction torque between the front wheel and ground surface. As shown in figure 2-2, rotation of the handlebar on a conventional bicycle is initiated when the driver applies a handlebar torque T_h to the handlebars which is higher than the environmental reaction torque T_e . The handlebar torque exerted by the driver is transferred

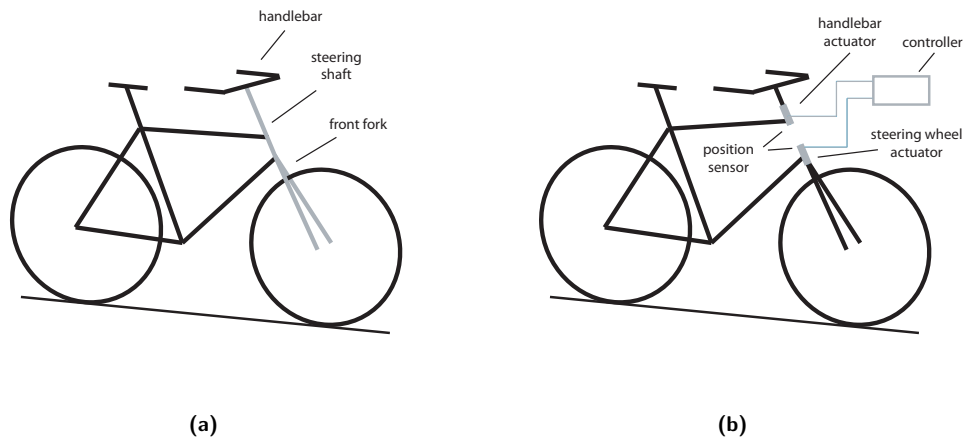


Figure 2-1: A schematic overview of the steering-assembly of a conventional bicycle (a) compared to its steer-by-wire equivalent (b). The mechanical connection between the handlebar and front fork is replaced by actuators, sensors and a controller to create an artificial stiffness to imitate the properties of a mechanical connection.

by the steering shaft, front fork and front wheel to the ground surface where the reaction torque T_e opposes the handlebar torque. When the handlebar torque exceeds the reaction torque, the steering assembly changes its angular position due to an angular acceleration proportional to the inertia properties of the steering assembly and the resulting torque input.

A more detailed view is given in the block diagram in figure 2-3 for both the conventional steered bicycle and the steer-by-wire bicycle. From left to right, the relation between the driver torque T_h and the bicycle front-wheel angular position δ is visualized. Both bicycles have a handlebar and front fork assembly with a certain rotational inertia J indicated with the two left- and right most blocks respectively. The difference between the interconnection of these two subsystems characterize a typical steer-by-wire system. The steering shaft of a conventional bicycle is essentially an elastic element having a certain stiffness K and damping C indicated by the shaft-block. The steer-by-wire bicycle however, utilizes a controller to imitate the behavior of the mechanical steering shaft, making use of the angular position- and rate information of the steering wheel and handlebar as indicated by the lower feedback loop. The upper feedback loop provides the steer torque T_δ at the handlebar to provide the driver a realistic feedback torque at the handlebar.

From the block diagram in figure 2-3, the front fork block determines the relation between the steer torque T_δ and the steering wheel angle δ . For a bicycle placed on a road-surface however, a change in steering wheel angle also implies a change in roll angle ϕ of the bicycle and vice versa, as the roll- and steering motions of the bicycle are geometrically coupled. The front fork block should be replaced with a bicycle model which includes the coupling between the roll- and steering motions as shown in figure 2-4. The interaction of the roll- and steering actions characterize the two degrees-of-freedom of a typical single-track vehicle.

A realistic model which describes the interaction between the steer torque T_δ , roll torque T_ϕ , steer angle δ and roll angle ϕ of a bicycle based on its mass- and geometrical properties was developed by [Whipple, 1899]. Integration of a Whipple-like bicycle model in a structure as proposed in figure 2-4 allows for numerical simulation of the lateral motion of a bicycle based on handlebar torque input and specific controller parameters.

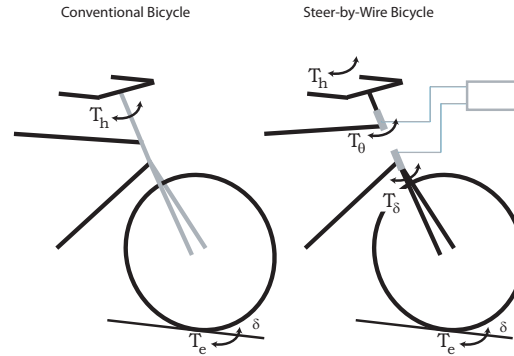


Figure 2-2: A schematic overview of the steering assembly of a conventional bicycle (a) compared to its steer-by-wire equivalent (b). The steering assembly of a conventional bicycle rotates along a single degree-of-freedom δ , due to interaction of the handlebar torque T_h provided by the driver and the environmental reaction torque T_e . The steering assembly of a steer-by-wire bicycle has an additional degree-of-freedom θ the handlebar-angle. Actuators on the handlebar- and steering assembly provide an artificial stiffness by reaction torques T_θ and T_δ respectively.

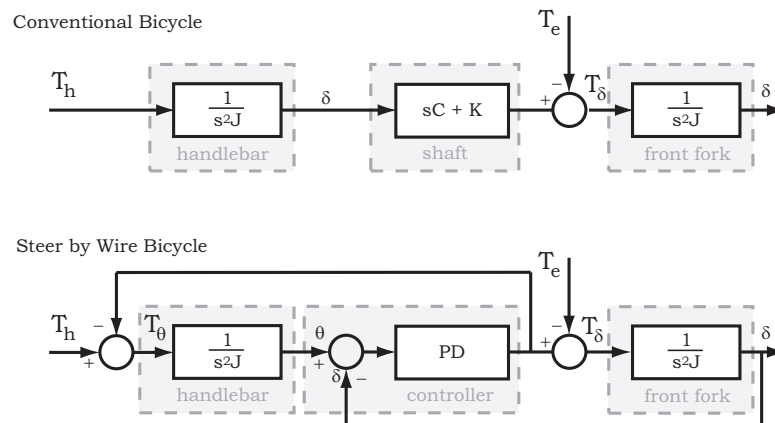


Figure 2-3: A block diagram showing a graphical overview of the steer-by-wire system compared to the steering assembly of a conventional bicycle. The interaction between the angular position δ and handlebar torque T_h of the steering assembly of a conventional bicycle is dependant on the combined rotational inertia J of the handlebar and front fork as well as the torsional stiffness K and damping C of the shaft. The interaction between the handlebar torque T_h and angular position δ of the front fork on a bicycle equipped with a steer-by-wire system, is predominantly dependant on the PD-controller settings which provide the artificial stiffness and damping.

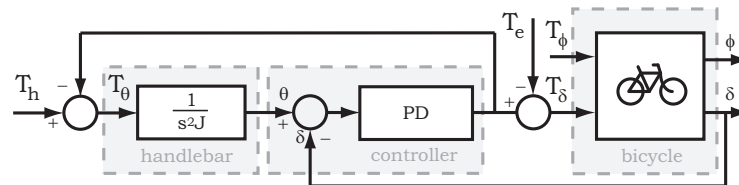


Figure 2-4: A block diagram showing a graphic overview of the steer-by-wire system interacting, with a more realistic bicycle model including the coupling between the roll- and steering motions. The interaction between the handlebar torque T_h and angular position δ of the front fork on a bicycle equipped with a steer-by-wire system is dependant on the PD-controller settings as shown previously. However an accurate model should also account for the coupling between the roll- and steering motions of the bicycle.

2-4 Summary

In this chapter the fundamentals of a steer-by-wire system are visualized compared to a conventional, mechanically coupled steering system. It is shown that a PD-controller algorithm is fundamentally identical to a conventional steering shaft. To be able to quantify the differences between a conventional steered bicycle and a bicycle equipped with a steer-by-wire system however, a suitable numerical model should provide insight based on bicycle-, actuator- and controller parameters. The following chapter will focus on the design of a suitable numerical model.

Bicycle Modeling

The ability to improve the lateral stability is an important aspect for application of a steer-by-wire system on a bicycle. At low forward speeds the human rider is not able to stabilize the bicycle very easily. To implement a true decoupled controller action irrespective of human control intervention, the handlebars are completely separated from the front wheel, unlike a steering assist system where the rider is still partly in control. This does not mean that the rider loses control over the vehicle, the controller is able to stabilize the bicycle far more quickly than a human rider is able to, while the driver still maintains directional control.

In order to enhance the lateral stability of the bicycle, an electronic actuator is attached to the steering wheel. The handlebar of the bicycle is mechanically decoupled from the steering wheel and only provides directional information to the controller. The controller operates the steering actuator based on sensor information like steering angle, forward speed and roll angle of the bicycle. Numerous control algorithms can be utilized with specific properties to suit specific needs under specific circumstances. In the following section, a mathematical model of the bicycle is used to predict the lateral stability of the bicycle with specific control algorithms. First, the Benchmark Bicycle model is presented which is used as the foundation for the Steer-by-Wire Bicycle model. This steer-by-wire model contains an additional handlebar body and is used to simulate different control strategies to enhance the lateral stability of the bicycle. Time simulations show the lateral response of the bicycle models on rider torque- or roll torque input perturbations.

3-1 Benchmark Bicycle model

One may know from experience that a bicycle is highly unstable at low forward speeds and becomes easy to stabilize at moderate to high forward speeds. Studies on the stability of the bicycle have been a topic of interest since the last century where the Whipple model [Whipple, 1899] is the most early recognized contribution. This model has been benchmarked and numerically validated by [Meijaard et al., 2007]. Measurements with an instrumented bicycle by [Kooijman et al., 2008] show close agreement to this benchmark model and therefore the Whipple model is chosen to be the foundation for the Steer-by-Wire Bicycle model.

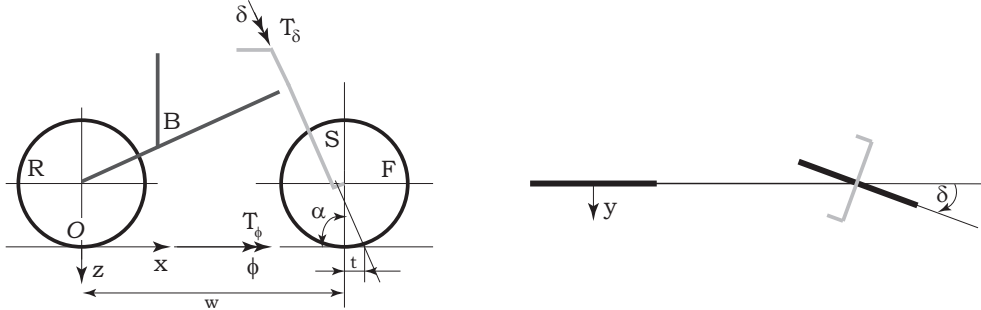


Figure 3-1: The Benchmark Bicycle model showing four separate bodies hinged at the wheels and steering stem originating from the 1799 Whipple model.

The Benchmark Bicycle model consists of four rigid bodies, a front wheel F , a rear wheel R , a rear frame B and steering assembly S as shown in figure 3-1. The rider is rigidly attached to the rear frame with no hands on the handlebars. The Benchmark Bicycle model is specified by geometric-, mass- and inertia-parameters shown in table 3-1.

These parameters include geometric properties like wheelbase w , trail t , head angle α and mass- and inertia parameters for the four individual bodies. The bodies are connected by rotational joints at the wheels and between the steering assembly and rear frame. The wheels have knife-edged contact with the ground and are modeled with holonomic constraints in the normal direction and non-holonomic constraints in the lateral and longitudinal direction. The x -axis pointing in the longitudinal direction of the bicycle and the z -axis pointing downwards. The model has three velocity degrees of freedom; the roll rate of the rear frame $\dot{\phi}$, the steer rate $\dot{\delta}$ and the forward speed v of the bicycle.

The linearized equations of motion for the bicycle at a specific constant forward speed v are expressed by two degrees of freedom, the roll angle ϕ and the steer angle δ , and form a set of coupled, second order ordinary differential equations. The first equation is called the roll equation and the second is called the steer equation. In matrix form they can be expressed as,

$$\mathbf{M}\ddot{\mathbf{q}} + [v\mathbf{C1}]\dot{\mathbf{q}} + [\mathbf{K0} + v^2\mathbf{K2}]\mathbf{q} = \mathbf{f} \quad (3-1)$$

with the state vector $\mathbf{q} = [\phi, \delta]^T$ and forcing term \mathbf{f} defined by,

$$\mathbf{f} = \begin{bmatrix} T_\phi \\ T_\delta \end{bmatrix}. \quad (3-2)$$

The matrices presented in equation 3-1 are derived in [Meijaard et al., 2007] and are functions of the geometric-, mass- and inertia-parameters as well as the forward speed v . The symmetric mass matrix \mathbf{M} , a damping-like matrix $\mathbf{C1}$ which is a function of forward speed v and a stiffness matrix which is the sum of a constant part $\mathbf{K0}$ and a part $\mathbf{K2}$ which is quadratic

Parameter	Symbol	Value
Wheelbase	w	1.02 m
Trail	t	0.08 m
Head angle	α	$(2/5)*\pi$ rad
Gravity	g	9.81 N/kg
Forward speed	v	variable m/s
Rear wheel (R)		
Radius	R_{rw}	0.3 m
Mass	m_{rw}	2 kg
Mass moments of inertia	(A_{xx}, A_{yy}, A_{zz})	(0.0603, 0.12, 0.0603) kgm^2
Rear frame (B)		
Position center of mass	(x_{rf}, y_{rf}, z_{rf})	(0.3, 0, -0.9) m
Mass	m_{rf}	85 kg
Mass moments of inertia	$\begin{bmatrix} B_{xx} & 0 & B_{xz} \\ sym. & B_{yy} & 0 \\ & & B_{zz} \end{bmatrix}$	$\begin{bmatrix} 9.2 & 0 & 2.4 \\ & 11 & 0 \\ & & 2.8 \end{bmatrix} kgm^2$
Front frame (S)		
Position center of mass	(x_{ff}, y_{ff}, z_{ff})	(0.9, 0, -0.7) m
Mass	m_{ff}	4 kg
Mass moments of inertia	$\begin{bmatrix} S_{xx} & 0 & S_{xz} \\ sym. & S_{yy} & 0 \\ & & S_{zz} \end{bmatrix}$	$\begin{bmatrix} 0.05892 & 0 & -0.00756 \\ & 0.06 & 0 \\ & & 0.00708 \end{bmatrix} kgm^2$
Front wheel (F)		
Radius	R_{fw}	0.35 m
Mass	m_{fw}	3 kg
Mass moments of inertia	(F_{xx}, F_{yy}, F_{zz})	(0.1405, 0.28, 0.1405) kgm^2

Table 3-1: The geometric-, mass- and inertia-parameters defining the Benchmark Bicycle model.

in the forward speed v . The time response of the system in the absence of a forcing term is a linear combination of the eigenmodes. These eigenmodes together with their eigenvalues form a solution to the homogenous equation 3-1 of the form,

$$\mathbf{q} = q_0 e^{\lambda t}. \quad (3-3)$$

This leads to the characteristic polynomial equation which is quadratic in λ ,

$$\det(\mathbf{M}\lambda^2 + v\mathbf{C}\mathbf{1}\lambda + \mathbf{K}\mathbf{0} + v^2\mathbf{K}\mathbf{2}) = 0. \quad (3-4)$$

The eigenvalues for the Benchmark Bicycle model as a function of forward speed v are shown in figure 4-3b. The real parts of the eigenvalues are shown in black, where the negative real parts correspond to an asymptotically stable decaying motion, whereas real eigenvalues with a positive real part correspond to an unstable motion for the corresponding eigenmode. The grey line shows the imaginary parts of the eigenvalues which correspond to an oscillatory motion. For this double, second order model, up to four eigenmodes can be observed where oscillatory eigenmodes come in pairs. Two distinguishing modes are called the capsize- and weave-mode. The capsize-mode correspond to a real, non-oscillatory eigenvalue with an eigenmode dominated by the roll angle of the bicycle. At higher forward speeds, this mode becomes unstable and causes the bicycle to tilt over in a spiralling motion with a decreasing radius until it falls over. The weave-mode causes the bicycle to swing about the longitudinal direction dominated by steering. The final eigenmode is the caster-mode and corresponds to a large and stable, negative, real eigenvalue with an eigenmode dominated by steering. Two pairs of real eigenvalues start at near zero speeds from which one pair combines into the unstable oscillatory weave mode and becomes stable at the weave-speed v_w at 4.29 m/s. At higher forward speeds the capsize eigenmode becomes positive and mildly unstable at the

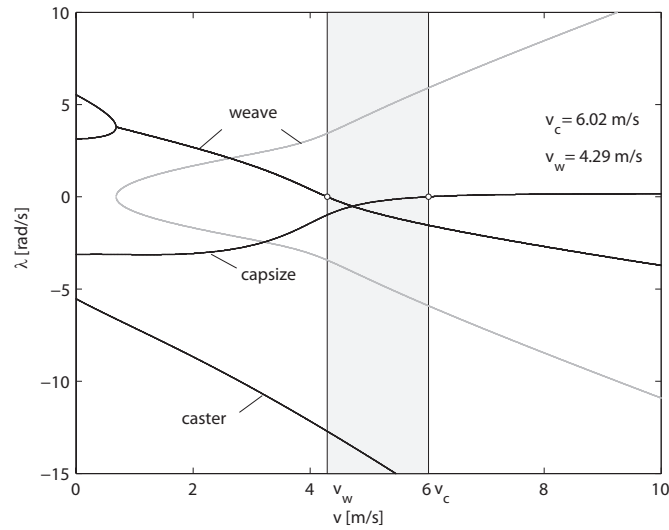


Figure 3-2: Eigenvalues λ for the lateral motion of the Benchmark Bicycle as a function of forward speed v in the range $0 \text{ m/s} < v < 10 \text{ m/s}$ (a).

capsize-speed v_c at 6.02 m/s . The speed range for which the bicycle is stable is shown in grey and is between the weave-speed v_w and capsize-speed v_c . For speeds below the weave-speed and above the capsize-speed, rider control is needed to stabilize the lateral motion in order to stay upright. Between the weave- and capsize speeds no stabilizing rider control is essential. It is below the weave-speed and above the capsize-speed where the steer-by-wire system is used to enhance the lateral stability. This is illustrated by the time simulations in figure 3-3a and 3-3b.

The time simulations show the lateral response for the Benchmark Bicycle model at a stable forward speed at 5 m/s and an unstable forward speed at 3 m/s , when subjected to a roll- and steer perturbation of 50 Nm and -2 Nm respectively. The Benchmark Bicycle model shows lateral stable behavior at 5 m/s as predicted, as well as the unstable lateral behavior at 3 m/s .

3-2 Steer-by-Wire Bicycle model

It would be very attractive to be able to shift the stable speed range, or even increase the stable speed range, by adjustment of the eigenvalues. In order to adjust the eigenvalues, a steer-by-wire bicycle design is proposed. By decoupling the handlebar input from the steer input it is possible to influence the equations of motion with respect to the steer equation. An actuator on the steering assembly makes it possible to adjust the dynamic behavior of the bicycle independent of the rider input.

The benchmark equation 3-1 is extended with an additional body by separating the front fork assembly into two individual separate bodies, handlebar H and front fork S as shown in figure 3-4.

The canonical form of 3-1 is expanded with a second-order differential equation 3-5 for the handlebar H at which an external hand torque T_θ is applied,

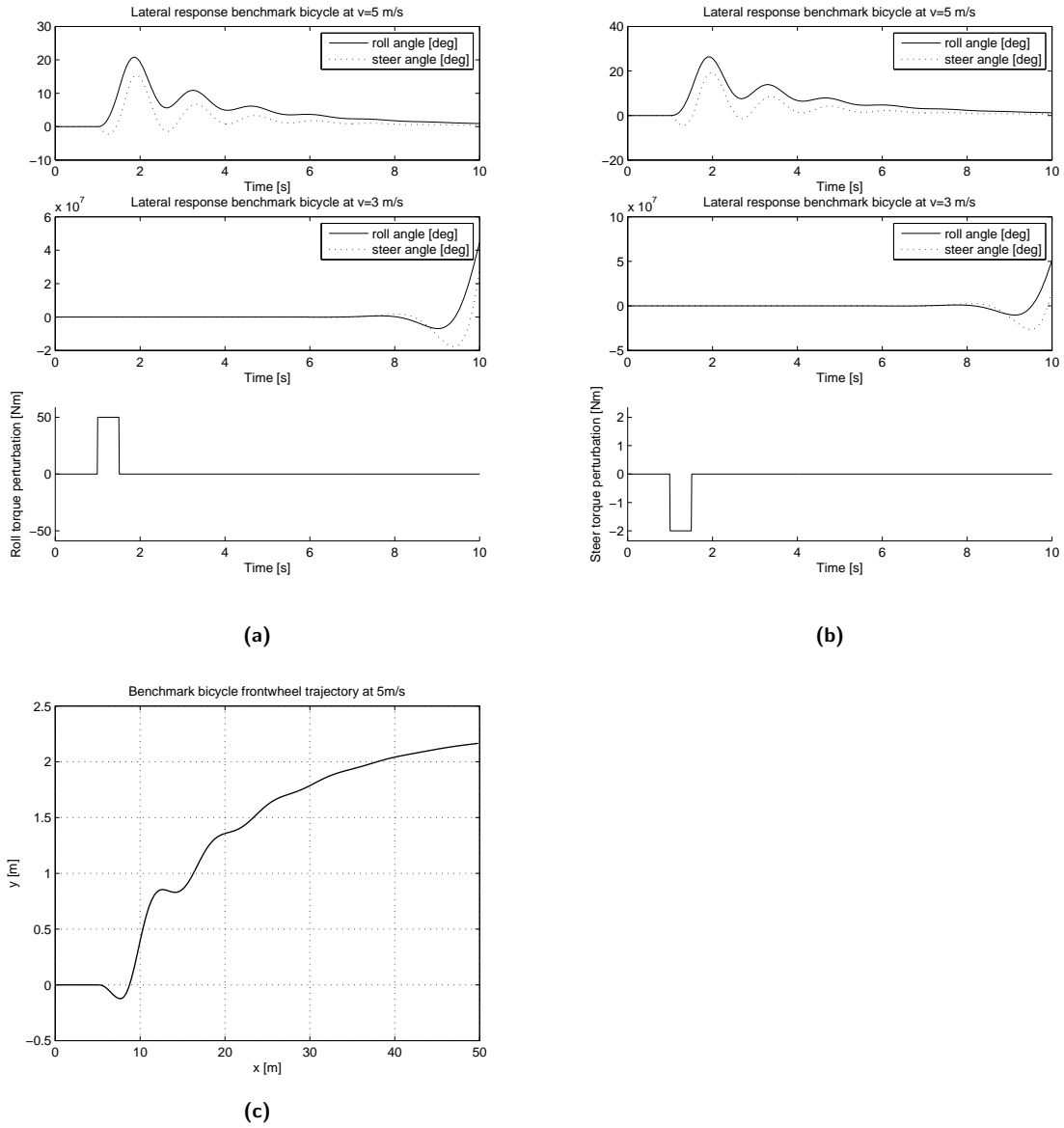


Figure 3-3: A time simulation (a) of the lateral motion of the benchmark bicycle to a 50 Nm roll perturbation inside the stable forward speed range at $v = 5$ m/s which shows a stable decaying roll- and steering motion. The time simulation at $v = 3$ m/s however shows an unstable increasing roll- and steering motion. The time simulation of the lateral motion of the benchmark bicycle to a -2Nm steer torque perturbation (b) shows a corresponding behavior. The ground trajectory of the front wheel contact patch (c) for the -2Nm steer perturbation shows a stable progression.

$$I_{\theta} \ddot{\theta} = T_{\theta}. \tag{3-5}$$

Where I_{θ} is the rotational inertia of the handlebar and no damping or friction is assumed. Subsequently, the state vector becomes $\mathbf{q} = [\theta, \dot{\theta}]^T$ and the forcing term \mathbf{f} is expanded to:

$$\mathbf{A} = \begin{bmatrix} -\bar{M}^{-1}\bar{C} & -\bar{M}^{-1}\bar{K} \\ I & 0 \end{bmatrix}, \quad \mathbf{B} = \begin{bmatrix} \bar{M}^{-1} \\ 0 \end{bmatrix}. \quad (3-11)$$

$$\mathbf{C} = \begin{bmatrix} 0 & I \end{bmatrix}, \quad \mathbf{D} = \begin{bmatrix} 0 \end{bmatrix}. \quad (3-12)$$

In a steer-by-wire application the single input to the system is the handlebar torque T_θ provided by the driver. The output to the system is the roll angle ϕ and the steering wheel angle δ of the bicycle. An artificial stiffness between the handlebar body H and front fork S would be realized by the actuators which replace the steering shaft from a conventional bicycle. The artificial stiffness provided by the actuators would depend on controller parameters having additional coefficients appearing in the forcing term \mathbf{f} in equation 3-6.

3-3 Summary

In this chapter the fundamental Whipple bicycle model is covered by analyzing the lateral stability boundaries as a function of forward speed, by simulation of a bicycle having specific geometric-, mass- and inertia properties as defined by a recognized and benchmarked data-set. The Steer-by-Wire Bicycle model was introduced by addition of an extra degree-of-freedom consisting of the handlebar angle θ , expanding the Benchmark Bicycle model to three coupled second-order differential equations. The coupling of the handlebar degree-of-freedom to the steering degree-of-freedom is related to controller parameters appearing in the right-hand side forcing-term which will be covered in the next chapter, as well as additional control algorithms to explicitly define the dynamic behavior of the steer-by-wire bicycle.

System Modeling and Simulation

The dynamic behavior or lateral stability of a bicycle is primarily defined by the eigenmodes and associated eigenvalues which depend on the mass-, damping- and stiffness properties of the bicycle as shown in chapter 3. Considering the Steer-by-Wire Bicycle model and combining equations 3-6, 3-7 and 3-8 the expression becomes

$$\begin{bmatrix} I_\theta & 0 \\ 0 & \mathbf{M} \end{bmatrix} \begin{bmatrix} \ddot{\theta} \\ \ddot{\phi} \\ \ddot{\delta} \end{bmatrix} + \begin{bmatrix} 0 & 0 \\ 0 & v\mathbf{C1} \end{bmatrix} \begin{bmatrix} \dot{\theta} \\ \dot{\phi} \\ \dot{\delta} \end{bmatrix} + \begin{bmatrix} 0 & 0 \\ 0 & \mathbf{K0} + v^2\mathbf{K2} \end{bmatrix} \begin{bmatrix} \theta \\ \phi \\ \delta \end{bmatrix} = \begin{bmatrix} T_\theta \\ T_\phi \\ T_\delta \end{bmatrix}. \quad (4-1)$$

Ignoring the virtual steering shaft between the handlebar- and steering assembly of the steer-by-wire bicycle, the required coupling terms included in the forcing term on the righthand side of the equation will be covered in section 4-2. The ability to apply an additional control algorithm by utilizing an actuator on the steering assembly of the steer-by-wire bicycle allows to physically provide an additional torque along the steering degree-of-freedom. This makes it possible to virtually adjust the entries in the mass-, damping- and stiffness matrix, by multiplying each state of the bicycle with a suitably chosen constant to calculate the required additional steer torque to move the eigenvalues of the system.

The freedom to adjust each individual entry in the system matrices and subsequently the ability to place the eigenvalues at any desired location is however limited. First, only an additional steer torque can be applied by the steer-by-wire system in contrast to an additional roll torque. Consequently only the entries in the lower row of the system matrices in 4-1 can be influenced. Second, if exclusively state information on the roll- and steer angle as well as the roll- and steer rate are used, the entries in the mass matrix are neither influenced which require roll- and steer acceleration feedback. The following expression shows the entries in the system matrices that can be influenced by feedback of angle- and angular rate information on the steer- and roll degree-of-freedom. Unreachable entries in the system matrices are marked with a dot (\cdot) in equation 4-2,

$$\begin{bmatrix} \cdot & \cdot & \cdot \\ \cdot & \cdot & \cdot \\ \cdot & \cdot & \cdot \end{bmatrix} \begin{bmatrix} \ddot{\theta} \\ \ddot{\phi} \\ \ddot{\delta} \end{bmatrix} + \begin{bmatrix} \cdot & \cdot & \cdot \\ \cdot & \cdot & \cdot \\ \cdot & c_{21} & c_{22} \end{bmatrix} \begin{bmatrix} \dot{\theta} \\ \dot{\phi} \\ \dot{\delta} \end{bmatrix} + \begin{bmatrix} \cdot & \cdot & \cdot \\ \cdot & \cdot & \cdot \\ \cdot & k_{21} & k_{22} \end{bmatrix} \begin{bmatrix} \theta \\ \phi \\ \delta \end{bmatrix} = \begin{bmatrix} \cdot \\ \cdot \\ T_{\delta} \end{bmatrix} \quad (4-2)$$

Despite these limitations, the steer actuator on a steer-by-wire system is more than capable of influencing the eigenvalues and the dynamic behavior of the bicycle in a way that is not able with a conventional steered bicycle. Entries c_{21} and c_{22} in the damping matrix as well as k_{21} and k_{22} in the stiffness matrix can be influenced which will be illustrated in the following sections. The next sections will particularly focus on the modeling and simulation of various control strategies to give the steer-by-wire bicycle specific properties with respect to its dynamic behavior and lateral stability.

4-1 Controllability

To be able to control the lateral stability of the bicycle, the behavior of the bicycle should be controllable by the steer actuator in the entire forward speed range v from 0 m/s to 10 m/s. The controllability of the bicycle is investigated by evaluating the controllability matrix which is defined by the following relation,

$$\mathbf{Q} = [b, bA, bA^2, \dots, bA^{n-1}] \quad (4-3)$$

where \mathbf{A} is the state matrix and \mathbf{b} is the input vector defined by the single steer torque input. If the rank of the controllability matrix \mathbf{Q} is equal to the number of states n of the system, the system is fully controllable by the steer torque actuator. As the state matrix \mathbf{A} is a function of the forward speed v the rank of the controllability matrix has to be evaluated over the entire forward speed range.

In order for the controllability matrix to be full rank, the square matrix has to be invertible by definition i.e. non-singular. The singularity of the controllability matrix can be visualized by the so called condition numbers as a function of the forward speed. These condition numbers are defined as the ratio between the highest and lowest vector norm of the matrix. A singular, non-invertible matrix will have a condition number near infinity. Figure 4-1 shows the condition numbers for the steer-by-wire bicycle model indicating rank deficiency at two distinct forward speeds. These two distinct peaks define an uncontrollable state of the bicycle with respect to the particular input defined in input vector \mathbf{b} .

These uncontrollable forward speeds can be calculated by evaluating the determinant of the controllability matrix at zero. As the state matrix \mathbf{A} is a function of forward speed v , this leads to a characteristic equation as a function of forward speed v . Finding forward speeds at which the bicycle is uncontrollable is done by evaluating the following expression,

$$\det([b, bA, bA^2, \dots, bA^{n-1}]) = 0. \quad (4-4)$$

This characteristic equation yields two forward speeds for which the bicycle is uncontrollable.

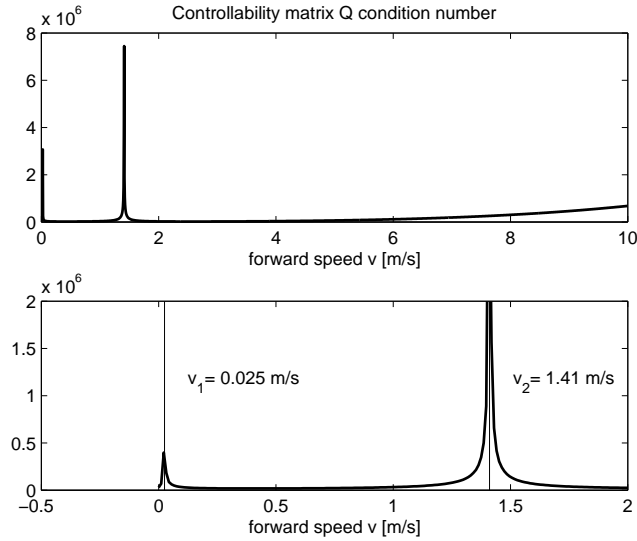


Figure 4-1: Condition numbers of the controllability matrix Q as a function of forward speed v in the range $0 \text{ m/s} < v < 10 \text{ m/s}$ and a close-up in the range $0 \text{ m/s} < v < 2 \text{ m/s}$. Two distinct peaks show an uncontrollable mode by exclusive use of the steer torque actuator.

Solving for v leads to the following two positive velocities for which the bicycle is uncontrollable by the steering actuator:

$$v_1 = 0.025 \text{ m/s}$$

$$v_2 = 1.411 \text{ m/s}$$

The bicycle is uncontrollable at v_1 and v_2 which does not necessarily pose a problem from a practical point of view as the rider on the bicycle is still able to apply a certain roll torque to the bicycle by body movement at those very distinct forward speeds. From a numerical point of view however, the calculation of the required additional actuator torque in some control algorithms will be problematic. The implications of this effect will be shown in the following sections.

4-2 Handlebar Tracking

The rider uses the handlebar on the steer-by-wire bicycle to provide directional information, like a conventional bicycle it is used to steer the bicycle in the desired direction. Therefore, the steering wheel should track the handlebar position closely without overshoot or time delays.

A tracking controller needs to be implemented to minimize the difference between the handlebar angle θ and the steering wheel angle δ . In this way the steer-by-wire system should behave like an ordinary, mechanically steered bicycle while providing the steer torque T_δ at the handlebar of the bicycle. A PD-controller is implemented which provides a control torque T_{PD} to the steering wheel actuator. The steer torque input T_δ in the forcing term 3-6 is now defined as,

$$T_\delta = T_{PD} \tag{4-5}$$

The undamped natural frequency ω_0 is defined as equation 4-11,

$$\omega_0 = \sqrt{K_p/I_\theta}. \quad (4-11)$$

The damping term is a function of the damping ratio ζ and natural frequency ω_0 shown in equation 4-12,

$$2\zeta\omega_0 = K_d/I_\theta. \quad (4-12)$$

Defining a damping ratio $\zeta=1$, a handlebar inertia $I_\theta=0.001 \text{ kgm}^2$ and a natural frequency $\omega_0=10 \text{ rad/s}$ which gives the following coefficients for the proportional gain $K_p=0.1 \text{ Nm/rad}$ and derivative gain $K_d=0.02 \text{ Nms/rad}$. Applying these coefficients in equation 4-6 leads to the eigenvalue plot shown in figure 4-3a.

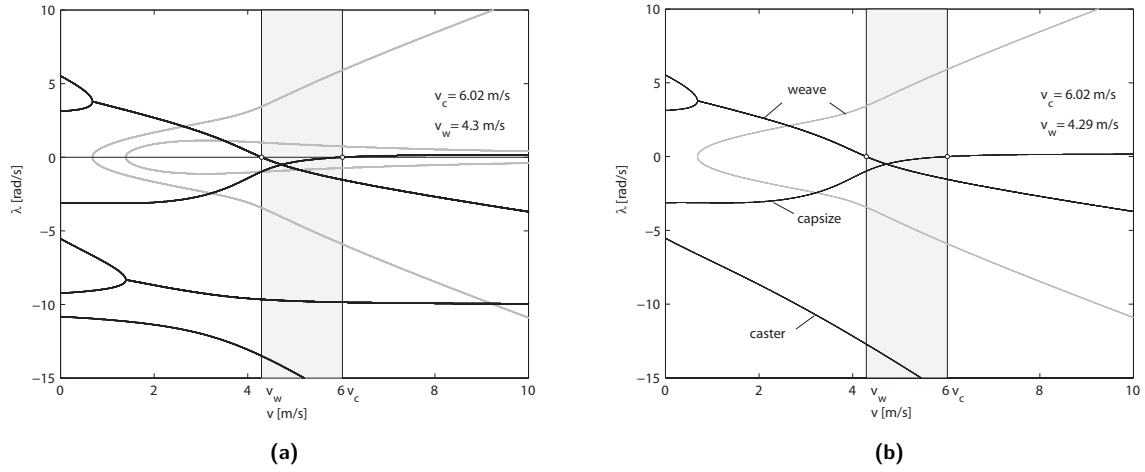


Figure 4-3: Eigenvalues λ for the Steer-by-Wire Bicycle model (a) as a function of forward speed v in the range $0 \text{ m/s} < v < 10 \text{ m/s}$ in comparison to the eigenvalues for the Benchmark Bicycle model (b).

The eigenvalue plots between the Steer-by-Wire Bicycle model 4-3a and the conventional Benchmark Bicycle model 4-3b indicate an identical lateral response shown by the identical eigenvalues for the weave-, capsizes- and caster modes. However an additional real and imaginary branch can be observed which originates from the additional handlebar body. The magnitude of this stable eigenvalue branch corresponds with the selected natural frequency of $\omega_0=10 \text{ rad/s}$.

Time simulations 4-4a and 4-4b show the lateral response for the Steer-by-Wire Bicycle model at a stable forward speed at 5 m/s and an unstable forward speed at 3 m/s , when subjected to a roll- and handlebar perturbation of 50 Nm and -2 Nm respectively. These simulation results do not show any differences in lateral motion compared to the Benchmark Bicycle model when subjected to a roll torque disturbance. However, when subjected to a handlebar torque disturbance the steering wheel is not able to track the handlebar angle with the current controller gains $K_p=0.1 \text{ Nm/rad}$ and $K_d=0.02 \text{ Nms/rad}$. Increasing the natural frequency ω_0 to 300 rad/s for the controller bandwidth, increases the proportional gain to $K_p=90 \text{ Nm/rad}$ and the derivative gain to $K_d=0.6 \text{ Nms/rad}$. The simulations with the increased bandwidth tracking controller settings are shown in figure 4-5a and 4-5b. The increased controller bandwidth reduces the steady-state tracking error between the handlebar- and steering wheel angle

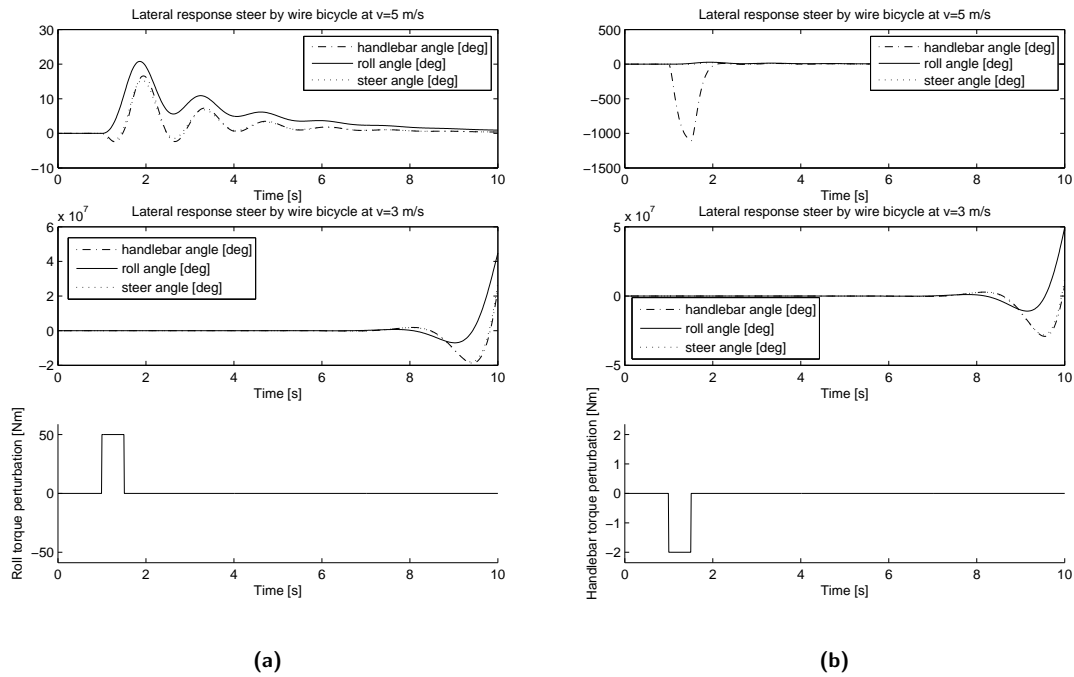


Figure 4-4: A time simulation (a) of the lateral motion of the steer-by-wire bicycle to a 50 Nm roll perturbation inside the stable forward speed range at $v = 5$ m/s which shows a stable decaying roll- and steering motion. The time simulation at $v = 3$ m/s however shows an unstable increasing roll- and steering motion. The time simulation of the lateral motion of the steer-by-wire bicycle to a -2 Nm steer torque perturbation shows a handlebar motion unable to track the steering wheel motion due to the low controller bandwidth of $\omega_0=10$ rad/s.

substantially. The following table shows the tracking error as a function of various controller parameters:

ω_0		tracking error
10 rad/s	$K_p = 0.1$ Nm/rad	1100 deg
	$K_d = 0.02$ Nm.s/rad	
100 rad/s	$K_p = 10$ Nm/rad	11 deg
	$K_d = 0.2$ Nm.s/rad	
300 rad/s	$K_p = 90$ Nm/rad	1.3 deg
	$K_d = 0.6$ Nm.s/rad	

As the proportional gain K_p and the steady state tracking error scale linearly, it follows that if the maximum allowable tracking error between the handlebar and steering wheel is determined to be one degree maximum, a proportional gain K_p of about 100 Nm/rad should be sufficient. Physical actuator torque limitations have not been considered in this simulation, this will be covered in following chapters.

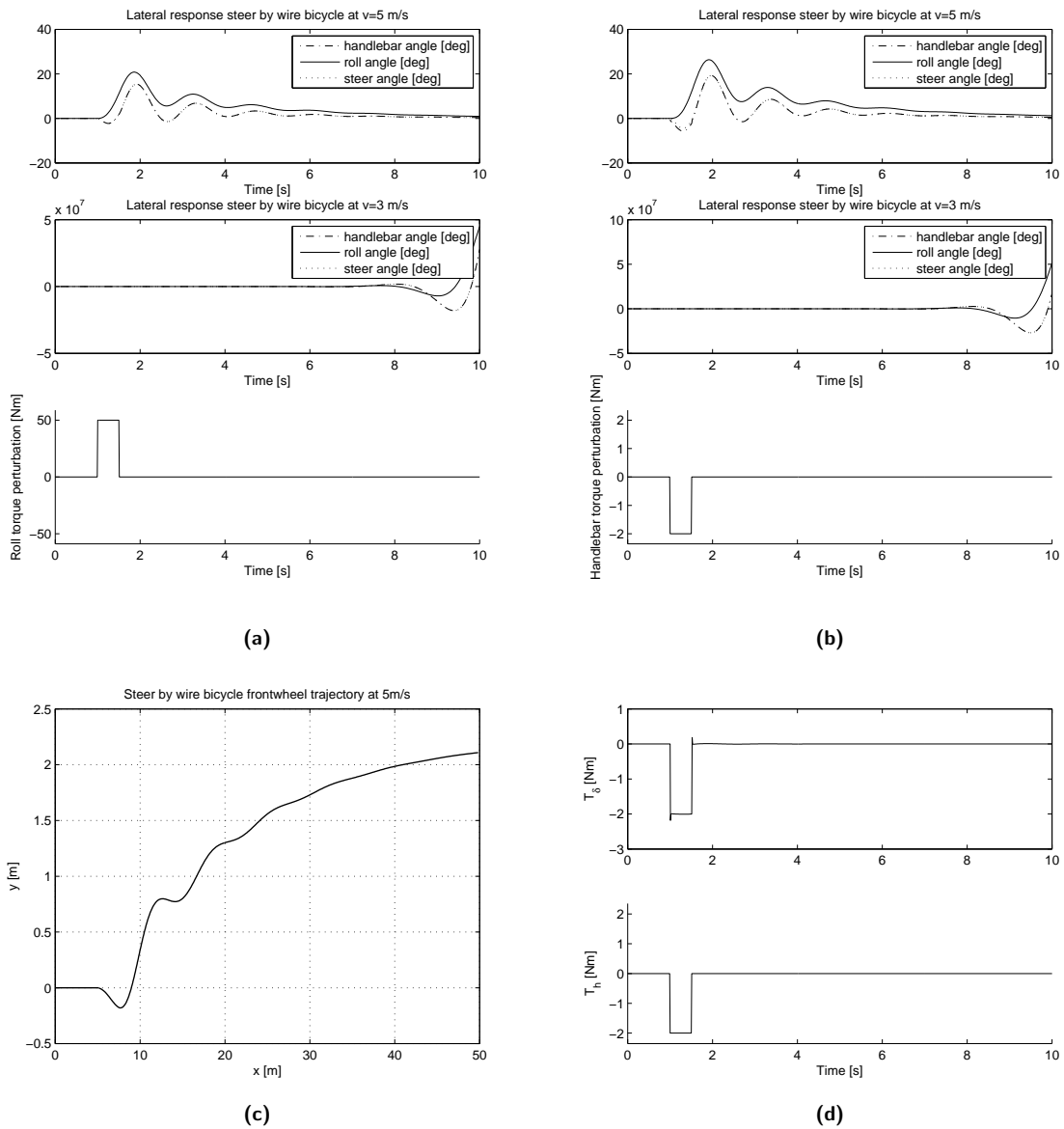


Figure 4-5: A time simulation (a) of the lateral motion of the Steer-by-Wire Bicycle model to a 50 Nm roll perturbation inside the stable forward speed range at $v = 5$ m/s which shows a stable decaying roll- and steering motion. The time simulation at $v = 3$ m/s however shows an unstable increasing roll- and steering motion. The time simulation of the lateral motion of the Benchmark Bicycle model to a -2 Nm steer torque perturbation (b) with an increased controller bandwidth of $\omega_0=300$ rad/s, shows a significant improved steering wheel tracking performance. The ground trajectory of the front wheel contact patch (c) for the -2 Nm steer perturbation. The steering wheel actuator torque T_{PD} shows a good handlebar tracking performance.

4-3 Lateral Stability Enhancement

An additional control torque on the steering degree-of-freedom makes it able to adjust the eigenvalues of the bicycle in such a way that the dynamic behavior or lateral stability of the bicycle can be enhanced. The lateral stability boundaries of a bicycle as a function of forward

speed are defined by the eigenvalues as shown in chapter 3. To increase the auto-stable speed region at which the real part of all the eigenvalues are negative, an additional torque can be applied as a function of specific state information. From a practical point of view, it can be beneficial if the lower boundary of the auto-stable speed region can be reduced such that the bicycle shows lateral stable behavior, making the bicycle more easy to control by the rider at a low forward speed.

4-3-1 Low Speed Stabilization

At low forward speeds a typical bicycle tend to behave like an inverted pendulum, it capsizes from an initial upright position if no control torques are applied. To overcome this undesired roll motion, turning the handlebar into the undesired fall uprights the bicycle again by moving the center of gravity back above the wheels. Or more specifically, moving the wheels back underneath the center of gravity.

This undesired capsize motion is relatively fast so a steer torque relation proportional to the roll rate $\dot{\phi}$ is proposed for speeds below $v_{avg}=5$ m/s. This control strategy is adopted from a recent publication by [Schwab et al., 2008], originally proclaimed Intuitive Control, hereby to be referred to as Low Speed Stabilization control. Subsequently, the torque relation T_{SE} proposed is proportional to the roll rate $\dot{\phi}$ and the forward speed v of the bicycle. The magnitude of this speed dependency is gradually decreased in magnitude up to v_{avg} , as no stabilizing control is required inside the auto-stable speed region. At higher forward speeds no stabilizing control torque is applied, as the unstable capsize mode is relatively slow and easy to control. This leads to the following control algorithm shown in equation 4-13 and block diagram 4-6.

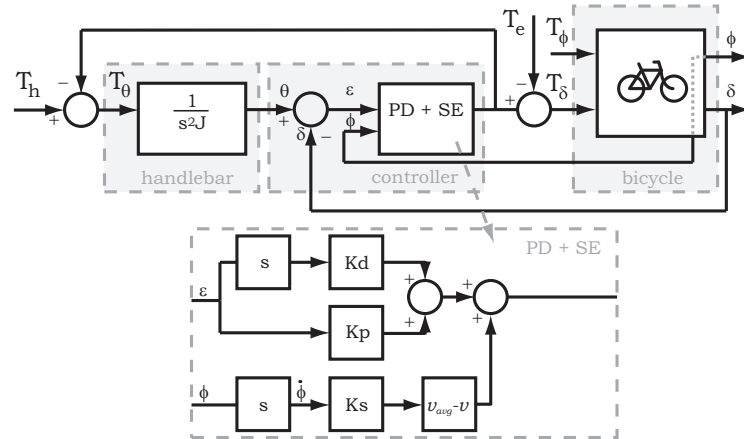


Figure 4-6: A block diagram for the steer-by-wire bicycle which includes the combined handlebar tracking controller (PD) and low speed stabilization controller (SE).

$$T_{SE} = K_s(v_{avg} - v)\dot{\phi} \quad (4-13)$$

Applying the stabilizing control torque T_{SE} to the Steer-by-Wire Bicycle model for which the

forcing term \bar{f} becomes as shown in equation 4-14,

$$\bar{f} = \begin{bmatrix} T_h - T_{PD} \\ 0 \\ T_{PD} + T_{SE} \end{bmatrix}. \quad (4-14)$$

By applying the stabilizing control torque relation given in equation 4-13, the weave speed lowers from 4.3 m/s to about 1.0 m/s for $K_s=10 \text{ Ns}^2/\text{rad}$, without negatively affecting the capsize speed. The eigenvalue plot for this control algorithm is shown in figure 4-7 and clearly shows the increased stable speed range. This is also demonstrated by the time simulations in figure 4-4a and 4-4b.

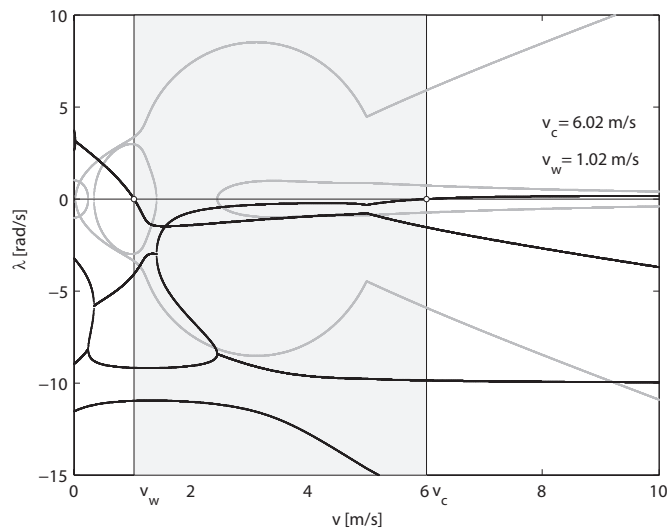


Figure 4-7: Eigenvalues λ for the lateral motion of the Steer-by-Wire Bicycle model utilizing the Low Speed Stabilization (SE) enhancement algorithm as a function of forward speed v in the range $0 \text{ m/s} < v < 10 \text{ m/s}$ (a).

The time simulations 4-8a and 4-8b show the lateral response for the stability enhanced (SE) Steer-by-Wire Bicycle model at a forward speed at 5 m/s and 3 m/s, when subjected to a roll disturbance perturbation of 50 Nm. Compared with the time simulations of the Steer-by-Wire Bicycle model, the lateral response at 3 m/s now shows a stable decaying motion as predicted.

4-4 Pole Placement

The dynamic response of the bicycle is defined by the state matrix \mathbf{A} in which the eigenvalues and eigenmodes determine the physical response to a particular input. As the state matrix is a function of the physical properties of the bicycle, changing the entries in this matrix, or more specific the eigenvalues or poles, gives the bicycle a different dynamic response.

A Pole Placement technique can be used for single input systems to place the eigenvalues at any desired location. Suppose that the system is controllable $\text{rank}(Q) = n$, we have the

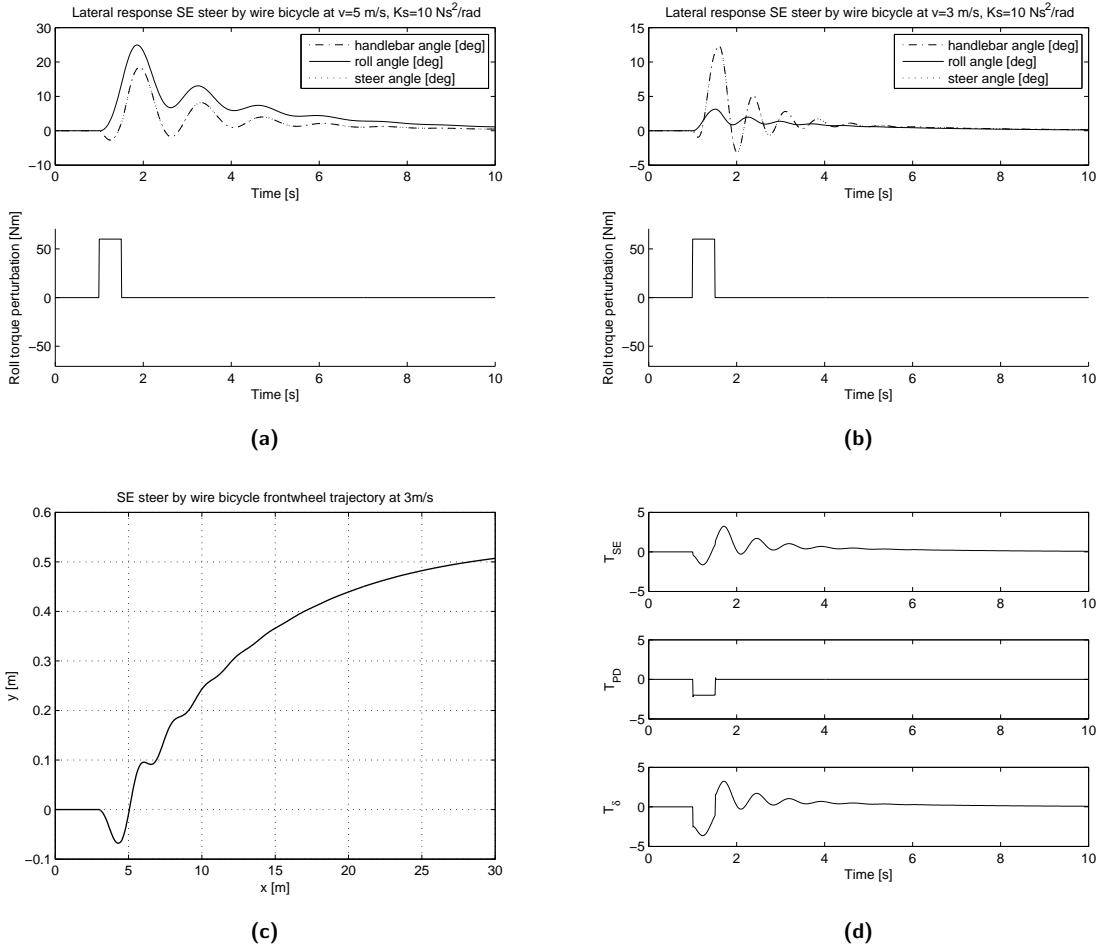


Figure 4-8: A time simulation (a) of the lateral motion of the Steer-by-Wire Bicycle model utilizing the Low Speed Stabilization (SE) enhancement algorithm to a 50 Nm roll perturbation at a forward speed range of $v = 5$ m/s which shows a stable decaying roll- and steering motion. The time simulation (b) at $v = 3$ m/s now also shows a stable decreasing roll- and steering motion, unlike previous simulations without the stability enhancement control. The ground trajectory of the front wheel contact patch (c) for the -2 Nm steer perturbation at 3 m/s shows no unstable behavior. The steering wheel actuator torque T_{PD} combined with the Stability Enhancement control torque T_{SE} specifies the steering actuator output torque T_{δ} (d).

following characteristic polynomial for a particular bicycle configuration as shown in equation 4-15,

$$\det(sI - A) = s^n + a_1 s^{n-1} + \dots + a_{n-1} s + a_n. \quad (4-15)$$

Define a desired characteristic polynomial,

$$\det(sI - A + BK) = s^n + \bar{a}_1 s^{n-1} + \dots + \bar{a}_{n-1} s + \bar{a}_n. \quad (4-16)$$

Then the required state feedback law is defined as,

$$K = [\bar{a}_n - a_n | \bar{a}_{n-1} - a_{n-1} | \dots | \bar{a}_1 - a_1] T. \quad (4-17)$$

Where T is defined as,

$$T = [Q]^{-1} \begin{bmatrix} a_{n-1} & a_{n-2} & \dots & a_1 & 1 \\ a_{n-2} & a_{n-3} & \dots & 1 & 0 \\ \vdots & \vdots & & \vdots & \vdots \\ a_1 & 1 & \dots & 0 & 0 \\ 1 & 0 & \dots & 0 & 0 \end{bmatrix}^{-1} . \tag{4-18}$$

This state feedback law has the form $u = -\mathbf{K}x$ for which gain vector \mathbf{K} specifies the feedback gains which is a function of forward speed v . The feedback gains specified in vector \mathbf{K} define the multiplication factor on each individual entry in the state vector \mathbf{q} . The states specified in \mathbf{q} have to be individually measured for the controller to calculate the required steer torque T_{PP} which is specified as,

$$T_{PP} = \mathbf{K} [\dot{\phi}, \dot{\delta}, \phi, \delta]^T . \tag{4-19}$$

This leads to the following block diagram shown in figure 4-9. This technique makes it possible

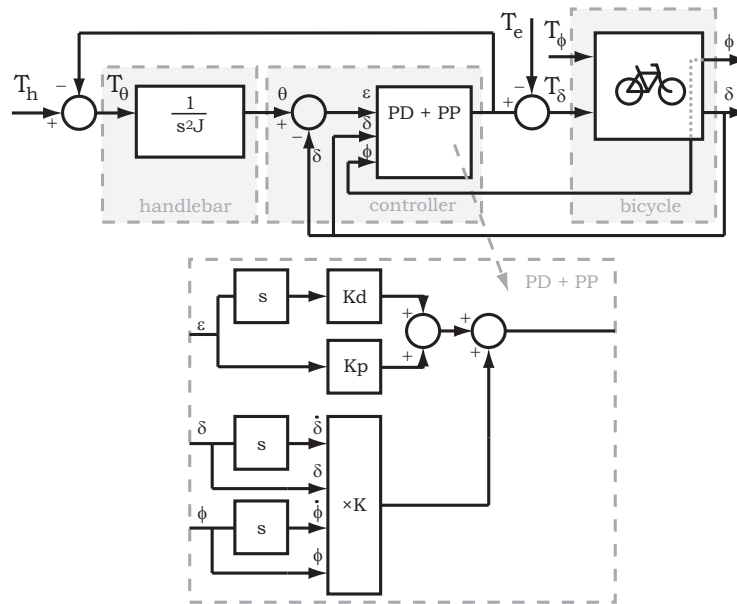


Figure 4-9: A block diagram for the steer-by-wire bicycle which includes the combined handlebar tracking controller (PD) and full state feedback controller (PP).

to virtually change the eigenvalues of the bicycle whose eigenvalues are otherwise determined by the physical configuration of the bicycle. The full state feedback uses roll- and steer rates as well as roll- and steer angles as a feedback signal. This implies a virtual change in stiffness and damping can be made to the equations of motion.

To illustrate the possibilities of using the Pole Placement technique, two specific cases are demonstrated:

1. The Virtual Head Angle Bicycle: The dynamic properties of a bicycle with a 45 degree head angle are assigned to the control action of the Steer-by-Wire Bicycle model which has a physical 18 degrees head angle. It will be shown that the Steer-by-Wire Bicycle model shows similar lateral stability properties as compared to a bicycle having a virtual 45 degrees head angle.
2. Stable Backwards Bicycle: The dynamic properties of a stable forward driven bicycle are assigned to the control action of the Steer-by-Wire Bicycle model which is driven backwards. It will be shown that the backwards driven Steer-by-Wire Bicycle model can be stabilized, showing similar lateral stability properties as compared to the forward driven bicycle.

4-4-1 Virtual Head Angle Bicycle

The difference between the Benchmark Bicycle model using a 18 degrees and a 45 degrees head angle is shown in figure 4-10a and 4-10b respectively.

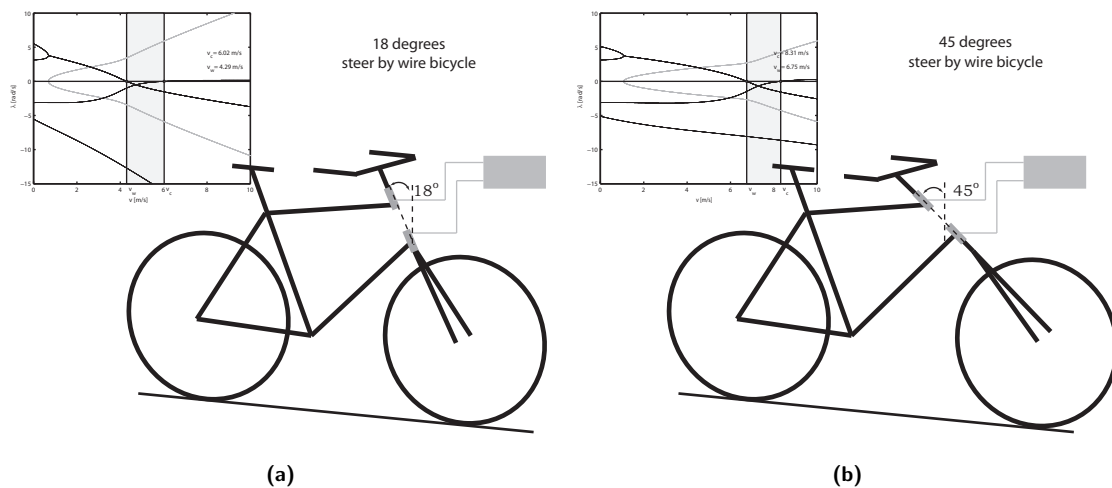


Figure 4-10: Changing a single physical parameter like the head angle from 18 degrees (a) to 45 degrees (b) has a significant effect on the lateral stability of the bicycle. The bicycle with the 18 degrees head angle shows lateral stable motion from 4.3 m/s to 6.0 m/s whereas the bicycle with the 45 degrees head angle shows lateral stable motion from 6.8 m/s to 8.3 m/s.

The Steer-by-wire Bicycle model with the 18 degrees head angle corresponds with the physical layout of the Benchmark Bicycle model where the weave- and capsize speeds are at 4.3 m/s and 6.0 m/s. Whereas for the chopper-like 45 degrees head angle bicycle the weave- and capsize speeds have changed to 6.8 m/s and 8.3 m/s. The increase in head angle has caused the stable speed range to shift upwards with about 2.5 m/s.

The dynamic properties of the 45 degrees head angle bicycle can be programmed in the physical 18 degrees head angle bicycle if the appropriate control algorithm is utilized by the steer-by-wire bicycle controller. The full state feedback gain vector \mathbf{K} to be used by the control algorithm as a function of forward speed is shown in figure 4-11a, which results in an artificial eigenvalue plot shown in figure 4-11b whose dynamic behavior corresponds to the 45 degrees head angle bicycle.

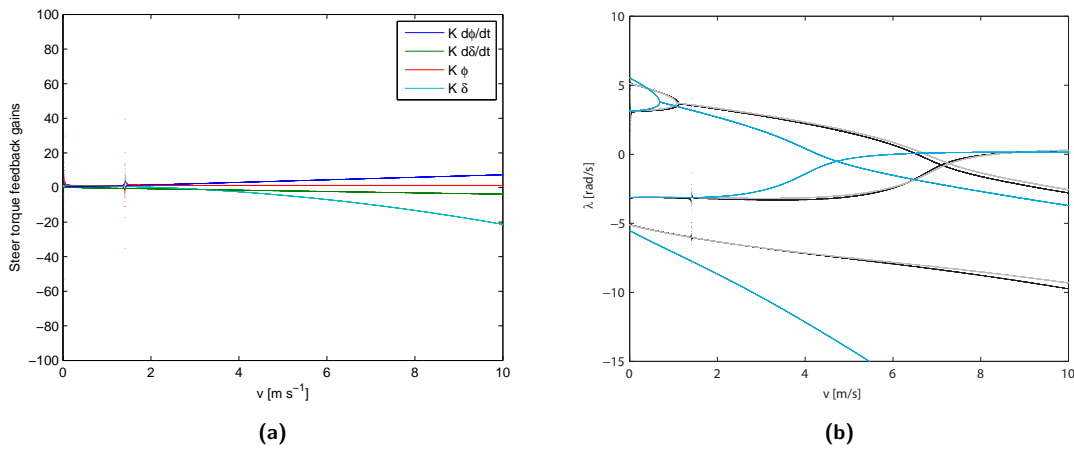


Figure 4-11: Steer actuator feedback gains K as a function of forward speed v (a) used to map the eigenvalue plot of the 45 degrees head angle bicycle on to the physical 18 degrees steer-by-wire bicycle. The resulting eigenvalue plot of the steer-by-wire bicycle utilizing the pole placement control algorithm (b) shown in black superimposed on the eigenvalue plot of the virtual 45 degrees head angle bicycle shown in grey. The original eigenvalue plot of the physical uncontrolled steer-by-wire bicycle is shown in blue.

This shows that the steer-by-wire bicycle with an 18 degrees head angle can be programmed to behave like a bicycle with a virtual 45 degrees head angle. At a forward speed of 7 m/s the bicycle with an 18 degrees head angle would be laterally unstable as shown in figure 4-12a in response to a 20 Nm roll torque perturbation. However as this bicycle is programmed to control the steering wheel actuator using full state feedback, the steer-by-wire bicycle shows lateral stable behavior as if it was equipped with an 45 degrees head angle shown in figure 4-12b.

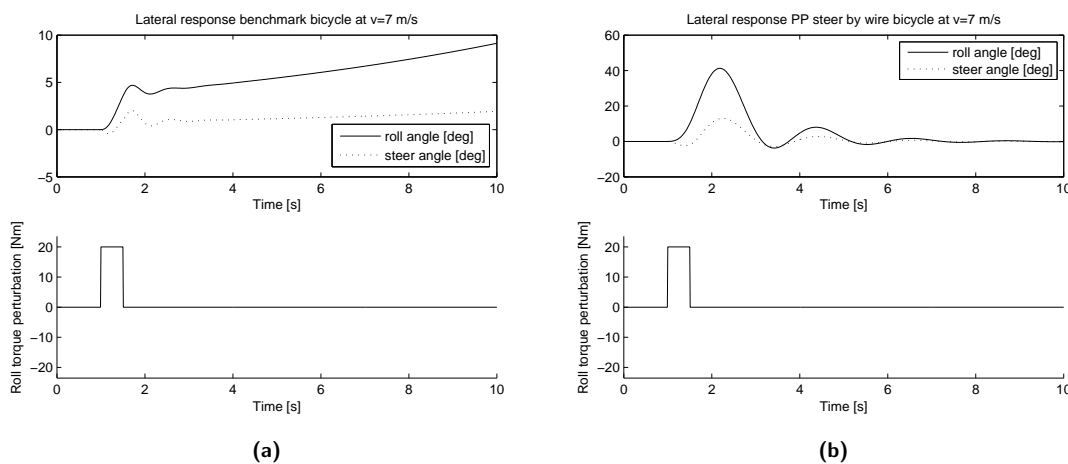


Figure 4-12: The time simulation of the 18 degrees head angle steer-by-wire bicycle at 7 m/s shows an unstable lateral roll- and steer motion. The steer-by-wire bicycle with the pole placement controller using a virtual 45 degrees head angle does show a stable lateral roll- and steer motion at 7 m/s although the bicycle has still a physical head angle of 18 degrees.

4-4-2 Stable Backwards Bicycle

Consider the eigenvalue plot shown in figure 4-13 which shows the eigenvalues of the steer-by-wire bicycle in a speed range from -10 m/s to 10 m/s. The presence of positive real eigenvalues indicate that the bicycle is laterally unstable at negative forward speeds from 0 m/s to -10 m/s. To be more precise, the bicycle will be unstable when driven backwards. As the eigenvalues of the steer-by-wire bicycle can be placed at any desired location using the state feedback technique shown in equation 4-17, the stable properties of the forward driven bicycle can be applied to the backwards driven steer-by-wire bicycle. A physical implementation will be rather impractical but it does illustrate this pole placement technique nicely as the resulting eigenvalue plots of these two bicycle configurations differ substantially. Observe the eigenvalue plots in figure 4-14b and 4-14a.

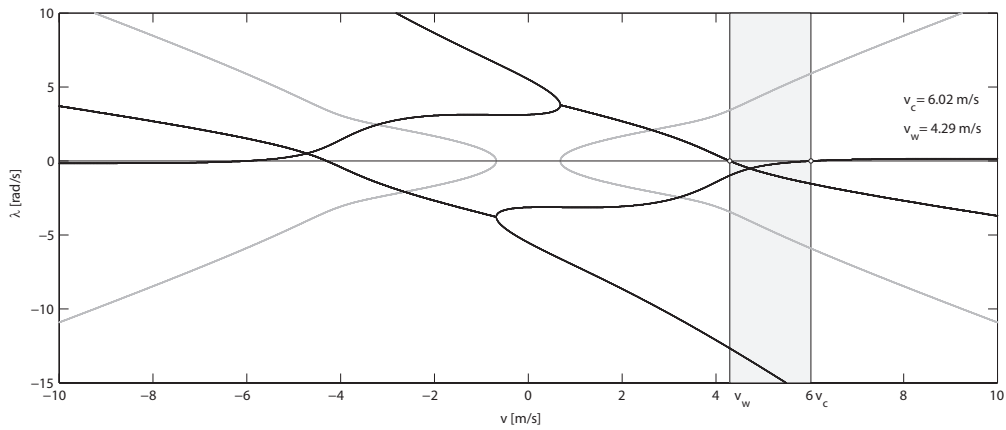


Figure 4-13: Eigenvalues λ for the lateral motion of the steer-by-wire bicycle as a function of forward speed v in the range $-10 \text{ m/s} < v < 10 \text{ m/s}$ (a).

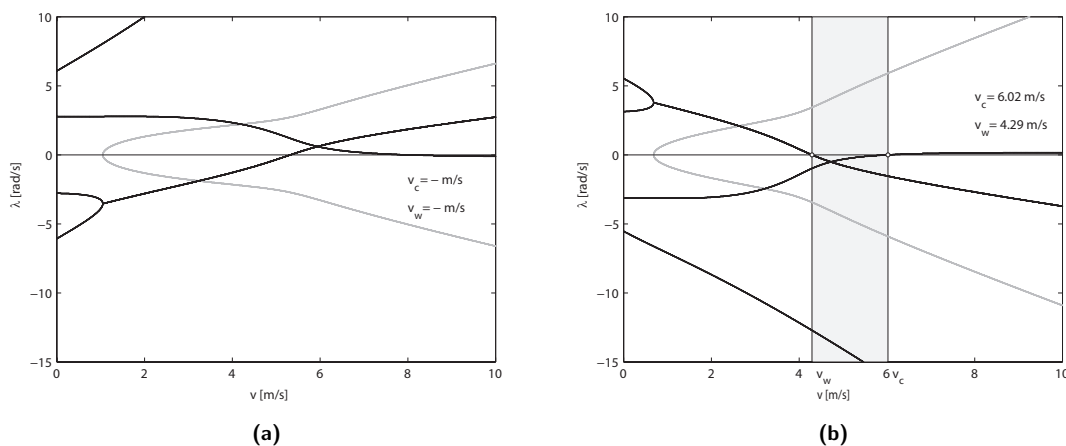


Figure 4-14: Eigenvalue plot of the backwards driven benchmark bicycle (a) which is to be mapped on the steer-by-wire bicycle driven forward (b).

The eigenvalue plot of the forward driven bicycle, having lateral stable dynamic behavior,

could be mapped on the backwards driven steer-by-wire bicycle having lateral unstable dynamic behavior. Applying this technique gives the following feedback matrix \mathbf{K} shown in figure 4-15a and resulting eigenvalue plot shown in figure 4-15b.

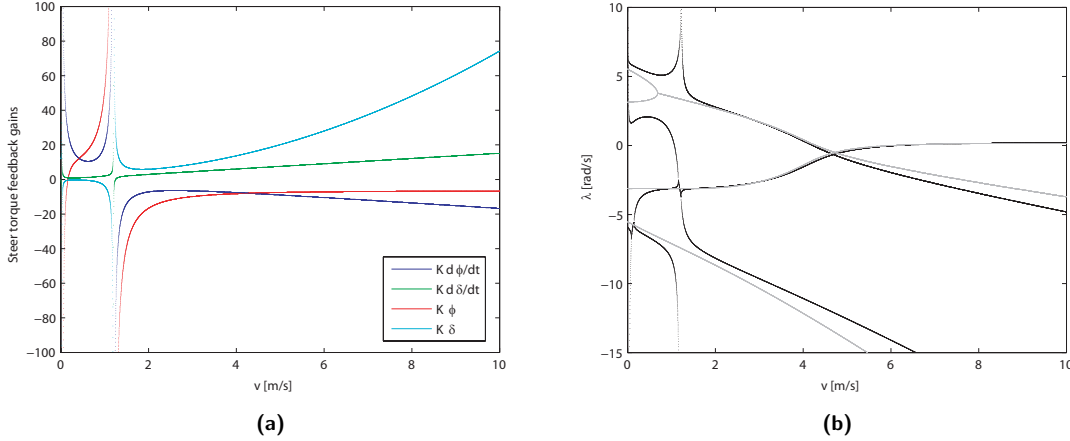


Figure 4-15: Steer actuator feedback gains as a function of forward speed v (a) used to map the eigenvalue plot of the forward driven bicycle on to the backward driven steer-by-wire bicycle. The resulting steer-by-wire eigenvalue plot (b) shown in black superimposed on the forward driven bicycle eigenvalue plot shown in grey.

As in the Virtual Head Angle Bicycle case, two distinct asymptote-like peaks in the feedback gain plot 4-15a can be observed. These peaks correspond to the uncontrollable forward speeds discussed earlier in section 4-1. This is also clearly visible in the eigenvalue plot 4-15b indicated by the relatively large discrepancy of the eigenvalues near the uncontrollable speeds. At higher forward speeds the eigenvalues associated with the weave- and caster-mode also diverge substantially. The discrepancy between the eigenvalues is caused by the fact that the single steering wheel torque input T_δ to the system is used in conjunction with a mass-matrix \mathbf{M} having off-diagonal terms. Input matrix \mathbf{B} in the state equation 3-9 therefore also contains non-zero values other than the steer torque input,

$$\mathbf{B} = \begin{bmatrix} M^{-1}[0, 1]^T \\ 0 \\ 0 \end{bmatrix}. \quad (4-20)$$

The upper most non-zero entry in the input matrix is the addition by the roll torque T_ϕ which is omitted in the pole placement technique due to the only available steer torque input on the bicycle. A comparison between the lateral response due to this discrepancy near 5 m/s is shown in the time simulation in figure 4-16a and 4-16b.

The unstable backwards driven bicycle can be stabilized by the pole placement mapping technique as shown in the time simulations. The lateral response of the controlled bicycle in figure 4-16b corresponds relatively close to the time simulation of the original Benchmark Bicycle model in figure 4-8a. The roll angle has a slight delayed response to the roll angle response for the forward driven Benchmark Bicycle model, although the amplitudes correspond nicely. Despite the lateral response doesn't exactly correspond to the dynamic behavior for the forward driven bicycle, the pole placement technique does show great potential in modifying

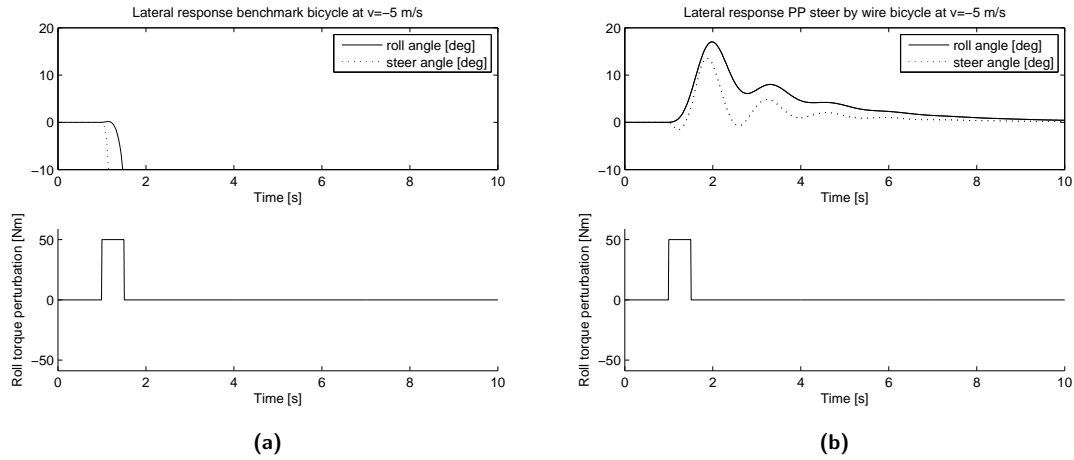


Figure 4-16: A time simulation (a) of the unstable lateral motion of the backwards driven bicycle to a 50 Nm roll perturbation at $v = -5$ m/s. When applying the pole placement technique to the backwards driven bicycle with the dynamic properties of the forward driven bicycle, the lateral response becomes stable (b) and corresponds similarly to the one found in figure 4-4a.

the dynamic properties originating from virtual properties without physically changing the bicycle.

4-5 Steer Torque Feedback

A bicycle rider perceives information on the state of the bicycle by three individual sensory inputs regarding movement control. Visual cues provide the rider information on the forward speed, horizon tilt and the trajectory of the current path. The vestibular system located behind the ears is able to measure the acceleration in three dimensional space, providing the rider cues regarding change in speed and ultimately the physical direction. The proprioceptive system in the human body is able to provide cues on the strength being employed in movement, the ability to sense the tension or strength in the human muscles.

A bicycle rider utilizes a combination of the aforementioned sensory inputs to control the motion of the bicycle. Numerous studies found in literature on vehicle control cover the importance and contribution of the sensory inputs as shown by [Gordon, 1966]. It was shown that steer torque feedback as well as transverse accelerations are rated of most important just after vision. In literature one can distinguish research on the tracking performance of the decoupled steering system [Bertoluzzo et al., 2007], and research on the ability of a steer-by-wire system to provide a realistic steering feel at the handlebars [Amberkar et al., 2004]. The latter aspect is covered in the following section as the steering feel of the steer-by-wire is characterized and compared to a conventional steered bicycle.

The mechanical connection between the handlebars and the steering assembly on the steer-by-wire bicycle, is replaced with an artificial stiffness and damping defined by the PD-controller parameters, the steering feel as perceived by the driver can be influenced by changing these controller parameters. The focus on steer torque feedback is primarily aimed at providing a steering feel as if the bicycle was equipped with a mechanical steering shaft.

The state space representation of the steer-by-wire bicycle can be conveniently expressed in the frequency domain. Applying the Laplace transform on 3-9 and 3-10 and rearranging yields a relation between the output $\mathbf{Y}(s)$ to the input $\mathbf{U}(s)$ of the system:

$$\mathbf{H}(s) = \mathbf{Y}(s)/\mathbf{U}(s) = C(s\mathbf{I} - A)^{-1}B + D \quad (4-21)$$

Now the steer stiffness is defined as the relation between the required torque T_θ in $\mathbf{U}(s)$ to the angle θ in $\mathbf{Y}(s)$. The change in handlebar angle θ and the handlebar actuator torque T_θ for the Steer-by-Wire Bicycle model can be expressed in the following transfer function,

$$H_{SBW}(s) = \frac{T_\theta(s)}{\theta(s)} \quad (4-22)$$

whereas the change in steering angle δ and the steer torque T_δ for the Benchmark Bicycle model is expressed as,

$$H_{BB}(s) = \frac{T_\delta(s)}{\delta(s)}. \quad (4-23)$$

The magnitude and phase relationship between the drivers handlebar angle and perceived steer torque can change significantly as a function of input frequency as well as the forward speed of the bicycle. The PD-controller stiffness- and damping properties between the handlebar- and steering assembly also have a significant contribution to the steering feel, as the PD-controller itself shows a frequency dependant stiffness relation.

Figure 4-17b shows the steer stiffness relation $H_{SBW}(s)$ for the Steer-by-Wire Bicycle model in grey at a forward speed of 3 m/s. The steer stiffness relation $H_{BB}(s)$ of the Benchmark Bicycle model is shown in black having PD-controller parameters with a bandwidth of 300 rad/s at an identical forward speed of 3 m/s. The relative low torsional stiffness provided by the PD-controller on the Steer-by-Wire Bicycle model as compared to the mechanical connection of the Benchmark Bicycle model will not provide an identical steering feel at higher frequencies. Realistic steer frequencies however are generally below 3 Hz this should not have a significant implication on the steering feel of the steer-by-wire bicycle.

A change in forward speed v of the bicycle however, also has a significant effect on the steering feel properties. The steer stiffness magnitude relation as function of forward speed of the benchmark bicycle is shown in figure 4-18a whereas the steer stiffness magnitude relation of the steer-by-wire bicycle is shown in figure 4-18b.

From the linearized equations of motion for the benchmark bicycle given in 3-1, it is shown that the damping-like matrix $\mathbf{C1}$ is a function of forward speed v , whereas the stiffness-like matrix $\mathbf{K2}$ is a quadratic function of forward speed v . The benchmark bicycle steer stiffness magnitude plot shown in figure 4-18a shows some interesting properties with respect to the torque the rider has to apply at the handlebars as a function of steer frequency and forward speed of the bicycle.

At zero forward speed, matrices $\mathbf{C1}$ and $\mathbf{K2}$ are zero. The steer stiffness is therefore primarily defined by the mass matrix \mathbf{M} and stiffness-like matrix $\mathbf{K0}$. The steer stiffness at low frequencies is defined by the entries in matrix $\mathbf{K0}$ whereas at higher frequencies the

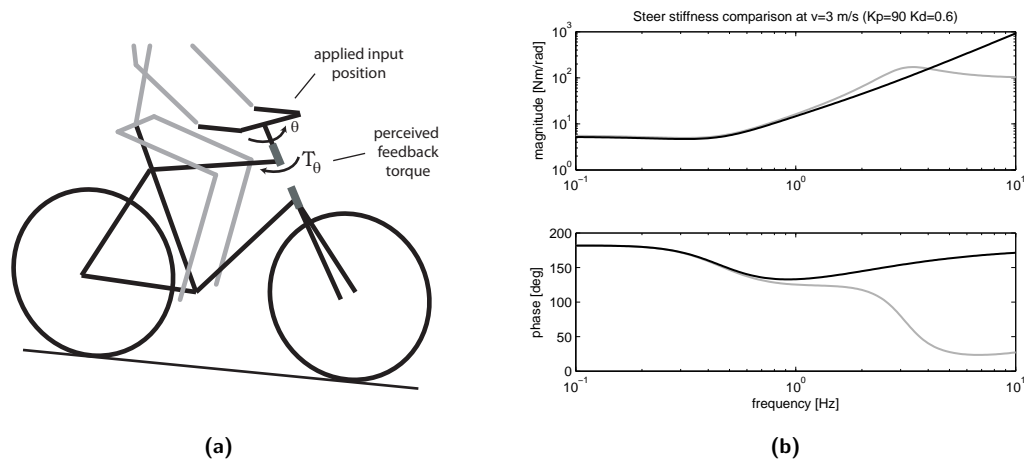


Figure 4-17: The steer stiffness (a) as perceived by the driver on the steer-by-wire bicycle as a function of the handlebar position. The magnitude and phase relation (b) at a forward speed of 3 m/s is shown for the Steer-by-Wire Bicycle model having a PD-controller bandwidth of 300 rad/s in grey and the Benchmark Bicycle model in black. At higher steer frequencies the Steer-by-Wire Bicycle does not provide a realistic steering feel as compared to a conventional bicycle.

mass- and inertia properties in matrix \mathbf{M} become dominant shown by the typical 40 dB per decade slope. As forward speed v increases, the contribution of v in $\mathbf{C1}$ and especially the quadratic expression of v in $\mathbf{K2}$ becomes relevant. A resonant-like downward peak appears at the weave-speed of 4.29 m/s. The coupling between the roll- and steer equation can result in a specific mode at which the bicycle oscillates between leaning left and steering right and the other way around. At the weave-speed the phase relation between the handlebar- and roll motion causes a significant drop in steer stiffness if the handlebars are rotated at a frequency equal to the the weave frequency. At higher forward speeds the weave frequency increases which is illustrated by the upward shift of the resonant-like steer stiffness peak whose magnitude simultaneously increases. An anti-resonance like upward peak appears for the steer-by-wire bicycle at around 3 Hz and low forward speeds caused by the damping- and stiffness coefficients of the PD-controller and mass properties as defined in mass matrix \mathbf{M} . At higher forward speeds the anti-resonance-like peak is reduced in magnitude due to the speed dependant term in the damping-like matrix $\mathbf{C1}$ which increases thereby reducing the anti-resonance-like peak.

In order to provide a steering feel at the handlebars of the steer-by-wire bicycle, identical or at least as close as possible to a conventional steered bicycle, the PD-controller coefficients should be chosen appropriately. Primarily at higher steer frequencies the PD-controller stiffness- and damping coefficients define the steer-stiffness in relation to the mass- and inertia properties of the bicycle and additional handlebar body. Especially resonant modes- and frequencies associated with the PD-controller coefficients should be avoided or placed at a frequency, high enough and well outside the operating range with respect to realistic steer frequencies.

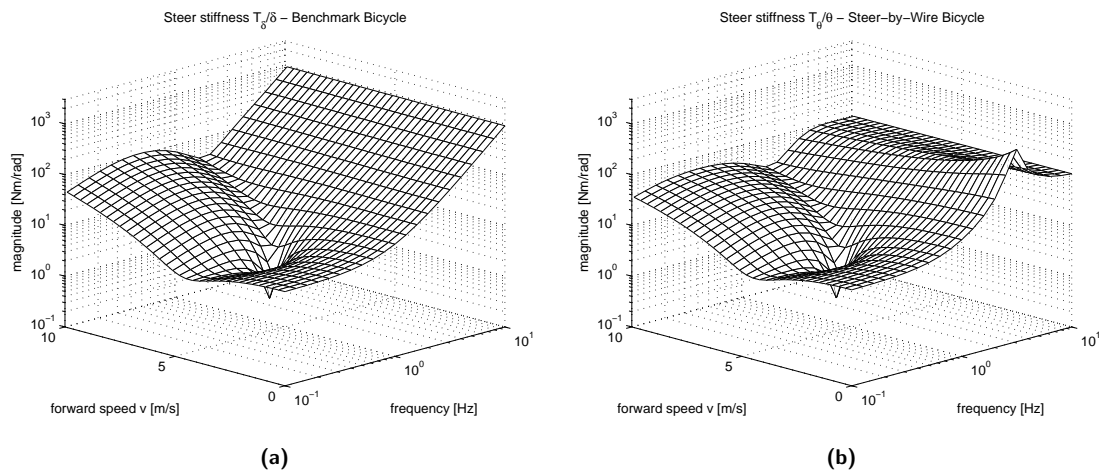


Figure 4-18: The steer stiffness magnitude relation as perceived by the rider as a function of forward speed on the benchmark bicycle (a) and the steer-by-wire bicycle (b). The steer stiffness at the handlebars changes significantly as a function of input frequency as well as the forward speed of the bicycle. At higher frequencies the steer stiffness is primarily defined by the mass- and inertia properties of the bicycle. A significant drop in the steer stiffness magnitude relation occurs at the weave speed and weave frequency of the bicycle shown by the downward resonance-like peak. The steer stiffness of the steer-by-wire bicycle at higher frequencies are primarily defined by the stiffness and damping properties of the PD-controller, whereas the anti-resonance-like upward peak at low forward speeds is caused by the PD-controller coefficients and the mass- and inertia properties defined in the system matrix.

4-6 Summary

In this chapter some of the capabilities of a steer-by-wire system are shown by time simulations performed on the previously defined Steer-by-Wire Bicycle model and additional control algorithms. First the coupling of the handlebar motion to the bicycle steering motion is characterized by suitable scaling of the PD-controller coefficients. Additional controller algorithms are introduced in the Lateral Stability Enhancement and Pole Placement sections. The Lateral Stability Enhancement algorithm shows the capability to stabilize the lateral motion of a bicycle by reducing the weave speed of the bicycle substantially. The controller algorithm provides an additional control torque at the steering assembly based on state information provided by the forward speed- and roll rate-sensor of the bicycle. A more advanced approach using a pole placement algorithm, shows that the steer-by-wire bicycle can be equipped with a virtual geometry- and mass distribution and corresponding dynamic behavior by feedback of the roll- and steering motions and appropriate scaling of each individual parameter to calculate the required additional control torque. The effect of a decoupled handlebar assembly and the relation of the virtual stiffness- and damping properties of the PD-controller coefficients on the steering feel properties are shown. The steering feel properties of a conventional bicycle and the steer-by-wire bicycle are graphically shown by the magnitude plot of the required steer torque as a function of steer frequency as well as the forward speed of the bicycle. The following chapter will cover the actual implementation of a steer-by-wire system on a bicycle which will subsequently be used to evaluate the above mentioned aspects experimentally.

Steer-by-Wire Implementation

The simulation results shown the previous chapters indicate the ability to enhance the lateral stability of the bicycle by active torque control along the steering axis. A natural progression is to validate the control algorithms on an actual bicycle equipped with a steer-by-wire system. As no such bicycle exist, the development of this steer-by-wire bicycle prototype is covered in the subsequent chapter.

The design of the steer-by-wire bicycle is subdivided in sections covering the specific physical domains involved in a typical mechatronic system design approach. As shown in figure 5-1a, the steer-by-wire bicycle design approach is based on the interaction between three principal domains; the software-, mechanical- and electronic domain.

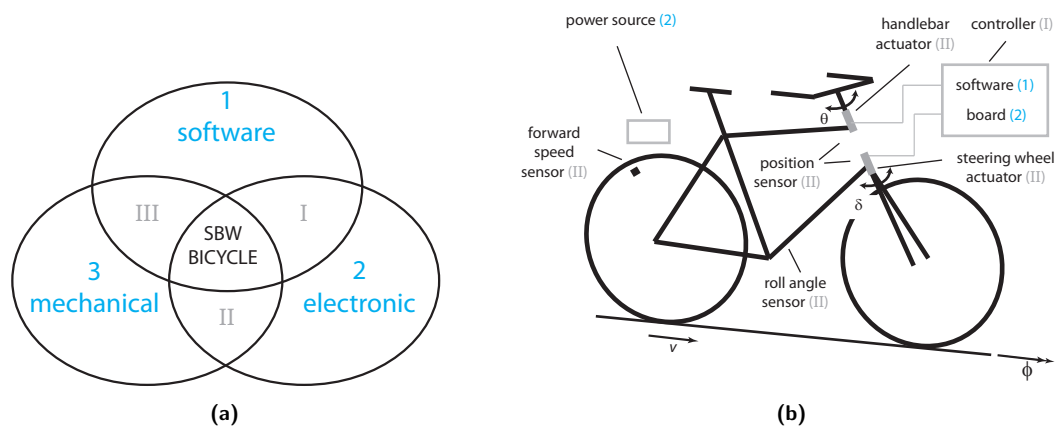


Figure 5-1: A mechatronic system design approach (a) showing schematically the interaction between the three principal domains; software, mechanics and electronics. The originating domain of each component (b) on the bicycle is shown between brackets.

Figure 5-1b shows the various components which will define the steer-by-wire bicycle prototype. Each component is labeled between brackets according to its origin shown in figure 5-1a. The controller (I) running software (1) on the electronic control board (3) interfacing

with the position-, forward speed- and roll angle sensors (II), as well as the handlebar- and steering wheel actuators (II). The controller, sensors and actuators are powered by a portable power source (2).

The three domains interact with each other and subsequently have an influence on the physical selection and implementation. The electronic controller for example, poses a restriction on the available software compiler packages. The mechanical physical layout of the bicycle poses constraints on the electronic motor choice, as well as the limited power storage available given the weight and dimension constraints. Likewise those constraints also apply vice versa, which make individual component selection a function of requirements originating from adjacent domains.

Recent bicycle related research at the TU Delft Bicycle Lab includes study on bicycle dynamics [Kooijman et al., 2008] and rider identification [Kooijman et al., 2009]. A Batavus Browser city bicycle as shown in figure 5-2 has been used extensively during those experiments. Likewise a recent M.Sc. study [van den Ouden, 2011] on the inventory of bicycle motion of a bicycle and rider combination, was performed on the Batavus Browser providing real-world measurement data like steer-torque and three axis motion capturing data using GPS and inertial measurement devices.



Figure 5-2: The Batavus Browser city bicycle will be converted to a steer-by-wire bicycle.

The use of a Batavus Browser bicycle to be converted to a steer-by-wire bicycle is highly suitable as geometrical-, mass- and inertia properties are readily available [Kooijman et al., 2009] for modeling purposes. Even real-world measurement data provided by [van den Ouden, 2011] give valuable and directly applicable numerical data to be used in actuator- and sensor selection. The relaxed riding position assures a comfortable riding experience for a large number of different sized riders while the aluminium frame and luggage carrier provide the required space to accommodate for the controller-, energy storage- and actuator hardware.

The following section will focus on the available software, electronic and electromechanical components in the design of the steer-by-wire bicycle. The programming software will be covered in the Software domain section, the controller hardware and power source selection will be covered in the Electronics section. The Electromechanics will cover both the sensor and actuator hardware.

5-1 Software

5-1-1 Development tool selection

The positioning of the software domain in figure 5-1a on top is not unintentional as this is the foundation of the steer-by-wire bicycle. The selection of the controller software plays an important role as there are a large number of different programming languages available to be utilized on modern electronic systems. However those many different programming languages can be subdivided in a hierarchical structure based on abstraction level as shown in figure 5-3.

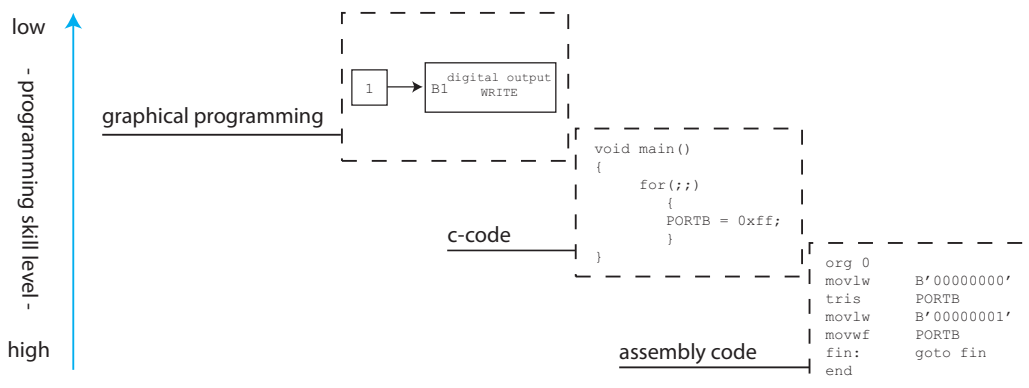


Figure 5-3: Programming code required to turn on a LED for specific programming languages indicating the abstraction level and programming skills required by the user.

Low-level programming languages like Assembly require in dept-knowledge of the actual processor and its specific internal operation. Even individual types from a single supplier within a certain family of processors could require a specific set of programming instructions, requiring experience and knowledge of the specific device. A more accessible and generally applicable way of programming modern electronic controllers is available by high-level programming languages like C-language. C-language programming is a more universal, multi-platform applicable programming language more easily readable and only requires an automatic in-between compilation step, which hides the complex machine-code generation from the user. Still C-programming requires a moderate level of programming experience. An even more accessible way of programming is more graphically oriented without the need to learn specific code or programming routines. Graphical programming based on flowchart-like structures again require an in-between compilation step but is the most easy to master programming technique.

In order to provide a future-proof, easy-to-understand and accessible development platform for the steer-by-wire bicycle prototype, the use of a high level graphical programming language is recommended. In this particular steer-by-wire application a graphical programming language provided as a Matlab Simulink blockset by Lubin Kerhuel¹ is used.

¹More information on <http://www.kerhuel.eu/>

This LK-blockset is a Matlab Simulink toolbox providing predefined function-blocks to gain access to full microcontroller peripheral functionality on 16-bit and 32-bit development hardware developed by Microchip Technology. The LK-blockset running on a development PC has a build in software compiler to generate the necessary C-code which is preceded by a compilation step by the Microchip C30 compiler which generates a programmable hex-file as shown in figure 5-4. The hex-file contains the controller algorithms and is programmed on the controller hardware with the use of a USB-interface. After the hex-file is programmed into the controller the algorithms are stored in non-volatile memory for future stand-alone operation.

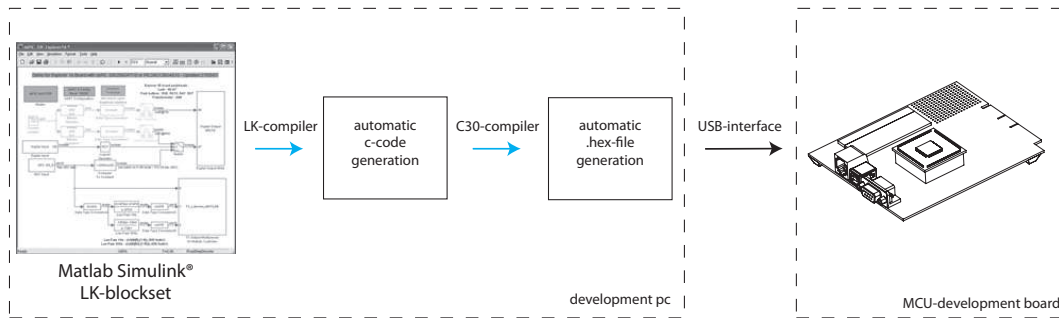


Figure 5-4: Schematic overview of the conversion steps involved for the Matlab Simulink LK-blockset to generate a downloadable hex-file compatible with Microchip 16-bit and 32-bit development hardware.

5-2 Electronics

5-2-1 Controller selection

The electronic controller selection is a function of the aforementioned software programming language compatibility, as well as a few equally important selection criteria. A bicycle in general is a relatively light, compact and mobile vehicle which excludes the use of heavy and large components. More specifically, besides the software programming language, the following additional criteria have to be considered when selecting a suitable controller:

- ▷ The physical weight and dimensions of the controller hardware should be kept as low as possible, as on a relatively small and light vehicle any additional mass and volume will negatively affect the handling of the bicycle in terms of response and rider steer effort.
- ▷ On a mobile, moving vehicle the power source available is usually restricted to direct current (DC) low-voltage power sources based on chemical energy storage. High-voltage alternating current power sources are less suitable, as a wired connection to the mains-power grid would be highly inconvenient. Chemical energy storage by means of (rechargeable) batteries are more suitable providing a direct current voltage source.
- ▷ The controller operates as an interface between the mechanical and electronic domain by various sensors and actuators on the bicycle. The physical number of sensors and actuators define the required number of input- and output channels (I/O's) on the

controller. If analog sensors are to be used there should be suitable analog-to-digital control (ADC) channels available to convert each individual analog signal to a digital value for the controller for internal calculations and processing. Vice versa, the control of actuators generally require an analog output on the controller by digital-to-analog (DAC) channels. High power actuators usually require an additional amplifier stage as the controller itself is not able to provide sufficient power.

Controller hardware in general can be visualized in three categories as show in figure 5-5. PC-based controller hardware, Dedicated embedded hardware and MCU-development hardware. PC-based controller hardware is based on the processing power of a personal computer or laptop, providing the required I/O connections by additional hardware connected via the USB-interface. The I/O hardware is equipped with signal conditioning circuitry and provides input protection to over-voltage. Dedicated embedded controller hardware provides the same level of I/O connections and predefined input protection, however the control algorithms are running on a embedded processor. MCU (Micro Controller Unit) development hardware is an even more compact solution providing access directly to the pins of the embedded microcontroller running the control algorithms without the predefined signal conditioning and input protection. This stripped-down approach allows for a more integrated design tailored to each specific application. At the expense however, of more in-dept knowledge requirement on electronic circuit design as usually an application specific interface board has to be implemented.



Figure 5-5: A visual comparison between different controller hardware solutions. Each having its own specific strengths and weaknesses in terms of size, weight, I/O connectivity, purchase price and performance.

Table 5-1 shows a comparison between the three controller hardware solutions as a function of relevant steer-by-wire bicycle design properties. Each hardware solution is able to run on a low-voltage DC power-source and can be programmed using a graphical programming language provided by their respective manufacturers. High priority selection criteria are weight, size, I/O connections, purchase price and performance.

Based on these five selection criteria, a modular 16-bit microcontroller development board provided by Microchip technology is selected to be used as the primary controller for the steer-by-wire bicycle. The Microchip Explorer16 development board shown in figure 5-6 is a small 145 mm x 115 mm printed circuit board based on a dsPIC33FJ256GP710 microcontroller placed on a removable carrier-board. The controller is powered from a 12 V DC power

Criteria	PC-based hardware	Dedicated embedded hardware	MCU-development hardware
Size	large	average	compact
Weight	significant	average	small
I/O connectivity	predefined	predefined	customizable
Purchase price	high	high	low
Performance	high	high	average

Table 5-1: A comparison between different controller hardware solutions regarding relevant selection criteria in a steer-by-wire bicycle application.

source while the onboard 3.3 V and 5 V linear voltage regulators supply power to the microcontroller and additional circuitry. The Explorer16 development board is equipped with an onboard programmer which interfaces to the development PC in order to download the controller algorithms to the microcontroller. A serial RS232 connector can be used to interface the microcontroller with a personal computer for data logging or troubleshooting purposes. Although there is no use for it on the steer-by-wire bicycle, the development board is also equipped with an alpha-numeric Liquid Crystal Display, four push-buttons and eight Light Emitting Diodes (LED's).

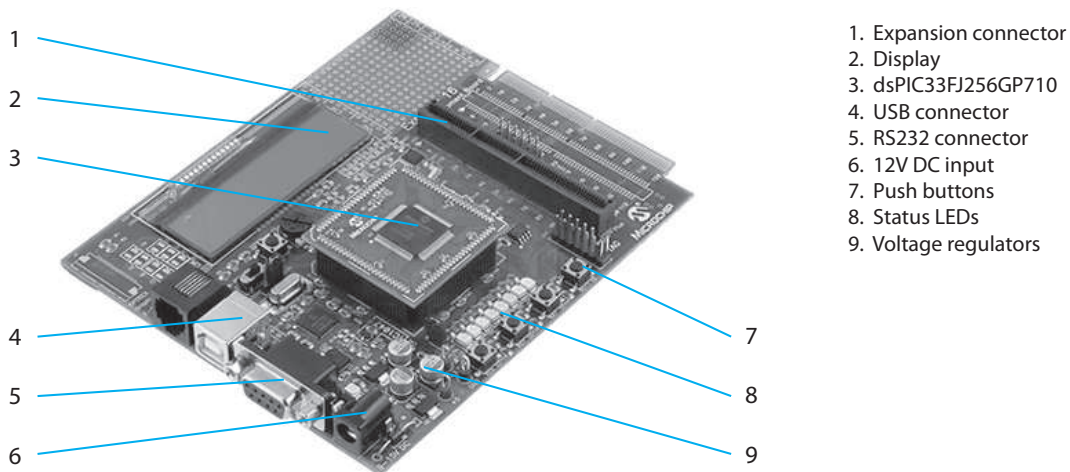


Figure 5-6: The Microchip Explorer16 development board utilizing a 16-bit dsPIC33FJ256GP710 microcontroller will be used as the main controller to interface with the sensors and actuators on the steer-by-wire bicycle prototype.

A 100-pin 16-bit Microchip dsPIC33FJ256GP710 microcontroller is used, which provides the required number of analog and digital I/O's, processing speed and software compiler compatibility with the Matlab Simulink LK-blockset. The microcontroller is able to operate at a clock-frequency of 80 MHz which provides a code execution speed of 40 million instructions per second. The microcontroller is equipped with 12-bit ADC channels with a maximum sampling frequency of 500 kHz.

As the microcontroller development board gives access to the basic I/O pins of the microcontroller in specific situations input protection, level switching or additional circuitry is required. As the development board is equipped with an expansion connector, the microcontroller can be connected to an additional IO-board which takes care of the previous mentioned signal con-

ditioning and provides room for the interface terminals as shown in figure 5-7 for connection to sensors and actuators.

5-2-2 IO-board design

For the steer-by-wire bicycle prototype, additional electronic circuitry is needed to protect the microcontroller from over-voltage originating from sensor outputs and subsequent analog voltage scaling as the ADC-module on the microcontroller can only tolerate voltages up to a maximum of 3.3V. A custom IO-board is designed and fabricated to interface with the MCU-development board as shown in figure 5-7. As well as interface terminals to connect sensors and actuators (labeled A to T) , additional audible warning capability is added by a buzzer, visual status indication is provided by a bi-color LED and user interaction is provided by two push-buttons placed on the IO-board. Operation of the status-LED, buzzer and push-buttons are full software configurable allowing for a highly flexible controller platform to be used in the steer-by-wire bicycle.

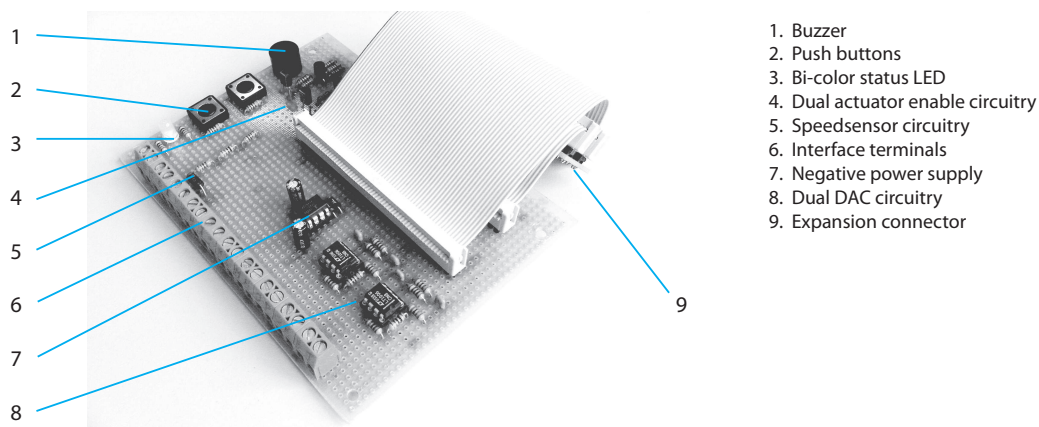


Figure 5-7: A custom designed IO-board to be placed on top of the Microchip development board provides room for the interface terminals and signal conditioning circuitry. Electrical connection is realized from the IO-board by a 60-pin flatband cable to the expansion connector of the MCU-development board.

In the following sections more detailed information will be given on sensor- and actuator selection which will show the need for the actuator-enable circuitry and DAC circuitry as shown in figure 5-7. A comprehensive layout and circuit description of the IO-board is given in Appendix B-1 however, the enable-circuitry and DAC circuitry will be covered in the following section.

Enable circuitry

The enable-circuitry is implemented to provide a 12V output to a power amplifier which enables or disables the actuators on the bicycle. A high logic-level signal on a typical microcontroller in general is only 3.3V which does not trigger the high signal threshold on the power amplifier enable-input which should be higher than 9V. In order to increase the voltage

level output on a microcontroller pin, a transistor can be used to drive an external 12 V signal as shown in figure 5-8a.

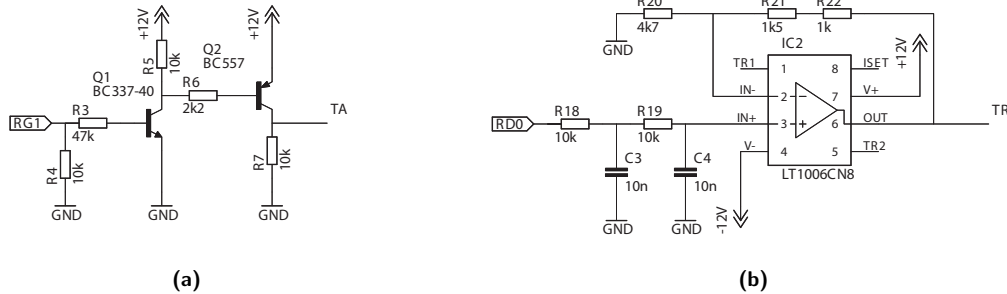


Figure 5-8: The enable-circuitry (a) on the IO-board used to convert a logic-level 3.3 V microcontroller signal [RG1] to a 12 V output signal [TA] capable of triggering the power amplifier enable-input, based on a cascaded NPN-PNP transistor pair. The DAC-circuitry (b) used to convert a high-frequency PWM microcontroller signal [RD0] to an analog output voltage [TR] able to drive the power amplifiers based on a double first-order low-pass filter op-amp circuit.

For safety reasons however, the 12 V output provided at the interface terminal [TA] of the IO-board should be pulled to ground if no voltage on the microcontroller is present or if the output pin is left floating, which is the case during the initialization phase just after power-up of the microcontroller. The use of a NPN transistor as a switch also means the signal is inverted which is unfavorable as the output should be high instead if the microcontroller output-pin is high. To overcome this phenomena a second PNP transistor is placed behind the NPN transistor whose base is connected to the collector of the PNP transistor. A 12 V signal on the emitter of the PNP transistor is only present if the microcontroller output RG1 is high, otherwise the voltage on the A-terminal is pulled low by the 10 kΩ resistor. This ensures a fail-safe mechanism which disables the operation of the actuators in case the controller has not yet active control over the DAC circuitry which defines the torque request to the actuators.

DAC circuitry

The DAC-circuitry is used to provide a 0 V to 5 V analog voltage signal to the amplifier to control the amount of steer torque. The microcontroller has no build-in DAC module to provide an analog voltage, however the microcontroller does have a build-in hardware Pulse-Width Modulation (PWM) module which can be coupled to some additional circuitry to provide an analog output voltage.

Pulse-width modulation is defined as a rapid high-low voltage sequence with a fixed frequency and variable high-low ratio. This implies that the voltage supplied by the PWM-module of the microcontroller is either 0 V or 3.3 V, while the average voltage over time is defined by the high-low ratio or duty-cycle. The duty-cycle is usually expressed in percentage of the period in which the signal is high. The average voltage over time has a linear relation with the duty-cycle of the PWM-signal. If a suitable filter is used a true variable analog voltage can be generated by changing the duty-cycle on the microcontroller PWM-module.

A passive low-pass RC-filter can be used to filter the PWM-signal with the use of a resistor-capacitor pair. As shown in figure 5-8b the resistor (R18) and capacitor (C3) pair operates as

a first-order low-pass filter on the PWM-signal supplied by the microcontroller RD0 output. In the frequency domain the resistor-capacitor pair operates as a voltage divider as defined by,

$$V_{C3}(s) = \frac{1}{sRC + 1} V_{RD0}(s) \quad (5-1)$$

Where V_{C3} is the output voltage across the capacitor, R is the resistance of resistor R18, C is the capacitance of capacitor C3 and V_{RD0} the voltage supplied by the PWM-output of the microcontroller. The transfer function from the output voltage V_{C3} to the input voltage V_{RD0} is defined by,

$$H_{LP1}(s) = \frac{V_{C3}(s)}{V_{RD0}(s)} = \frac{1}{sRC + 1} \quad (5-2)$$

The combination of R and C values in the denominator of the transfer function define the time constant of the signal response. In order to have a fast dynamic response the values should be chosen suitably. However the scaling of the R and C values are a tradeoff between high frequency amplitude attenuation and time response. A fast time response requires a relatively small product of R and C values, however this also implies a smaller high frequency signal attenuation.

Given a specific requirement on signal response or time constant, the signal amplitude attenuation is a function of the PWM-signal frequency. A higher PWM-signal frequency will lead to a higher signal amplitude attenuation which reduces the voltage oscillation on the filter output. The microcontroller is able to generate PWM-signals with a frequency of up to 20 MHz by its hardware PWM-module. However as the microcontroller operates at a maximum clock frequency of 40 million instructions per second, the resolution res_{pwm} of the PWM-signal duty-cycle is a function of the PWM-frequency f_{pwm} as defined by,

$$res_{pwm} = \frac{f_{pwm}}{40 \times 10^6} \quad (5-3)$$

The resolution of the PWM-signal duty-cycle defines the analog voltage resolution at the filter output and subsequently the steer-torque resolution of the actuators. The steer-torque resolution is a very important property involved in haptic steering feel. To provide a realistic steering feel the steer torque resolution should be scaled appropriately.

In [Newberry et al., 2007] research has been done on a quantitative formulation of driver perception on steering feel. Experiments on a simulator including a steering wheel and integrated torque measuring equipment show, a correlation between the minimum distinguishable- and applied steer torque level. It was found that a 15 percent threshold detection for steady-state steering wheel force was determined. In order to provide a control signal to the steer-by-wire bicycle actuators allowing for a realistic steering feel with respect to torque resolution, the PWM duty-cycle resolution should at least be equal to or smaller than 15 percent.

If the PWM-frequency is set at 100 kHz the PWM-signal duty-cycle resolution according to 5-3 is equal to 0.25 percent which greatly exceeds the minimum required threshold found by [Newberry et al., 2007]. Simulations based on a 100 kHz PWM-frequency signal in combination with the filter values for R18 and C3 shown in figure 5-8b, produces an analog output

voltage as shown in figure 5-9a. Measurements² on the first order filter as shown in figure 5-9b show close correspondence to the simulation results as shown in figure 5-9a. However as the voltage output on the first order filter has a satisfactory resolution by appropriately scaling the PWM-module settings, the steady state oscillation is undesirably high with a peak to peak voltage of about 100 mV.

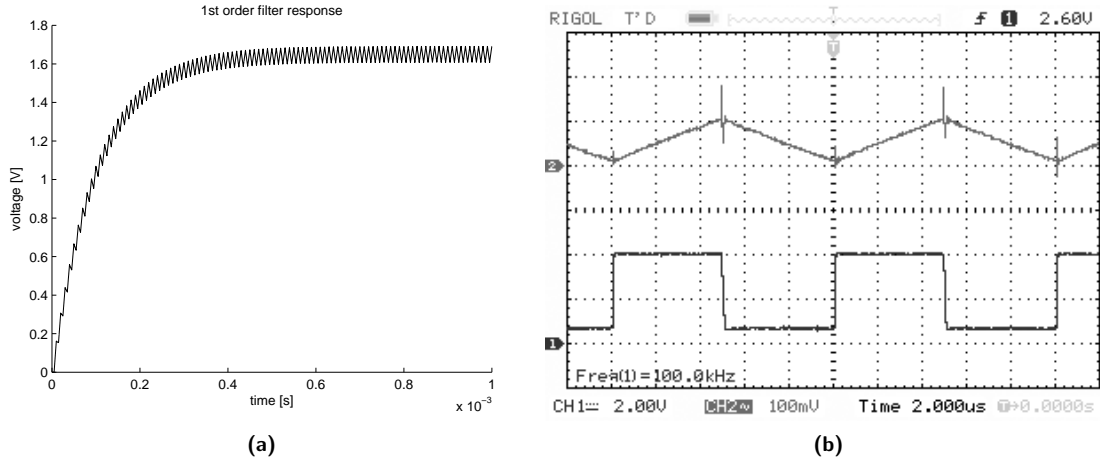


Figure 5-9: A first order filter step-response simulation (a) of the analog output voltage of a 100 kHz PWM-signal with a 50 percent duty-cycle showing a significant voltage oscillation. Measurements (b) on the PWM-signal (channel 1) and ac-coupled output voltage (channel 2) show close agreement to the simulation.

In order to reduce the output voltage oscillation without substantially changing the dynamic response, two first order low-pass filters are cascaded in series as shown in figure 5-8b. The second order filter is now based on two first order filter pairs as indicated by R18, C3 and R19, C4. If the component values C3, C4 and R18, R19 are chosen identical the transfer function from the output voltage V_{C4} to the input voltage V_{RD0} is defined by,

$$H_{LP2}(s) = \frac{V_{C4}(s)}{V_{RD0}(s)} = \frac{1}{s^2 R^2 C^2 + s 2RC + R^2 C^2} \quad (5-4)$$

Simulation on the 100 kHz PWM-frequency signal shown in figure 5-10a shows a dramatic decreased voltage oscillation due to the steeper frequency roll-off characteristic of a typical second order filter. Measurements shown in figure 5-10b show a highly improved oscillation attenuation which correspond closely to the simulation as shown in figure 5-10a.

Behind capacitor C4 the analog voltage is buffered by a LT1006 precision op-amp providing a low impedance voltage output. Resistor R20 and resistor combination R21,R22 are configured in a non-inverting op-amp configuration to scale the 3.3 V microcontroller output to a more industrial standard 5 V output to drive the actuator amplifiers. The IO-board provides two analog outputs at interface-terminal R and S in order to control the steering- and handlebar actuator individually.

²Measurements conducted with a Rigol DS1022C Digital Storage Oscilloscope.

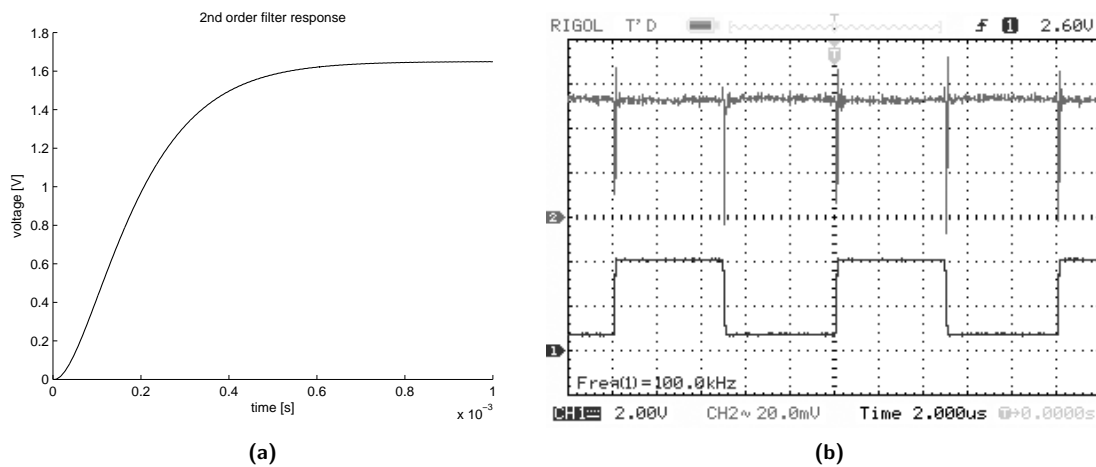


Figure 5-10: A second order filter step-response simulation (a) of the analog output voltage of a 100 kHz PWM-signal with a 50 percent duty-cycle showing a significantly reduced voltage oscillation with respect to the first order filter. Measurements (b) on the PWM-signal (channel 1) and ac-coupled output voltage (channel 2) again show close agreement to the simulation.

Controller Integration

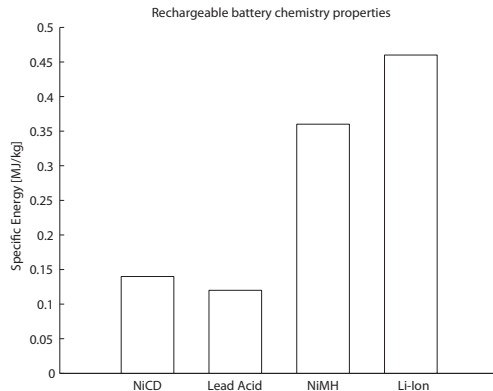
The IO-board is physically connected by two 60-pin flat band cable-connections to the Explorer16 MCU-development board and placed in a transparent casing at the back of the bicycle. The transparent casing still provides visibility of the status-LED and easy access to the interface terminals labeled A to T. The push-buttons are color-coded and placed on top of the controller.

5-2-3 Power source selection

An electrical power source provided by chemical energy storage by means of rechargeable batteries are most suitable to provide a DC voltage on a mobile platform. A big variety of battery chemistries like nickel-cadmium (NiCD), Lead-Acid, nickel-metal hydride (NiMH) and Lithium-ion are available with each it specific strengths and weaknesses.

On a bicycle where weight and size is critical, it is beneficial to use a chemistry which provides the highest specific energy. Or more specific, the highest amount of energy per unit mass. Figure 5-11a shows the specific energy densities for available battery chemistries. NiMH and Li-Ion chemistries are preferable over NiCD or Lead-Acid based batteries as they provide substantially more energy per unit mass. It shows from table 5-2 that the self discharge of a NiMH battery compared to Li-ion is highly unfavorable. This leads us to the conclusion that Li-Ion based batteries are recommended over other rechargeable batteries despite the higher purchase price.

A pair of Super-B 6400E batteries are used on the steer-by-wire bicycle. A Super-B 6400E battery has a nominal output voltage of 13.2 V combined with a capacity of 6.4 Ah in a 114 mm x 81 mm x 62 mm package at 0.9 kg. According to actuator voltage- and current requirements, the batteries can be connected in series or in parallel to gain the specified voltage or current requirement. Voltage and current requirements will be covered in the actuator selection section.



(a)



(b)

Figure 5-11: Specific energy density for different rechargeable battery chemistries (a) and a Super-B 6400 mAh Li-Ion rechargeable battery (b) to be used on the steer-by-wire bicycle.

Criteria	NiCD	Lead-Acid	NiMH	Li-Ion
Purchase price	low	average	low	high
Energy density	average	average	average	high
Self discharge	average	average	high	low

Table 5-2: A comparison between different rechargeable battery chemistries regarding relevant selection criteria in a steer-by-wire bicycle application.

5-3 Electromechanics

5-3-1 Sensor selection

To apply different steer-by-wire control strategies, the states of the bicycle have to be available to the controller. As previously mentioned the forward speed of the bicycle, handlebar- and steer angle as well as handlebar- and steer angular rate has to be measured in order to apply the Lateral Stabilization and Pole Placement control algorithms described earlier.

Forward speed measurement

As the dynamic behavior of the bicycle is a function of the forward speed, accurate measurement of the forward speed is necessary. In order to accurately measure the forward speed of the bicycle it is beneficial to use a type of sensor which has a direct coupling between the mechanical and electronic domain.

A spring loaded generator against the rear wheel of the bicycle provides a linear relation between rotational speed of the wheel and DC output voltage of the sensor. An electric DC motor operated as a generator is used as the rotational speed is linearly proportional to the output voltage. An 58 mm rubber o-ring equipped aluminium disc is mounted on a Maxon DC-motor which is spring-loaded against the rear wheel of the bicycle, see figure 5-12a and Appendix B-1 for detailed information. As the rear wheel will rotate as the bicycle moves

forward, the aluminium disc rotates, generating a voltage proportional to the forward speed of the bicycle. The output voltage of the forward speed sensor U_v is proportional to the nominal motor voltage U_n , nominal rotational speed n_n , and geometrical properties defined by the o-ring radius r_o , wheel radius r_w , the distance from the wheel center to the o-ring contact point on the tire r_s and the forward speed v of the bicycle as shown in figure 5-12b. This leads to the following relation for the output voltage U_v as function of forward speed of the bicycle v ,

$$U_v(v) = 30 \frac{U_n v r_s^2}{\pi n_n r_o r_w^2} \quad (5-5)$$

At a maximum forward speed v of 10 m/s the output voltage of the forward speed sensor U_v defined by the properties given in table 5-3 is about 10.42 V. However any voltage higher than 3.3 V will damage the ADC-module of the microcontroller, therefore the forward speed sensor signal has to be attenuated suitably in order to protect the ADC-input from over voltage and maximize measurement resolution.

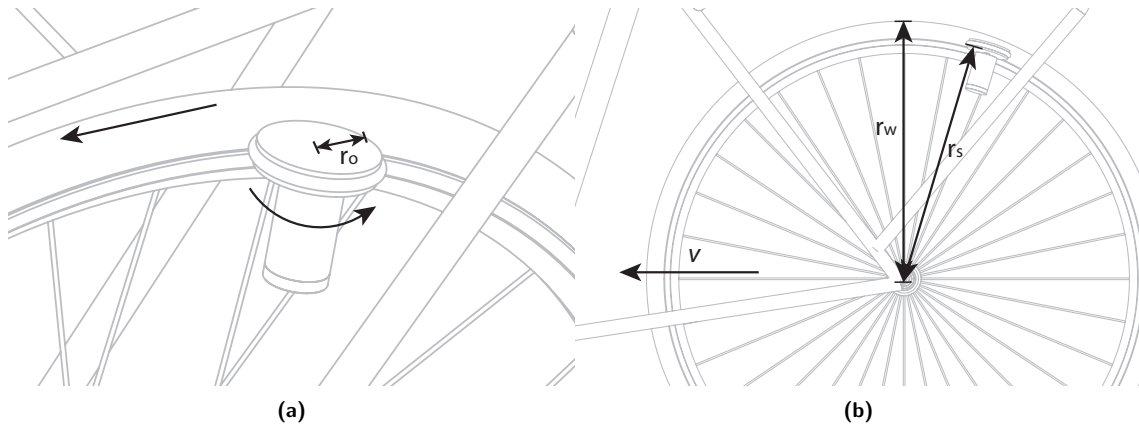


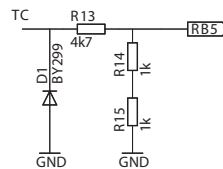
Figure 5-12: A schematic overview (a) of the forward speed sensor positioning against the rear wheel of the bicycle. The output voltage of the forward speed sensor is a function of the geometrical properties (b) and dc-motor characteristic.

Parameter	Value	Dimension
U_n	18	V
n_n	5300	rpm
r_o	0.029	m
r_w	0.347	m
r_s	0.335	m

Table 5-3: Parameters defining the forward speed sensor output characteristics.

Figure 5-13a show the input-protection circuitry placed on the IO-board to interface the forward speed sensor to the microcontroller. In a forward moving bicycle, the positive signal-wire of the forward speed sensor is connected to interface terminal C (TC). The input is protected against reverse-voltage in case the bicycle is moved backwards by a BY299 diode. The diode is reverse-biased against the positive signal-wire to provide a minimum voltage

drop over the diode of about -0.2 V which is within the safe limits of the microcontroller ADC-module. A resistor divider provided by R13 and the R14, R15 pair attenuates the maximum forward speed sensor output with by about 0.298, to a maximum voltage at the ADC-module of about 3.11 V . This ensures a safe operating range while still maintaining a maximum measurement resolution utilized by the 12-bit ADC-module.



(a)

Figure 5-13: The input circuitry on the IO-board to interface the forward speed sensor at interface-terminal C (a) providing reverse-voltage protection by a reverse-biased diode D1, and a voltage divider stage provided by resistors R13 and R14, R15 at the microcontroller input RB5.

Steering- and handlebar position measurement

The measurement of the rotational position of the steering- and handlebar assembly, is performed by two Altheris FCP22AC potentiometers which are connected to the front fork steering stem and handlebar axle respectively. The conductive-plastic, endless-turn, 320 degree travel, $5\text{ k}\Omega$, linear potentiometers are connected by a timing-belt construction to the steering stem and handlebar axle as shown in figure 5-14b and 5-14a. A small 36-teeth gearwheel mounted on the potentiometer is driven by a larger 72-teeth gearwheel, providing a full-scale rotation at the steering assembly and handlebar of ± 80 degrees.

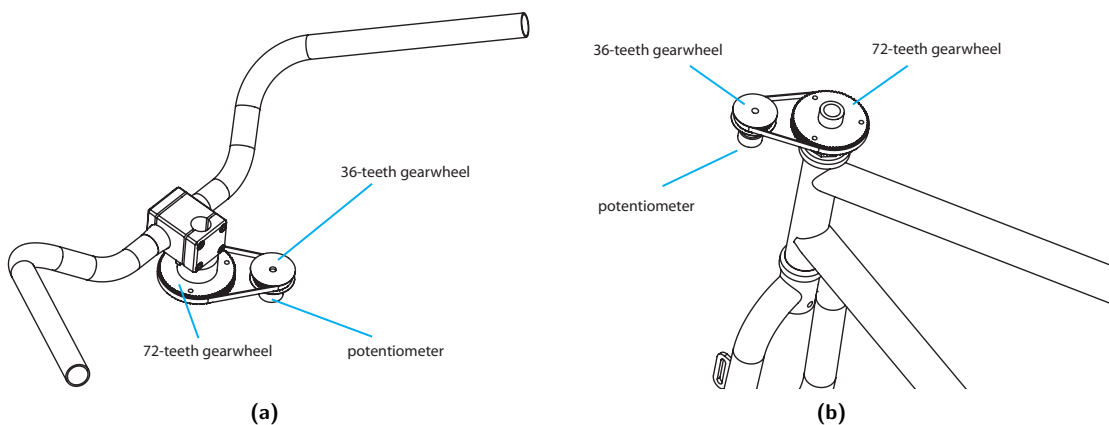


Figure 5-14: The decoupled handlebar assembly (a) and steering assembly (b) on the bicycle showing the potentiometer driven by a timing belt construction.

The potentiometers acting as a voltage divider where the wiper-connection is connected to the microcontroller ADC-module while the remaining two connections are referenced to ground

and 3.3 V respectively. The position measurement resolution is a function of the full-scale potentiometer measurement range α_f and gear-ratio defined by the teeth-count of the small gearwheel z_1 and large gearwheel z_2 . Provided the 12-bit ADC-module sampling resolution gives the following relation for the position measurement resolution res_{pos} ,

$$res_{pos} = \frac{\alpha_f \left(\frac{z_1}{z_2} \right)}{2^{12}} \quad (5-6)$$

This leads to a position measurement resolution of about 0.04 degrees. However noise induced by the sensor and quantization noise originating from the microcontroller ADC cause a smaller effective positional resolution as shown in figure 5-15. A random fluctuation of the ADC-module output samples are shown with an amplitude of about four least significant bits (LSB). The signal to noise level is still highly sufficient to provide accurate information to the controller algorithms on the steering position.

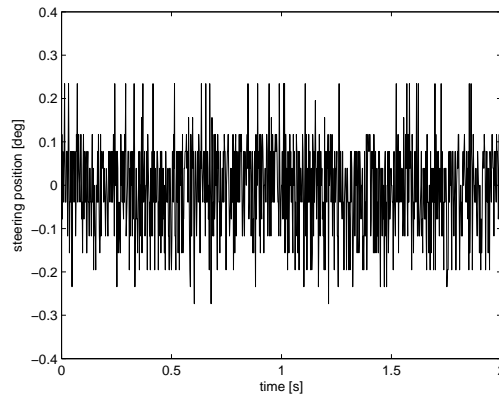


Figure 5-15: Quantization and sensor noise level on the steering position signal which indicates the effective angular resolution on the steering- and handlebar position measurement.

Steering- and handlebar rate measurement

The measurement of the angular rate of the steering- and handlebar assembly can be done directly or indirectly. A direct angular rate measurement can be done with the use of a dedicated angular rate sensor or indirectly by numerical differentiation of the potentiometer position signal. The use of a dedicated angular rate sensor provides a better signal to noise ratio, but integration on the steer-by-wire bicycle requires additional ADC input channels and physically more components.

However by numerically differentiating the signal from the steering- and handlebar position sensor, the angular rate can also be determined. The accuracy of the calculated angular rate is influenced by the sampling frequency and the noise-level of the position signal. The angular rate $y(t_n)$ is calculated by defining the difference between the input signal $u(t_n)$ at the current time step T_s and the previous input signal $u(t_{n-1})$ by the following relation,

$$y(t_n) = \frac{u_{t_n} - u_{t_{n-1}}}{T_s} \quad (5-7)$$

The input signal difference is subsequently multiplied with the inverse of the time step T_s as shown in figure 5-16a. A Silicon Sensing CRS03 dedicated angular rate sensor shows a reference signal compared with the numerically differentiated angular position signal. The noise level of the calculated angular rate signal is significant compared to the reference signal provided by the dedicated angular rate sensor.

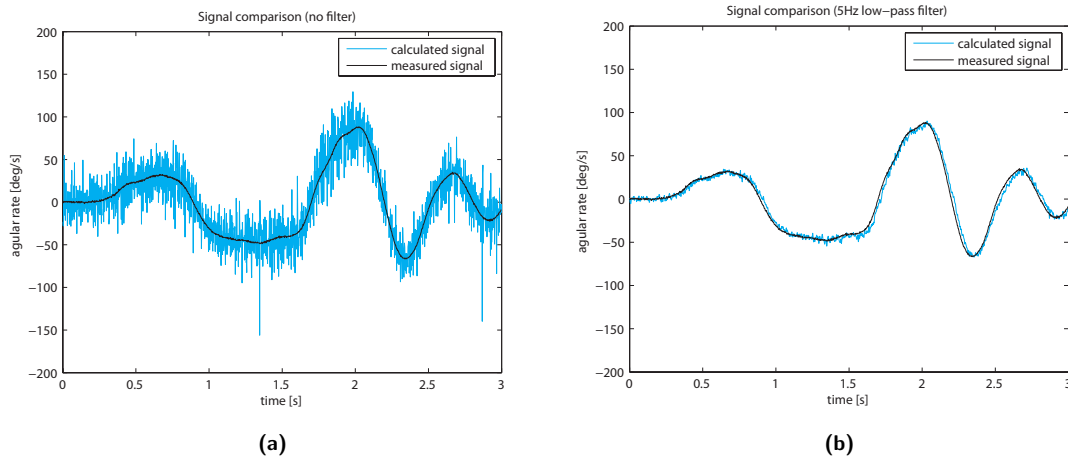


Figure 5-16: The calculated angular rate signal (a) by numerical differentiation of the position signal shows a significant amount of noise compared to the signal from a dedicated angular rate sensor. However when using a suitable 5 Hz low-pass filter (b) the calculated angular rate signal corresponds closely to the actual angular rate as shown by the dedicated angular rate sensor.

However if a suitable low-pass filter is utilized, the noise originating from the angular position sensor can be filtered to produce a more useable output signal. From [Kooijman et al., 2009] we know that, the steering amplitude frequency spectrum during normal bicycle driving only shows significant contributions in the lower frequency range, up to 3 Hz. This relatively low frequency steering excitation allows for the use of a 5 Hz low-pass filter which provides a suitable attenuation of higher frequency content. Figure 5-16b shows the numerically differentiated angular position signal with the addition of a 5 Hz low-pass filter which significantly improves the signal to noise ratio. A suitably chosen cut-off frequency attenuates the high frequency noise present on the angular-position sensor signal but however, introduces an additional and highly undesirable phase-lag. Figure 5-16b shows clearly the different bandwidth characteristics of both signals characterized by a 5 Hz numerically differentiated position signal and a clean, even more noise-free signal from a dedicated angular-rate sensor which has a specified 10 Hz bandwidth. Any additional phase-lag introduced by sensors in a feedback system can decrease its performance and even destabilize the system. More in-dept modeling and experimental testing will be shown to decide if the faster angular-rate sensor can be omitted in favor of the slower numerically differentiated angular position signal.

Roll-angle and -rate measurement

The roll-angle and roll-rate of the bicycle are the remaining states to be utilized by the controller algorithms. However without a fixed reference frame, measurement of a bicycle roll-angle and roll-rate is not as straight-forward as compared to the steering- and handlebar angle

measurement as previously shown. In different fields of application, roll-angle measurement is of great interest judging numerous publications in avionic-, transportation- and robotics-research. Most recent publications on roll-angle measurement of single-track-vehicles are by [Boniolo et al., 2008a] which utilizes a dual optical distance-sensor layout to determine the roll-angle with respect to the road surface. A subsequent study [Boniolo et al., 2008b] which fuses high- and low-frequency content to provide an accurate roll-angle estimation.

For the steer-by-wire bicycle prototype a similar approach is proposed by utilizing a complementary filter algorithm based on sensor information provided by an Analog Devices ADXL335 three-axis accelerometer and an InvenSense IDG500 dual-axis angular-rate gyro. As shown in figure 5-17a, both MEMS-based sensors are conveniently pre-mounted on a Sparkfun IMU5 sensor board equipped with onboard voltage regulators and filters for easy interfacing to the steer-by-wire bicycle controller board.

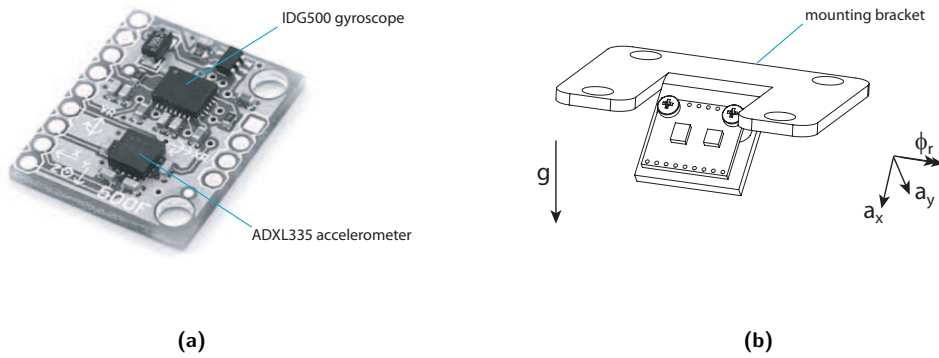


Figure 5-17: A small sensor-board (a) incorporating a ADXL335 three-axis accelerometer and a IDG500 two-axis angular rate gyro, is utilized to calculate the roll-angle of the bicycle. The sensor-board is placed on a mounting bracket (b) such that the accelerometer provides a static angle-estimation in addition to the dynamic angle-estimation of the angular rate-sensor by numerical integration.

In order to estimate the bicycle roll-angle, two-axis sensor information by the accelerometer is combined with sensor information from a single-axis provided by the angular-rate sensor. Figure 5-17b show the orthogonal orientation of the two accelerometer axes a_x and a_y subjected to the earths gravitational field \mathbf{g} , which yields an accurate estimation of the static roll-angle ϕ between the sensor-plane and earths gravitational field by the following relation,

$$\phi = \arctan\left(\frac{a_x}{a_y}\right) \quad (5-8)$$

However, the output of the accelerometer contains a relative high amount of high-frequency noise and high frequency signal content introduced by road irregularities which is highly undesirable. A suitable low-pass filter can be used to attenuate the high-frequency noise-content allowing for a more accurate low frequency angle estimation. The loss of the dynamic high-frequency content however is complemented by numerical integration of the angular-rate signal-output ϕ_r from the angular-rate gyro by the following relation,

$$\phi(t) = \int_{t_0}^t \phi_r dt + \phi_r(t_0) \quad (5-9)$$

Low-frequency- and temperature dependant zero-output drift is attenuated using an appropriately chosen high-pass filter with a cut-off frequency identical to the accelerometer low-pass filter. Figure 5-18a shows a block diagram of the complementary filter algorithm, combining the noise-free filtered, low-frequency information of the accelerometer combined with the drift-free filtered, high-frequency numerically integrated signal from the angular-rate sensor.

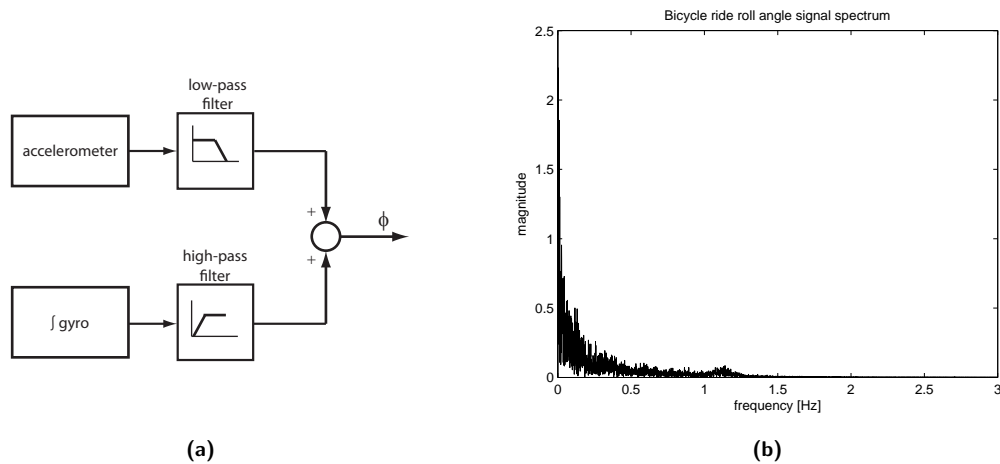


Figure 5-18: A block diagram of the complementary filter algorithm (a) which utilizes the noise-free filtered, low-frequency information of the accelerometer combined with the drift-free filtered, high-frequency numerically integrated signal from the angular-rate gyro. The roll-angle frequency spectrum signal (b) of typical bicycle ride shows the relative low frequency content. No distinguishable frequency content is present from 1.5 Hz and above.

The key to accurate estimation of the roll-angle is based on appropriate selection of the cut-off frequency of both the high- and low-pass filter. The cut-off frequency of the accelerometer low-pass filter should pass the low-frequency signal content experienced during normal bicycle driving and attenuate any higher frequency disturbances.

In a recent M.Sc. study [van den Ouden, 2011] an identical Batavus Browser bicycle was equipped with measurement devices to characterize bicycle behavior during city driving. A bicycle ride on a predefined route in the center of Delft by a group of pre-selected test drivers provided a data-set including the time history of the roll-angle of the bicycle recorded by a relative expensive, commercially available IMU-sensor. A spectral analysis of a typical roll-angle data-set is shown in figure 5-18b and shows the relative low-frequency nature of the bicycle roll-angle signal. A suitable cut-off frequency for the first-order low- and high-pass filters is determined to be 2 Hz as there is no higher distinguishable frequency content in the roll-angle signal.

A bench test was performed for the individual sensors and the complementary filter algorithm by mounting the sensor-bracket on a potentiometer to provide an absolute reference angle as well as an additional Silicon Sensing CRS03 angular-rate gyro to provide a reference output to the IDG500 angular-rate gyro. Figure 5-19a shows the static angle calculation by the accelerometer compared to the reference angle provided by the potentiometer in the bench test-setup. Some high-frequency signal content is visible in the accelerometer signal, however the accelerometer provides an accurate estimation compared to the potentiometer reference angle.

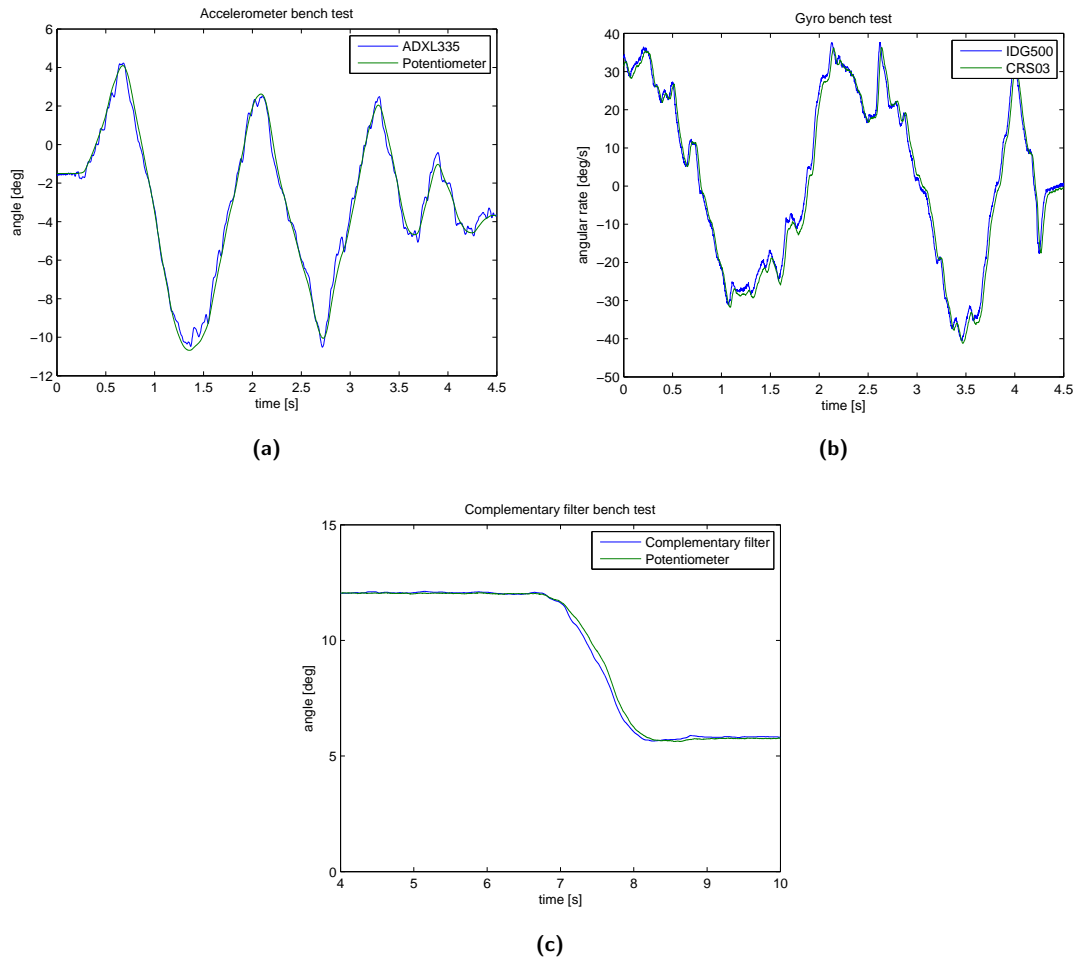


Figure 5-19: The static roll-angle estimation (a) from the accelerometer compared to the potentiometer reference angle on the bench test-setup shows close agreement. The output of the IDG500 angular-rate gyro (b) was experimentally determined to a CRS03 angular-rate sensor which provided an accurate output sensitivity reference. Phase difference originates from different bandwidth characteristics. The complementary filter algorithm (c) combining accelerometer and gyro sensor information compared to the potentiometer reference angle shows a realistic roll-angle estimation in primarily static measurements.

The sensitivity specified in the datasheet of the IDG500 angular-rate gyro of $9.1 \text{ mV}/^\circ/\text{s}$ appeared to be incorrect. Initial testing with the sensitivity as specified in the datasheet showed inconsistent readings if the numerically integrated signal was compared to the potentiometer reference angle. Therefore the output sensitivity was experimentally determined with the use of a CRS03 angular-rate gyro temporarily mounted on the sensor-bracket. Three different CRS03 angular-rate gyro's have been tested which individually showed identical output sensitivities corresponding to the manufacturer specifications. Therefore, one of the CRS03 angular rate gyro's was utilized as a reference to determine the output sensitivity of the IDG500 sensor, which appeared to be $3.6 \text{ mV}/^\circ/\text{s}$. Figure 5-19b shows the output of both angular-rate gyro's to an identical external excitation. The phase difference between both sensor outputs is due to the different bandwidth characteristics between both angular-rate gyro's. The IDG500 has a faster response time due to the higher bandwidth which is specified at 500 Hz in comparison to the relatively low 10 Hz bandwidth of the CRS03 rate gyro.

Combining the accelerometer- and gyro sensor data with the use of the complementary filter as shown in figure 5-18a utilizing a 2 Hz bandwidth, first-order low- and high-pass filter respectively, shows a roll-angle estimate as shown in figure 5-19c. Static angle estimation corresponds closely, however a small angular error is present during the dynamic transition between two static positions. This small angular estimation error is probably caused by the low-frequency centripetal acceleration experienced by the individual accelerometer axes causing a bias during a position transition. This low frequency bias due to a centripetal acceleration is however also present when the bicycle rides along a curve.

A more advanced sensor estimation algorithm should therefore be implemented like a recursive estimation technique as provided in a Kalman filter algorithm. However as a Kalman filter algorithm provides a more reliable angle estimation, it is more processor intensive and requires an accurate dynamic model. A relatively easy improvement by using the complementary filter algorithm is to utilize a low frequency angle estimation signal resistant to centripetal acceleration disturbances. An improvement on the bicycle roll angle estimation is to replace the low frequency accelerometer signal with a direct angle measurement. A dual optical distance measurement as described in [Boniolo et al., 2008a] could provide a suitable direct low frequency angular signal reference as illustrated in figure 5-20a.

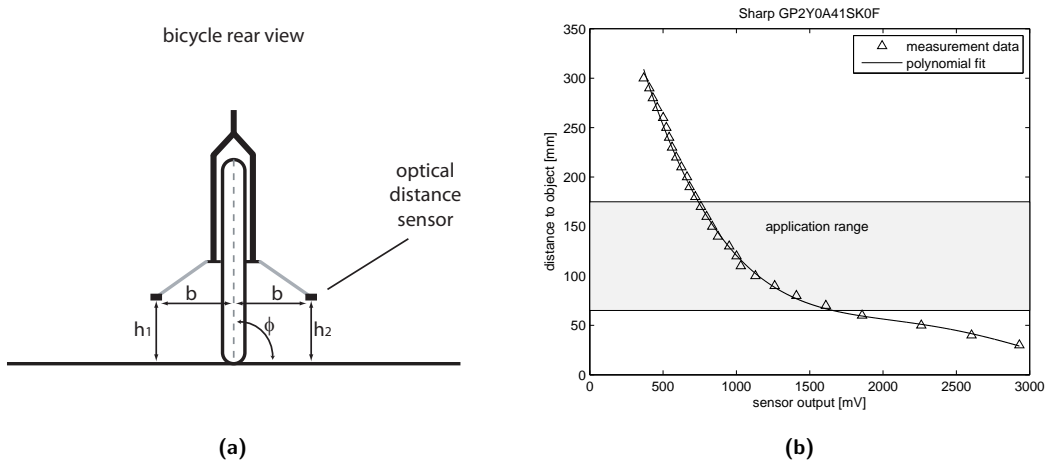


Figure 5-20: A dual distance sensor setup can be used to provide a low frequency roll angle estimation (a) on the steer-by-wire bicycle prototype. The output of the Sharp optical distance sensors provide a non-linear relation between the distance measurement and output voltage (b). However a suitable curve-fitting procedure on the sensor calibration data provides a suitable expression for numerical roll angle calculation.

Two low-cost, low-range, Sharp GP2Y0A41SK0F, infrared optical distance sensors are placed on either side of the bicycle near the rear-axle, measuring the distance to the ground surface. Equally spaced from the center of the bicycle and placed from a certain distance to the ground surface. The roll angle ϕ of the bicycle is calculated using the following expression as a function of the horizontal spacing b and the distance to the ground surface of each individual sensor defined by h_1 and h_2 ,

$$\phi = \arctan\left(\frac{h_1 - h_2}{2b}\right) \quad (5-10)$$

A positive change in roll angle of the bicycle will cause distance h_1 to increase and h_2 to

decrease and vice versa. The Sharp optical distance sensors operate in a range from 4 cm to 30 cm which provides the design constraints with respect to the physical placement on the bicycle. A large distance change is beneficial to improve the angular resolution, however this implies a physically wide spacing which is undesirable on a relatively compact bicycle. The output calibration data from the Sharp position sensor is shown in figure 5-20b which shows the non-linear relation between the distance measurement and the output voltage. The sensor sensitivity increases with decreasing object distance. It is therefore beneficial to use the sensors in the lower distance range to improve sensitivity. Placing the sensors at a distance of $b=120$ mm and $h_1=h_2=120$ mm on the bicycle provides a physically compact design, while operating the distance sensors inside its sensitive operating range allowing for accurate roll angle measurements up to ± 25 degrees.

An initial rough estimate for the low frequency roll angle estimation using equation 5-10 should provide an angular resolution of about ± 0.5 degrees from an upright position. This should provide an accurate low frequency angle estimate to be utilized in the complementary filter setup as described previously. The roll angle estimation accuracy is obviously only guaranteed when driving at a smooth and flat level ground surface. However for testing purposes in a controlled environment the proposed roll angle measurement should provide a useable roll angle estimate to be integrated in the previously described controller algorithms.

5-3-2 Actuator selection

The actuators to be used to drive the steering wheel and the handlebar should meet certain design criteria. Mechanical and electrical design constraints are summarized by the need for sufficient output torque and output power, the capability to provide the required rotational speed and the ability to operate at the available power source in terms of operating voltage. The rotational inertia of the steering assembly should not increase significantly compared to the original front fork assembly, as the uncontrolled steering response of the bicycle should not be obstructed due to additional steering components.

To provide easy interfacing with the controller hardware, the use of electric motors to actuate the steering- and handlebar assembly is an obvious choice. In general three main types of electric motor topologies can be distinguished, stepper motors, alternating current (AC) motors and direct current (DC) motors. The most relevant property for integration in a servo controlled application is the linear relation between the input and output defined by the input current and output torque respectively. Only electric DC motors provide a linear relation between input current and mechanical output torque.

Torque and power requirements

The electric motors should be able to provide sufficient torque and power to drive the steering- and handlebar assembly. In chapter 4 a steer torque perturbation of 2 Nm shows a realistic response in terms of roll- and steering angles. A data-set provided by [van den Ouden, 2011] also contains the steer torque history during a typical bicycle ride. A time history plot of the steer torque during a specific recording is shown in figure 5-21a.

The steer torque distribution figure 5-21b shows that the absolute torque provided by the rider on the steering assembly rapidly decreases from 2 Nm and up. Still, a maximum steer torque of

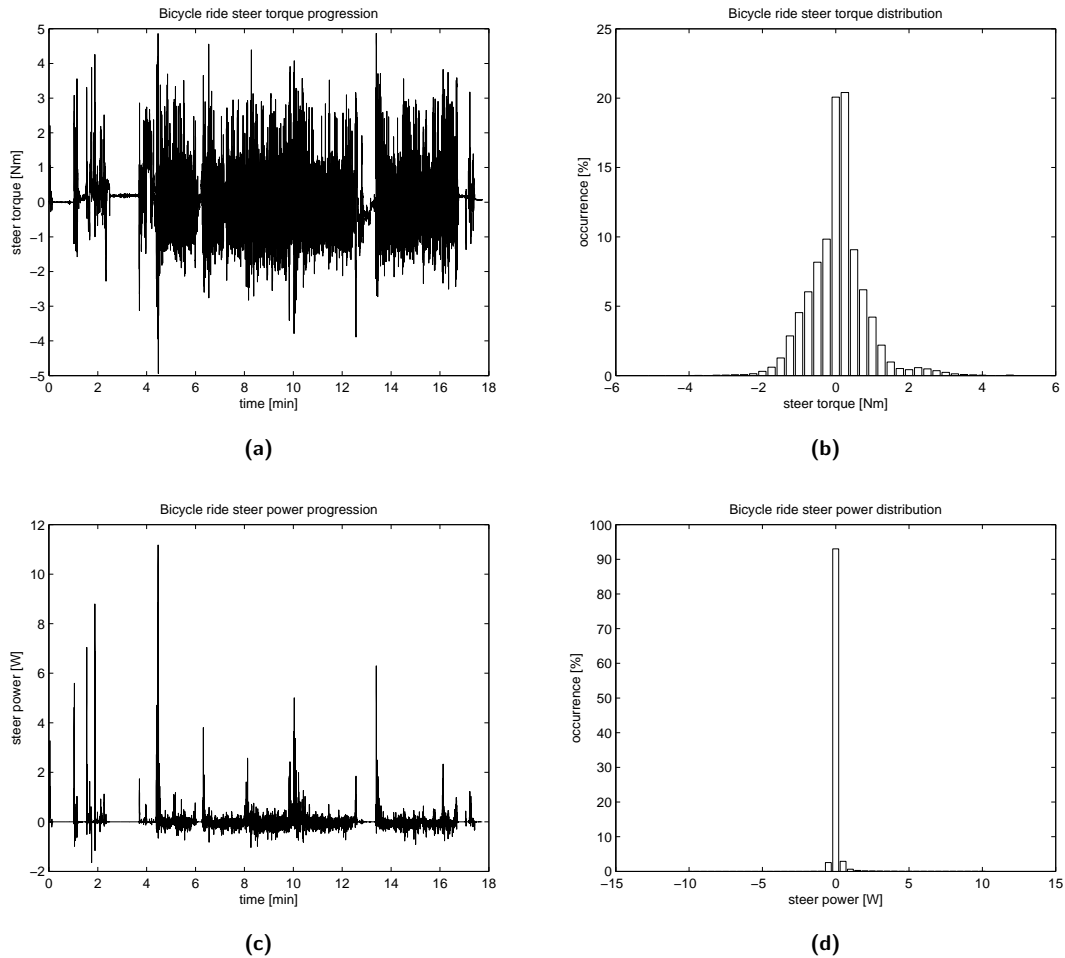


Figure 5-21: The steer torque measured (a) during a city ride on the Batavus Browser bicycle shows a maximum steer torque of about 5 Nm, however the absolute steer torque distribution (b) shows a significant decrease from 2 Nm and up. The steer power provided by the rider on the handlebars (c) shows a few significant peaks up to 12 W however as the distribution shows (d) the significance of these peaks is negligible as the majority of the time the steer power is below 1 W.

about 6 Nm as proposed in [van den Ouden, 2011] should be regarded as a design constraint for the steer-by-wire bicycle actuator specifications. A static steer torque specification is not the only design constraint as the actuator power should be considered as well. The actuator power should be adequate to provide the required rotational speed of the steering- and handlebar assembly. Figure 5-21c shows the corresponding power applied to the steering assembly. A few significant peaks up to 12 W show the need for an output power requirement which is an order of magnitude higher than most of the time required as shown by the steer power distribution figure 5-21d.

In order to satisfy the design constraints in terms of output torque and -power, a Maxon permanent magnet, 12 pole, 3 phase, brushless DC motor is selected. The Maxon EC90 type of electric motor provides up to 90 W of output power at a maximum voltage of 48 V. The nominal output torque T_n of 0.49 Nm is available at a specified nominal current I_n of 2.12 A. The brushless DC motor is controlled by a Maxon EPOS2 switching motor-amplifier

driving the motor with a sinusoidal commutation profile, providing a high power efficiency and smooth torque output. The motor-amplifier is configured as a current amplifier which ensures a constant current to the motor windings, regardless of the actual rotational speed of the motor. The use of this electric motor and motor-amplifier combination allows for an easy torque control, linearly proportional to the control voltage output by the DAC-circuitry of the controller.

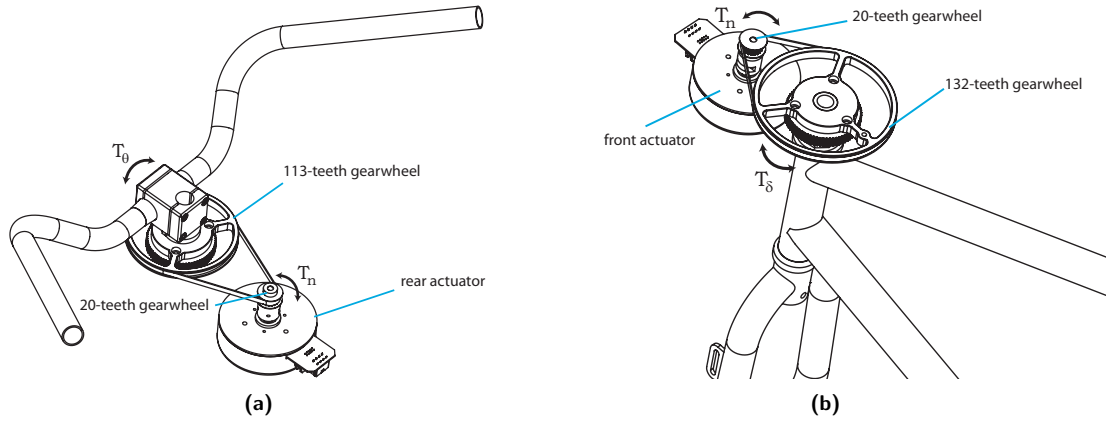


Figure 5-22: The decoupled handlebar assembly (a) and steering assembly (b) on the bicycle showing the actuator positioning driven by a timing belt construction.

In order to be able to satisfy the torque requirement described previously, the nominal output torque of the motor can be increased with the addition of a gearing assembly. In order to reduce friction and play in the steering assembly, the use of a precision timing-belt construction is favorable above a (planetary-) gearbox construction. A gearwheel on the motor output combined with a gearwheel on the steering assembly or handlebar, increases the steer torque with a ratio defined by the radii and subsequently the number of teeth on the gearwheels. However the effective rotational inertia of the steering assembly increases quadratically with the gear ratio which is undesirable.

In figure 5-22b it is shown that the steer torque T_δ is defined by the motor torque T_n multiplied with the torque multiplication factor introduced by the gearing assembly. The torque multiplication factor defined by the teeth-count of the small gearwheel z_{fs} and the large gearwheel z_{fl} gives the following relation for the steer torque,

$$T_\delta = T_n \frac{z_{fl}}{z_{fs}} \quad (5-11)$$

From the nominal motor torque T_n and the teeth-count ratio of the gearing assembly, the steer torque yields $T_\delta = 3.2 \text{ Nm}$. This approach also applies for the handlebar torque T_θ which is defined by the motor torque T_n multiplied with the torque multiplication factor. Again the torque multiplication factor at the handlebar assembly is defined by the teeth-count of the small gearwheel z_{rs} and the large gearwheel z_{rl} which in particular is a little smaller in comparison to the gearwheel on the steering assembly due to space limitations. The relation for the handlebar torque is now given by,

$$T_\theta = T_n \frac{z_{rl}}{z_{rs}} \quad (5-12)$$

The handlebar torque now yields $T_\theta = 2.8 \text{ Nm}$. Both the nominal steering- and handlebar torque now are about 3 Nm which should in general be sufficient during a normal bicycle ride.

Thermal limitations

A higher required peak torque output is occasionally required based on the measurements on the instrumented bicycle. The maximum output torque of the motor can actually be higher as long as the thermal dissipation is high enough and the temperature of the motor windings do not exceed 125 °C. Relevant electrical, mechanical and thermal information is shown in table 5-4.

The output torque T of the motor is defined by the following relation,

$$T = iK_t \quad (5-13)$$

Where i is the current through the windings and K_t is the torque constant. The motor behavior is defined by mechanical and electrical properties. The mechanical properties are related to the rotor inertia J_r and motor acceleration $\ddot{\theta}_r$ as defined in,

$$J\ddot{\theta}_r = iK_t \quad (5-14)$$

The contribution of the damping term due to coulomb friction is neglected as no specified value is given by the manufacturer and rotational speeds are low. Electrical properties are related to the winding inductance L_w , the winding resistance R_w , the supply voltage U , the speed constant K_n and the rotational speed $\dot{\theta}_r$ of the motor as in,

$$L \frac{di}{dt} + iR_w = U - K_n \dot{\theta}_r \quad (5-15)$$

The contribution in the righthand term by the speed constant K_n and rotational speed $\dot{\theta}_r$ generates a voltage opposing the supply voltage U of the motor, lowering the effective current flow and subsequently reducing the motor torque with increasing rotational speed. When the opposing voltage is equal to the supply voltage the motor is running at its nominal rotational speed n_n . However as the motor-amplifier is configured as a current controller, the current flow is controlled by an internal control-loop in the motor-amplifier compensating for the reduced effective driving voltage therefore the speed constant K_n will be set to zero.

As the steering angle will only be about $\pm 45^\circ$ in a driving situation, the maximum rotation of the actuator is small and the motor will never be operated at the specified nominal rotational speed. The motor is continuously actuated about a center reference from a standstill position, which implies that the required operating voltage U is exclusively defined by the winding current i and winding resistance R_w ,

$$U = iR_w \quad (5-16)$$

Parameter	Description	Value	Dimension
U_n	Nominal voltage	48	V
n_n	Nominal speed	1640	rpm
T_n	Nominal torque	0.494	Nm
i_n	Nominal current	2.12	A
R_w	Winding resistance	2.3	Ω
L_w	Winding inductance	2.5×10^{-3}	H
K_t	Torque constant	0.217	Nm/A
K_n	Speed constant	$30/(44\pi)$	Vs/rad
$R_t h$	Thermal resistance	4.88	K/W
τ_w	Thermal time constant winding	52.6	s
J_r	Rotor inertia	3×10^{-4}	kgm ²

Table 5-4: Maxon EC90 brushless DC motor mechanical, electrical and thermal properties.

For example, if the motor is actuated at the nominal current specification the required operating voltage U is only 4.9 V. However as previously indicated, as the motor winding temperature is below 125 °C the operating current can be higher as long as the maximum winding temperature is not exceeded. The temperature increase in the motor is primarily caused by the joule heating effect which is a function of the winding resistance and winding current. The actuators are powered from two Super-B 12 V batteries connected in series resulting in a maximum current delivery of 10.4 A, which is a five times multiplication with respect to the nominal winding current. This additional current capability increases the maximum torque output of the motors to about 2.3 Nm as shown in equation 5-13 and 14.8 Nm at the steering wheel.

As the output torque increase of the motor is highly favorable, the increased temperature due to the additional current flow is not. The power dissipation P_j due to the joule heating effect is given by,

$$P_j = i^2 R_w \quad (5-17)$$

The power dissipation at a maximum current of 10.4 A is about 250 W, well over the maximum specified power of 90 W for this type of actuator. As long as the maximum power or torque request is limited to a small period of time, the maximum winding temperature will not be exceeded. The motor-amplifier monitors the winding temperature of the motor indirectly by evaluating the current flow over time. Based on pre-specified motor parameters as shown in table 5-4, the internal winding temperature is calculated by the motor-amplifier and if needed, the output current reduced to the nominal output current allowing the motor to cool down. The maximum duration for the additional current flow is provided by the manufacturer and is shown in figure 5-23.

A maximum steering torque of 6 Nm for example would require a winding current of about 4.2 A which is exactly twice the nominal current. According to figure 5-23 this gives us a normalized peak current time of about 0.28, multiplied by the thermal time constant winding τ_w specification from table 5-4 gives a maximum torque delivery duration of about 14 seconds after which the motor-amplifier will reduce the current to the nominal specification.

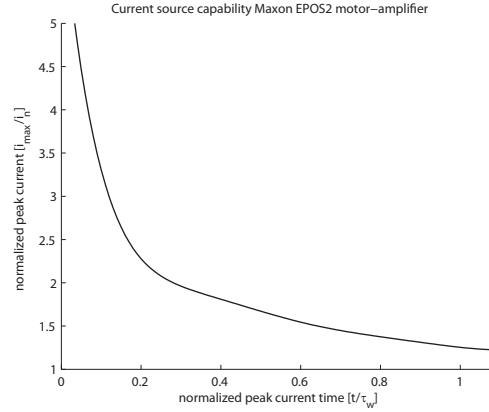


Figure 5-23: The maximum allowed additional current flow i_{max} normalized as a function of the nominal current i_n as a function of time.

Actuator bandwidth

The steer torque requirement during a bicycle ride is depending on the type of steer manoeuvre being conducted and subsequently the steer torque requirement. In order to make a realistic estimation of the required steering torque a simulation is performed on the steering response with realistic steering assembly inertia properties. To express the system in state space form, the state space representation is given by the state equation 5-18 and output equation 5-19:

$$\dot{x} = \mathbf{A}\mathbf{x}(t) + \mathbf{B}\mathbf{u}(t) \quad (5-18)$$

$$\mathbf{y} = \mathbf{C}\mathbf{x}(t) + \mathbf{D}\mathbf{u}(t) \quad (5-19)$$

Combining 5-14 and 5-15 gives the following expressions, where states are expressed as $x = [\delta_m, \dot{\delta}_m, i]^T$, the input variable u is the motor voltage U and the output y is the motor output angle δ_m . Now the state matrix \mathbf{A} , input matrix \mathbf{B} , output matrix \mathbf{C} and feed forward matrix \mathbf{D} are defined by the motor parameters as shown in table 5-4.

$$\mathbf{A} = \begin{bmatrix} 0 & 1 & 0 \\ 0 & 0 & \frac{K_t}{J_r + J_f \left(\frac{z_{fs}}{z_{fl}}\right)^2} \\ 0 & -\frac{K_m}{L_w} & -\frac{R_w}{L_w} \end{bmatrix}, \quad \mathbf{B} = \begin{bmatrix} 0 \\ 0 \\ \frac{1}{L_w} \end{bmatrix}. \quad (5-20)$$

$$\mathbf{C} = \begin{bmatrix} 1 & 0 & 0 \end{bmatrix}, \quad \mathbf{D} = \begin{bmatrix} 0 \end{bmatrix}. \quad (5-21)$$

The steering assembly rotational inertia J_f however is a parameter based on the physical interconnection of the rotational inertia of the front wheel, front fork, gear wheels and actuator. The effective rotational inertia of the steering assembly equals to $J_f = 0.101 \text{ kgm}^2$.

A time simulation on the state-space representation shown in 5-21 coupled to the feedback structure shown in figure 5-24 is performed to predict the torque requirement on the steering assembly, in order to track the reference steering motion with respect to a specific steering

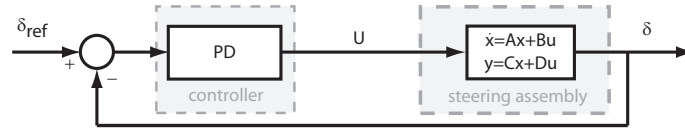


Figure 5-24: A simplified block diagram of the steer assembly position feedback loop which shows the relation between the steer- and reference-angle as a function of the PD-controller parameters.

frequency and -amplitude. A PD-controller is added in a feedback loop to shape the dynamic response by adding a scalable stiffness and damping term with respect to the steering position.

The controller utilizes an arbitrary proportional constant of 12 Nm/rad and a derivative constant of 0.6 Nms/rad. Three time-simulations shown in figure 5-25a, 5-25b and 5-25c show the steer response on a 10 degree sinusoidal handlebar-angle reference with increasing frequency from 0.5 Hz up to 1.5 Hz. The increasing frequency causes the required steer torque to increase, which at a frequency of 1.5 Hz has raised to about 2 Nm, well below the nominal steer torque specifications of the actuator.

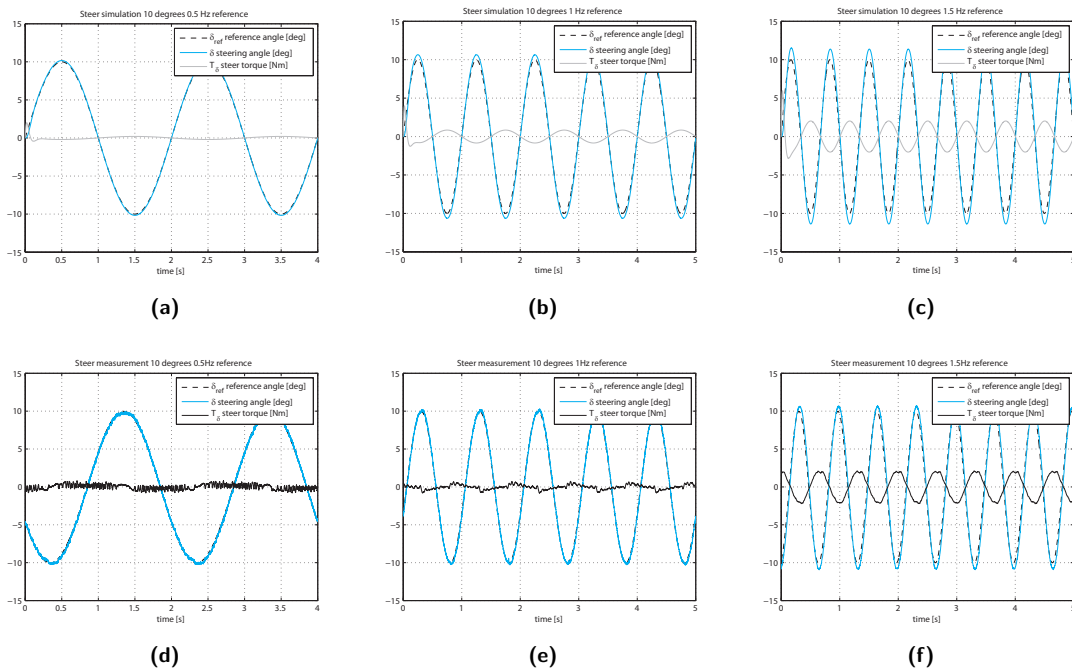


Figure 5-25: A simulation with a 10 degree sinusoidal handlebar reference profile at different steer frequencies (a,b,c) show the steer response and required actuator torque for a specific PD-controller stiffness. Measurements on the actual steer-by-wire bicycle (d,e,f) show close agreement with respect to the required actuator torque and steer response.

A validation step on the steer-by-wire bicycle by measuring the actual steer response on the 10

degree handlebar-angle reference was performed to evaluate the accuracy of the model. The bicycle is lifted from the ground eliminating un-modeled friction forces between the ground- and tire surface. Figure 5-25d, 5-25e and 5-25f show the actual steer-angle on the steer-by-wire bicycle as well as the steer torque requested by the controller.

The simulation shows a reasonable accurate prediction on the maximum error between the handlebar reference- and steer angle as well as the phase-lag which becomes apparent at higher steer frequencies. At low steer frequencies the steer torque and steer motion profile shows a significant noise component which is caused by the cogging-forces present in the actuator. However as the rotational speed increases with increasing steer frequency, the magnitude of the cogging forces with respect to the actual steer torque becomes negligible which is shown by the higher frequency measurement plots, in which a more continuous and more smooth position profile is observed.

The actual tracking performance of the steering assembly to the handlebar input, with respect to the static-error and phase difference, is a function of the actual controller stiffness or PD-controller settings. More specifically, the PD-controller stiffness and damping properties defined by the proportional- and derivative constant determine the actual handlebar tracking performance. A PD-controller with a proportional constant of 12 Nm/rad and a derivative constant of 0.6 Nms/rad shows a frequency response as shown in figure 5-26 for both the steering assembly as well as the handlebar assembly.

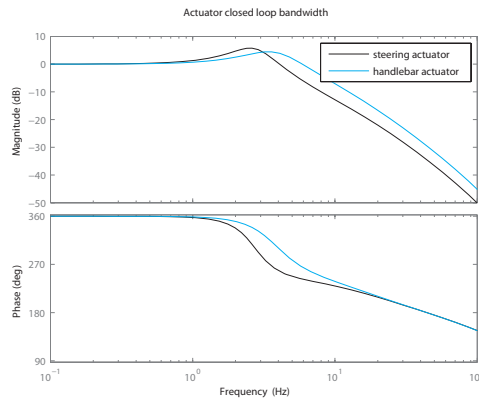


Figure 5-26: The bode plot indicating the frequency response of the steering- and handlebar assembly. The bandwidth of the steering- and handlebar assembly is a function of the PD-controller coefficients which are defined as proportional constant of 12 Nm/rad and a derivative constant of 0.6 Nms/rad respectively. Appropriate selection of the PD-controller coefficients can eliminate the resonance-peaks and increase the bandwidth.

The different geometric amplification ratio between the steering- and handlebar assembly as well as different rotational inertia properties, causes a different frequency response and bandwidth between the handlebar actuator and steering actuator. In order to gain the smallest position error and fastest response, the proportional and derivative gains should be as high as possible without exceeding the actuator output torque and output power capabilities. As well as the limited actuator output torque, the position control structure as shown in figure 5-24 also limits the maximum controller gains as the control loop can become unstable.

Stability

Figure 5-27 shows the PD-controller design including the two individual control loops for the steering- and handlebar assembly. From left to right, the PD-controller algorithm running on the microcontroller produces an analog output voltage which is wired to the EPOS2 motor-amplifier. The motor-amplifiers are configured as current-amplifiers with a gain of 4 A/V. The motor-amplifiers control the actuators by regulating the current flowing through the motor windings producing a torque at the output shaft defined by the torque-constant K_t of 0.217 Nm/A. The gear-belt construction at the handlebar- and steering-assembly allows for an effective increase in output torque. The resulting handlebar torque T_θ and steer torque T_δ interact with the rider input torque T_h and interaction torque with the environment (ground surface) T_e . The resulting torques interacting with the inertial properties of the handlebar- and steering-assemblies result in a specific handlebar- and steering-angle position. The sensor blocks both provide angular position- and angular rate information to the controller closing the feedback loop.

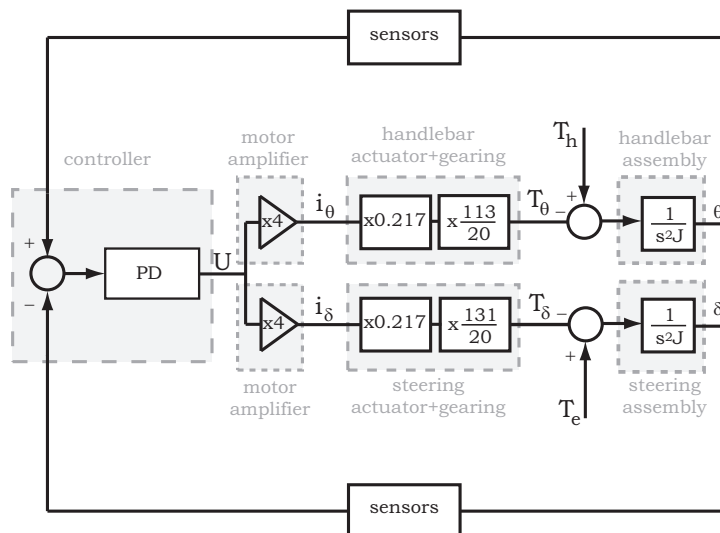


Figure 5-27: A block diagram showing the steering- and handlebar feedback loops. The individual motor-amplifier gains as well as the actuator gains and output torque multiplication stages by the gear assemblies are visualized. The resulting actuator torques T_θ and T_δ interact with the rider torque T_h and environment interaction torque T_e . The resulting torque components interact with the handlebar- and steering assembly inertial properties which results in a specific handlebar angle- and steering angle respectively. The sensor blocks provides angle- and angular rate information to the controller which are used to close the feedback loop. Note that due to the unequal gear-gelt ratios between the handlebar- and steering assembly, the handlebar torque is also unequal to the steer torque if a single PD-controller output signal is used (as depicted).

The schematic as shown in figure 5-27 essentially consists of two position feedback loops, the top-loop is used to provide the steer-torque at the handlebars allowing the driver to perceive the steer torque at the handlebars by interaction with the environmental disturbance torque. The bottom-loop is used to position the steering assembly as requested by the handlebar input. If both loops are analyzed separately, the handlebar position control feedback structure is given by the following transfer function which shows the relation between the actuator

voltage input $U(s)$ and output position $\theta(s)$,

$$\frac{\theta(s)}{U(s)} = \frac{K_t}{s((sJ_h)(sL_w + R_w))} \quad (5-22)$$

where the torque constant K_t , winding inductance L_w and winding resistance R_w are given in table 5-4. Note that coulomb friction is neglected and the speed constant K_n due to the use of a current controller is equal to zero, and not present in the equation. The handlebar assembly inertia equals to $J_h=0.038 \text{ kgm}^2$. To be able to select the highest controller gain setting, a root locus design method is performed which gives valuable information about the stability boundaries of a particular closed loop feedback system if the overall controller gain is adjusted.

The open loop transfer function between the motor position and input voltage is analyzed in the digital domain at a sample frequency of 1 kHz. The analog output filter-stage on the IO-board of the controller is modeled as two cascaded first-order low-pass filters as described in section 5-2-2. The limited bandwidth of the low-pass filtered position sensor signal (10 Hz) and angular rate gyro signal (10 Hz) are modeled as cascaded, first-order low-pass filters to account for delays and phase-lag characteristics.

Figure 5-28a and figure 5-28c show the open-loop discrete root locus of the handlebar- and steering-assembly at the current PD-controller settings as described in section 5-3-2. A close-up is shown in figure 5-28b and figure 5-28d for the handlebar- and steering-assembly respectively. The branches depart from the origin with increasing gain K thereby effectively increasing the controller stiffness at an unfavorable decrease in damping ratio as the poles move up to the border of the unit circle. As already observable in figure 5-26 the current PD-controller coefficients do not provide a critically damped response for both the handlebar assembly as well as the steering assembly indicated by the lightly damped resonance peaks in the magnitude plot. Due to the different geometric amplification ratio between the steering- and handlebar-assembly as well as different rotational inertia properties, the instability boundary gain K as shown in the figures differs in magnitude between the two.

The current system dynamics actually limit the tracking performance between the handlebar- and steering assembly without operating the actuators near its torque and power limits. A suitable filter could provide a solution to force the poles more inwards in the root locus plots. However for initial testing purposes and to provide an optimal positioning response for both the handlebar- and steering assembly, a double PD-controller layout is used inside the controller block from figure 5-27. Two individual PD-controllers can provide a better positioning response for both the handlebar- and steering assembly without driving one assembly to instability by a too high PD-controller gain.

For initial testing purposes a double set of PD-controller coefficients is utilized to provide a better response for both the handlebar- and steering assembly. A slightly under damped response for both the handlebar- and steering assembly result in controller coefficients of $K_p=8 \text{ Nm/rad}$ and $K_d=0.6 \text{ Nms/rad}$ for the handlebar assembly and $K_p=15 \text{ Nm/rad}$ and $K_d=1.5 \text{ Nms/rad}$ for the steering assembly.

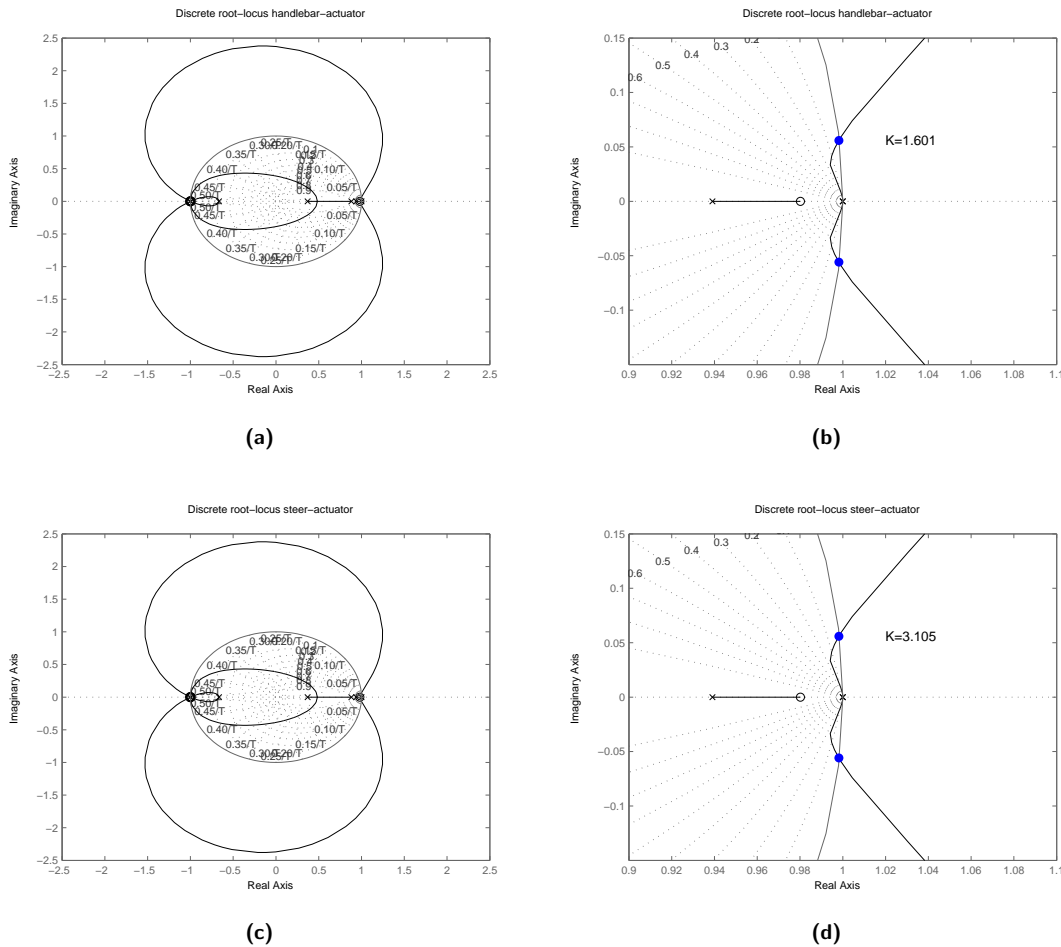


Figure 5-28: The open-loop discrete root locus of the handlebar- (a) and steering-assembly (c) at the current PD-controller settings as described in section 5-3-2. A close-up is shown in figure (b) and figure (d) for the handlebar- and steering-assembly respectively. The branches depart from the origin with increasing gain K thereby effectively increasing the controller stiffness at an unfavorable decrease in damping ratio as the poles move up to the border of the unit circle.

5-4 Firmware

As shown in section 5-1-1 the controller firmware is developed with the use of the graphical Simulink LK-blockset toolbox. The main controller loop is shown in figure 5-29 which shows the fundamental ADC-, DAC-, (serial port) datalog- and various subsystem-blocks. The controller firmware loops continuously at a sample frequency of 1 kHz reading the analog inputs and providing an analog output to the motor-amplifiers.

Appendix E shows the individual internal function-block layout, however a short description of each individual block is given below. The Principal Control-loop defines the tracking performance between the handlebar- and steering-assembly position. The Auxiliary Control-loop is able to implement an additional Enhanced Stability Control- or Pole Placement Control-loop algorithm as described in section 4-3 and 4-4.

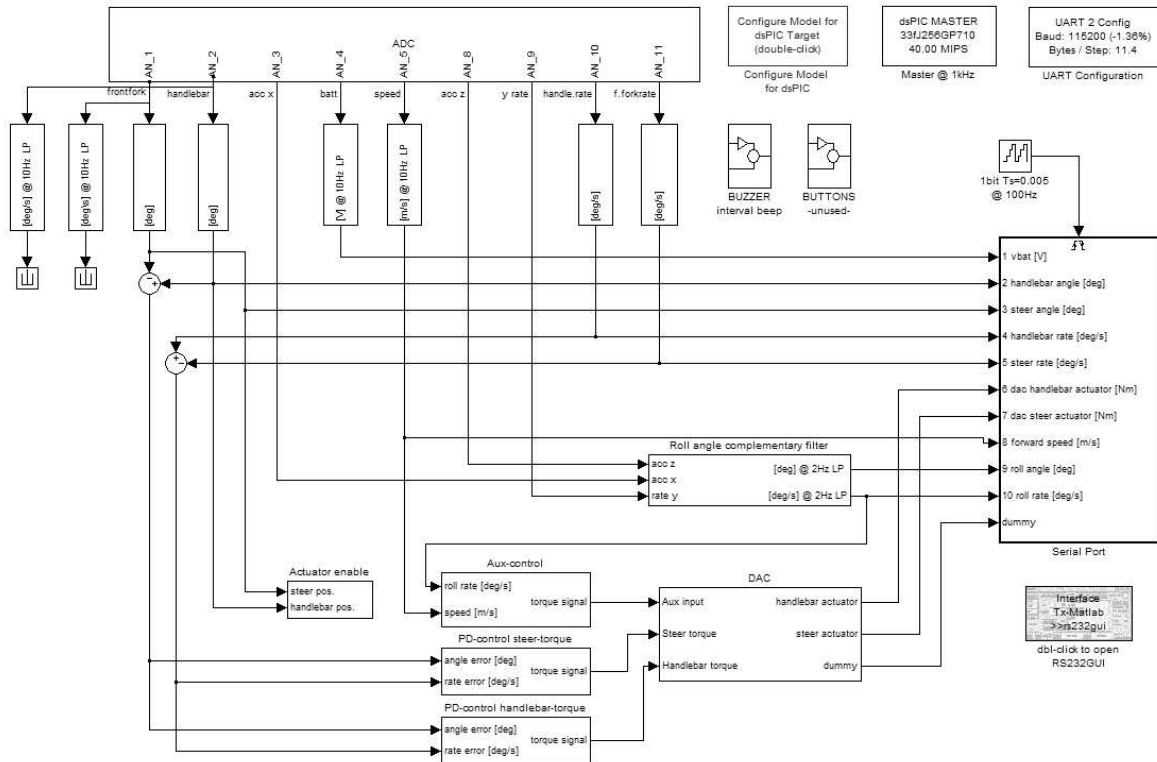


Figure 5-29: The graphical Simulink controller firmware layout for the steer-by-wire bicycle which shows the separate fundamental ADC-, DAC-, datalog- and various subsystem-blocks. The control-loop runs at a sample frequency of 1 kHz, evaluates sensor information at the analog inputs, processes the information in the various subsystem-blocks and outputs an analog voltage to the motor-amplifier accordingly.

5-4-1 Principal Control structure

ADC block

The ADC block samples the sensors connected to the designated analog input ports. Channel AN_1 to AN_11 corresponds to the pin-out description in the microcontroller datasheet. The ADC samples the analog inputs with a 12bit resolution at a 1 kHz sample frequency. An analog voltage between 0 V and 3.3 V is converted to a linear proportional digital value of 0 to 4096.

Analog signal conversion blocks

After analog to digital conversion, the digital values are converted in the vertical function-blocks to actual physical units by each individual sensor. Each block calculates the actual physical dimension as a function of the sensor sensitivity as specified by the manufacturer. Noisy sensor signals are additionally filtered with a discrete low-pass filter which is indicated by the LP notation preceded by the cutoff frequency in Hz.

Actuator enable block

During initial power-on, the motor-amplifiers are disabled preventing undesired movement of the actuators if the microcontroller initializes and the analog output is not under full control. When the microcontroller has initialized the actuators are both enabled if the absolute angle difference between the steering- and handlebar-assembly is smaller than five degrees. If the enable threshold is satisfied, the enable signal latches to the on-state until the power is cycled by the main on-off switch.

PD-control blocks

The PD-control function blocks evaluates the difference of the steering- and handlebar assembly position as well as the steer- and handlebar angular rate signals and multiplies the values with the PD-controller coefficients. Two individual PD-controllers are utilized which individually control the steering- and handlebar actuator. The resulting torque signal is passed to the DAC function-block.

DAC block

The DAC function-block generates the PWM output of the microcontroller adjusting the duty-cycle based on the torque requirements defined in the PD-control and Aux-control function blocks.

Serial port block

The serial port block is able to send signals of interest to the serial port of the controller board. Real-time datalogging is performed by a laptop PC connected to this serial port. The data is transferred to the laptop PC with a transfer-rate of 115200 bps, or 14400 Bps. Each channel sends a two byte variable, however data transfer for each channel required three Bytes. The serial port is able to send a maximum of 4800 two-byte variables per second. Data is send as the Serial Port function block is triggered, which occurs at the rising- and falling-edge of the 1-bit free-running-counter block. By adjusting the sample-time of the free-running-counter block, the sample frequency of the data-acquisition can be adjusted.

5-4-2 Auxiliary Control structure

Aux-control block

The Aux-control block, or auxiliary block is used to provide an additional steer torque based on sensor information to implement a stability enhancement algorithm as described in section 4-3 and 4-4. Like the handlebar-tracking PD-control signals, the auxiliary torque signal is passed to the DAC function-block to actuate the steering- and handlebar assembly accordingly.

5-5 Summary

In this chapter the actual implementation of a steer-by-wire system on a conventional bicycle is covered. The firmware development software tools and controller hardware selection are closely related and form the foundation of the steer-by-wire prototype. A low-cost general purpose microcontroller development board is selected with the addition of a custom IO-board to interface with the sensors and actuators on the bicycle. The integration of the forward speed sensor, angular position- and angular rate sensors are covered, as well as the roll angle sensor on the bicycle. The physical implementation of the roll angle sensor by inertial angle estimation does not yet provide an accurate estimate of the bicycle roll angle. However a design is proposed to improve the roll angle estimation by an alternative optical distance measurement. The actuator selection is covered by selection criteria based on measurement data from previous research and time-simulations to predict the torque- and power requirements. The virtual stiffness between the handlebar- and steering assembly is however limited by the utilized PD-control structure. Instability behavior due to limited actuator-, sensor- and controller bandwidth characteristics require a more advanced control implementation to actually utilize the maximum torque the actuators can deliver. Without covering an in-dept analysis of suitable control structures to increase the virtual handlebar-, steering assembly stiffness a double PD-controller set of coefficients is utilized on the steer-by-wire bicycle prototype for initial testing purposes. The following chapter will cover the experimental tests to evaluate the Stability Enhancement algorithm as described in the previous chapter.

Experimental Tests

In chapter 3 it is shown that a conventional bicycle at low forward speeds can be highly unstable. However a bicycle equipped with a steer-by-wire system can be stabilized as shown by the Low Speed Stabilization algorithm in section 4-3. In order to evaluate the proposed algorithm, experimental tests have been conducted with the steer-by-wire bicycle prototype on a flat, empty, asphalt car park. Sensor data and relevant internal variables are send real-time to a laptop, which is carried by the rider in a backpack for datalogging purposes and off-line analysis. First the steering feel or steer torque feedback response of the steer-by-wire bicycle is compared to a conventional steered Batavus Browser bicycle.

6-1 Steer Torque Feedback Steer-by-Wire Bicycle

In section 4-5 it is shown that the limited stiffness provided by the PD-controller coefficients on the Steer-by-Wire Bicycle model compared to the Benchmark Bicycle model, has a significant contribution on the steer stiffness or steer torque feedback magnitude difference between the two analytical models. An identical steer stiffness analysis is conducted with accurate geometric-, mass- and inertia parameters from the Batavus Browser bicycle, obtained from a publication by [Kooijman et al., 2009]. Applying the proposed dual PD-controller coefficient layout as in section 5-3-2 allows to compare the steer stiffness of the Steer-by-Wire Bicycle prototype to a conventional steered Batavus Browser bicycle. Figure 6-1a shows the steer stiffness magnitude plot of a conventional steered Batavus Browser bicycle on top of the steer stiffness magnitude plot of the Steer-by-Wire Bicycle prototype.

Figure 6-1b shows a more visible comparison as it shows the ratio between the steer stiffness magnitude of a conventional steered Browser bicycle over the steer stiffness of the steer-by-wire bicycle prototype. A decrease in steer stiffness or steering feel is apparent on the steer-by-wire bicycle. At low steer frequencies and low forward speeds, the steer stiffness magnitude ratio is about unity. At higher steer frequencies and higher forward speeds the steer stiffness ratio increases, which implies the steer stiffness of the steer-by-wire bicycle reduces in comparison to the steer stiffness of the conventional steered browser bicycle.

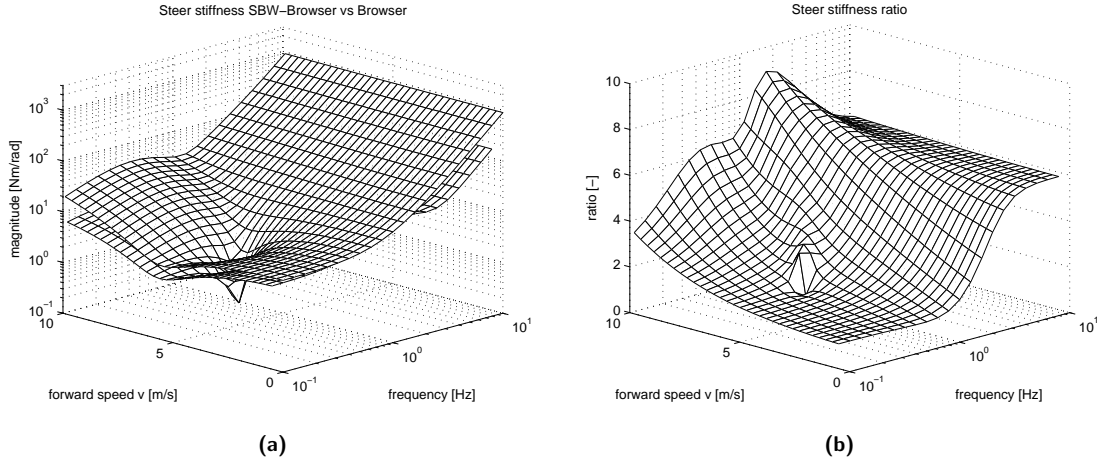


Figure 6-1: The steer stiffness plot of a conventional steered Browser bicycle on top of the steer stiffness plot of the steer-by-wire bicycle prototype (a). A decrease in handlebar torque is apparent on the steer-by-wire bicycle due to the limited stiffness provided by the PD-controller coupling. A more clarifying plot (b) shows the numerical ratio between the steer stiffness magnitude of a conventional steered Browser bicycle over the steer stiffness of the steer-by-wire bicycle. At higher forward speeds and higher steer frequencies the perceived steer stiffness on the steer-by-wire bicycle reduces in magnitude by a factor as shown in the surface-plot.

During experimental evaluation of the Low Speed Stabilization algorithm however, the double PD-controller layout is implemented as the tracking performance between the handlebar- and steering assembly is sufficient for the proposed PD-controller coefficients. Likewise as the steer stiffness magnitude on the steer-by-wire bicycle prototype is reduced in comparison to a conventional steered bicycle, the PD-controller layout is able to provide a significant handlebar feedback torque. Without investigating the effects of a scaled handlebar feedback torque to the rider's perception, the effect of a completely disabled handlebar feedback torque will be covered in the following section.

6-2 Low Speed Stabilization

To be able to quantify the theoretical effect of the Low Speed Stabilization control on the lateral motion and stability boundaries of the steer-by-wire bicycle prototype, the eigenvalue analysis is re-calculated with accurate geometric-, mass- and inertia parameters from the Batavus Browser bicycle. Utilizing appropriate parameters and applying a control algorithm according to equation 6-1,

$$T_{SE} = K_s(v_{avg} - v)\dot{\phi} \quad (6-1)$$

with $v_{avg}=7$ m/s, a stabilizing control action can be observed for positive gains $K_s=[5,10]$ Ns^2/rad as demonstrated in figure 6-2c and 6-2d respectively. Figure 6-2b shows the eigenvalue plot of the steer-by-wire bicycle without any additional stabilizing control, whereas for completeness a destabilizing control action is shown in figure 6-2a by utilizing a negative gain $K_s=-5$ Ns^2/rad which dramatically decreases the auto-stable forward speed region.

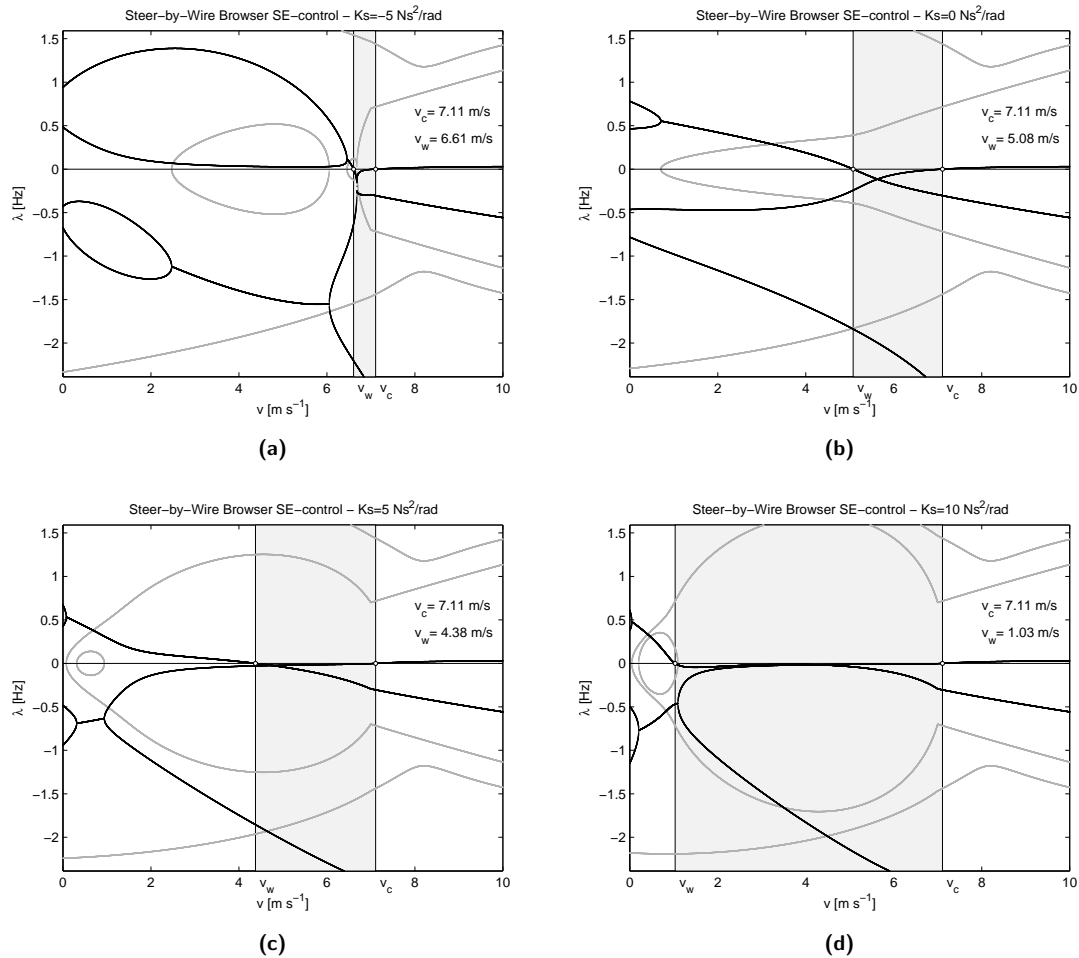


Figure 6-2: Eigenvalue plots for the steer-by-wire bicycle prototype utilizing a Low Speed Stabilization algorithm (SE-control) for different gains K_s as a function of forward speed v . A destabilizing negative gain $K_s = -5 \text{ Ns}^2/\text{rad}$ shows an unstable bicycle (a) for almost all forward speeds. A gain $K_s = 0 \text{ Ns}^2/\text{rad}$ effectively disables the stabilizing action and subsequently shows the stability characteristics (b) of the steer-by-wire bicycle without additional control. Utilizing a positive gain $K_s = 5 \text{ Ns}^2/\text{rad}$ (c) and $K_s = 10 \text{ Ns}^2/\text{rad}$ (d) shows the stabilizing properties for the lateral motion of the bicycle by a decreasing weave-speed from 4.4 m/s to 1.0 m/s respectively.

6-2-1 Test procedure

The eigenvalue plots in figure 6-2 show interesting properties with respect to the stability boundaries as a function of the controller gains K_s which scales the stabilizing control torque on the steering assembly. Two different experiments have been conducted, a ride along a predefined path and a lane-change obstacle avoidance manoeuvre to evaluate different controller gain settings.

Path following test

Experimental tests at controller gains $K_s = [-5, 0, 5, 10] \text{ Ns}^2/\text{rad}$ are performed at constant forward speeds of $v = [5, 10, 15, 20] \text{ km/h}$ by riding the bicycle at a predefined track along a path as shown in figure 6-3. A rectangular shaped path was marked on the asphalt roughly equal

to the dimensions shown in the figure which contains nine straight sections, three right-hand corners and five left-hand corners. The bicycle was ridden along a path from start/stop, through turns t_1 to t_8 and back to the start/stop position.



Figure 6-3: Path following test with the steer-by-wire bicycle at the track along a predefined path as shown on the map overlay. A laptop carried in the backpack and connected to the serial-port of the controller was used to store sensor-data and relevant internal controller variables for off-line analysis.

Lane change test

Experimental tests by performing a lane change avoidance manoeuvre at controller gains $K_s=[0,5,10]$ Ns^2/rad are performed at constant forward speeds of $v=[5,10,15,20]$ km/h by riding the bicycle at a predefined track along a path as shown in figure 6-4. The bicycle ridden from the start position to halfway of the track at which a sudden left or right direction command is shown. After the avoidance manoeuvre the bicycle progressed along a section at a distance of 3 m from the center-line at which the avoidance manoeuvre was initiated.

6-2-2 Data analysis

Eleven parameters are send by the controller to the laptop and stored for off-line analysis. The battery voltage, handlebar- and steering angle, handlebar- and steering rate, handlebar actuator- and steering actuator torque command, forward speed, roll-angle and roll-rate as well as the additional stabilizing torque T_{SE} are stored during each test run.



Figure 6-4: Lane change test with the steer-by-wire bicycle at the track along a predefined path as shown on the map overlay. The bicycle is ridden from the start position to halfway of the track at which a sudden left or right direction command is given onto section L1 or section L2.

Path following data analysis

From the eigenvalue plots shown in figure 6-2 it shows that the weave-speed at which the bicycle becomes self-stable decreases as a function of increasing gain K_s . It should therefore become more easy for the driver to stabilize the bicycle and should require less steer input to follow a predefined path. In order to test this hypothesis, the motion of the handlebar is investigated in the frequency domain by analysis of the Power Spectral Density (PSD) on the handlebar rate signal.

The power spectral density gives the power of a signal as a function of frequency. By analyzing the handlebar rate signal a bias or offset in the handlebar position signal is eliminated. Figure 6-5 shows a matrix of power spectral density plots of each individual test. The horizontal axis show the frequency content of the handlebar rate signal from 0 to 4 Hz whereas the vertical axis shows the magnitude of the handlebar rate signal from 0 to 15 $(\text{deg/s})^2/\text{Hz}$. The columns in the total figure show results at a constant controller gain K_s whereas the individual rows show a constant forward speed v .

The sum P_h of the power spectral density magnitude and frequency can be conceived as a measure for the total effort the rider has put on the handlebars, during a single run along the track and is indicated in each individual figure. Observations from the test results as shown in figure 6-5:

- ▷ Test runs at a single specific forward speed show a decreasing rider effort P_h with increasing gain K_s , especially at a low forward speed of 5 km/h. This shows the significant

effect which the low speed stabilization control algorithm has on the lateral stability of the bicycle. A destabilizing gain K_s actually shows a significant increase in rider effort to control the bicycle as already predicted from the eigenvalue plot in figure 6-2a. At higher forward speeds, the stabilizing control torque decreases and subsequently only a relatively small improvement at higher gain K_s is present at higher forward speeds.

- ▷ At a maximum controller gain of $K_s=10 \text{ Ns}^2/\text{rad}$ the rider effort to control the bicycle becomes more or less constant irrespective of the forward speed. This actually shows that the bicycle is as easy to control at low speeds ($v=5 \text{ km/h}$) as it is at high speeds ($v=20 \text{ km/h}$), whereas the bicycle without additional control at $K_s=0 \text{ Ns}^2/\text{rad}$ requires twice as much rider effort at 5 km/h as compared to riding the bicycle at 20 km/h .
- ▷ The significant peaks in the plots for gain $K_s=10 \text{ Ns}^2/\text{rad}$ at 1 Hz to 1.5 Hz correspond closely to the weave frequency indicated by the dashed black lines. At lower controller gains K_s however, the distinct peaks become less present in magnitude and the frequency peaks do not correspond very well to the weave frequencies. The dominant frequency content is actually defined by the peddling frequency by the rider indicated by the blue lines. At lower controller gains K_s the lateral motion of the bicycle is not predominantly defined by the bicycle-controller combination, but rather the un-modeled bicycle-rider combination, therefore the weave frequencies do not match correctly. This shows actually the effect of bicycle-rider interaction if the rider is physically attached to the steering-assembly by holding the handlebars and contributing to the overall bicycle-rider dynamics.
- ▷ Tests at forwards speeds of $v=[5,15,20] \text{ km/h}$ show a decreasing rider effort with increasing controller gain K_s , and subsequently at constant controller gain K_s and increasing forward speed rider effort again decreases as expected. However rider effort at a forward speed of $v=10 \text{ km/h}$ decreases unexpectedly fast at zero and low controller gains K_s .

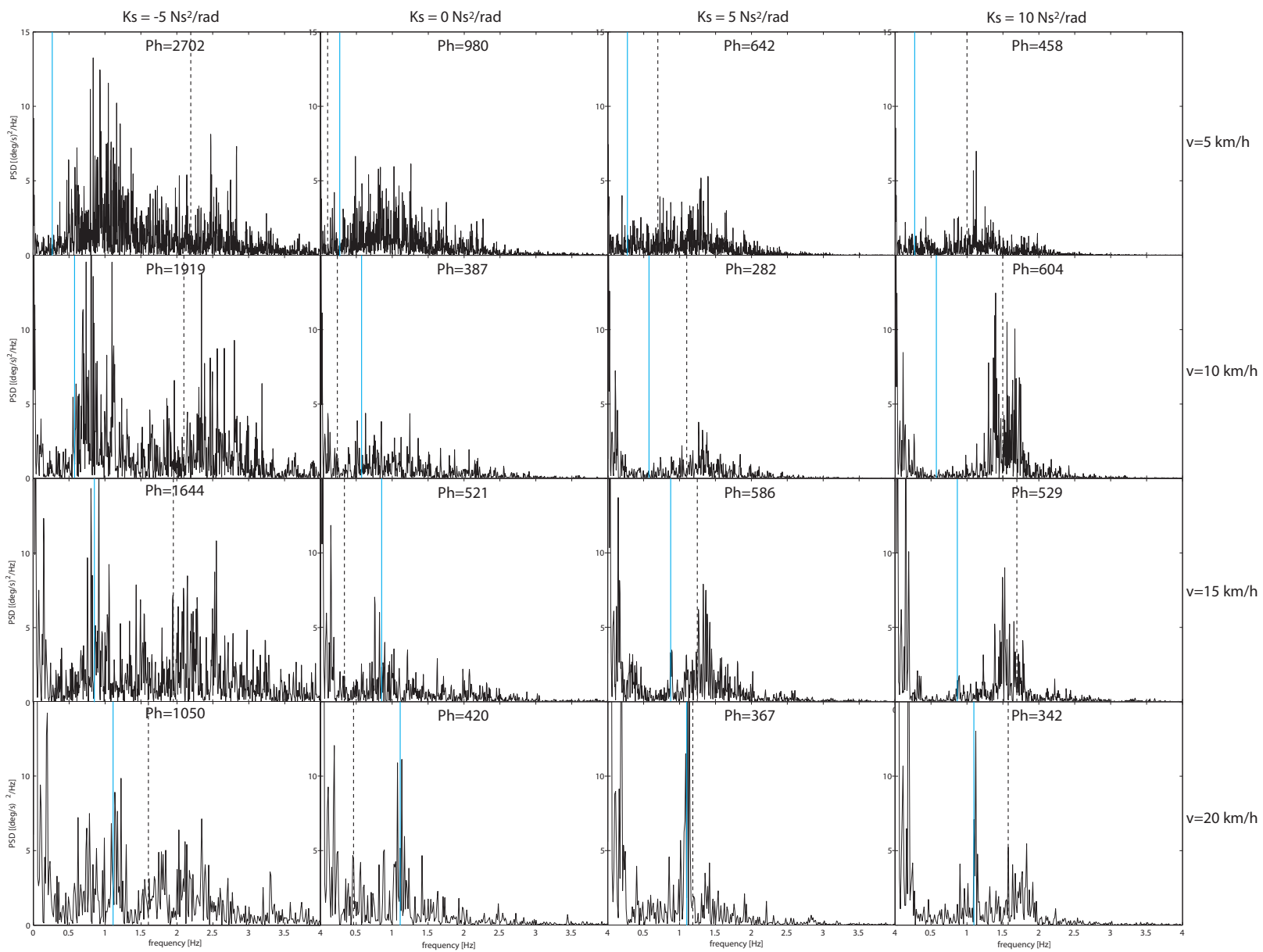


Figure 6-5: Low Speed Stabilization control algorithm test results. Each plot shows the power spectral density (PSD) of the handlebar rate at $v=[5,10,15,20]$ km/h and $K_s=[-5,0,5,10]$ Ns²/rad. Plots along rows show a constant forward speed, plots along columns show a constant controller gain. The weave-frequencies from the model are indicated with a black dashed line whereas the pedaling frequency is indicated by a continuous blue line. The bicycle at 5 km/h with active Low Speed Stabilization control ($K_s=10$) requires an equal amount of rider input as compared to a bicycle without additional control ($K_s=0$) at a higher auto-stable forward speed of 20 km/h.

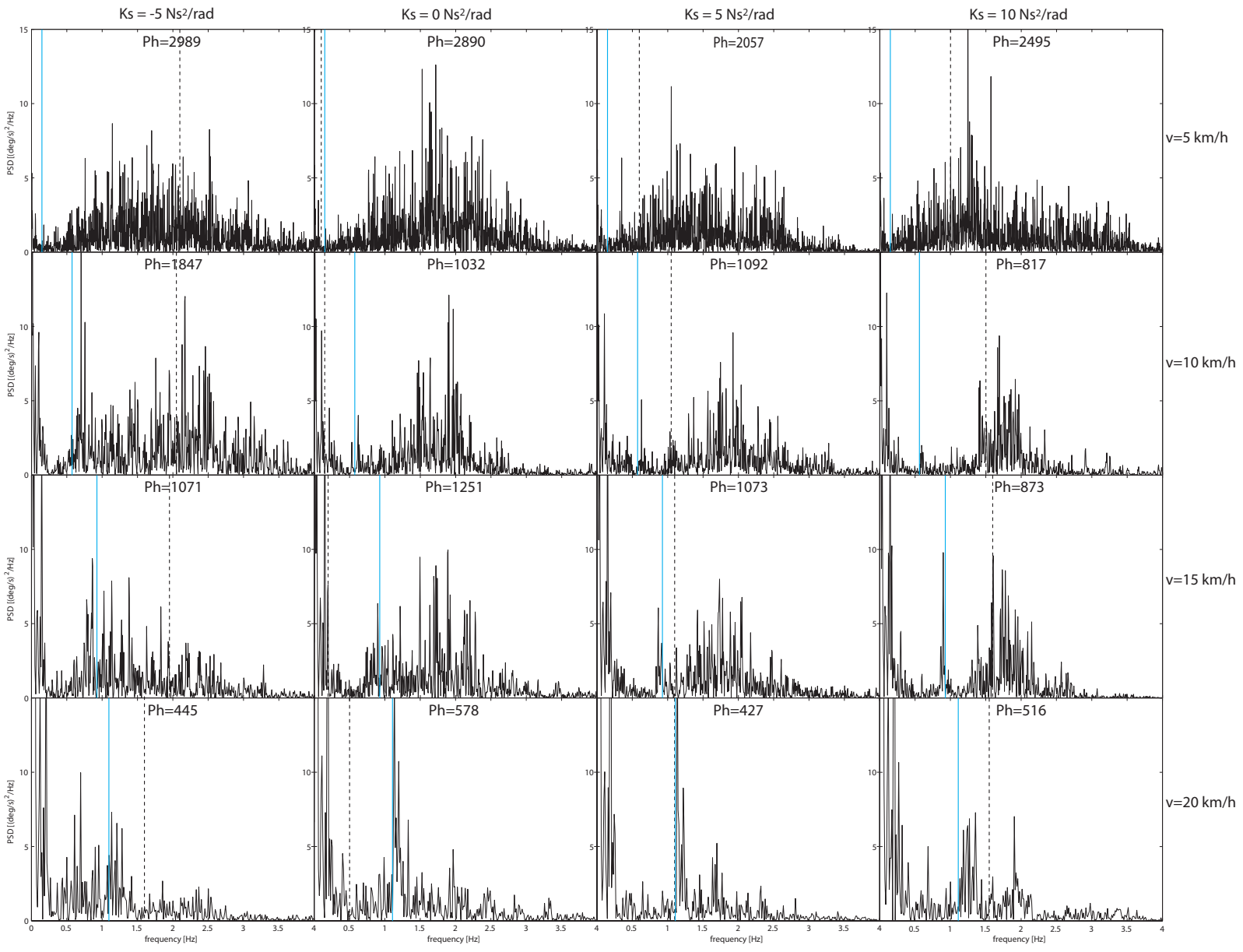


Figure 6-6: Test results with disabled feedback torque actuator. In comparison to the test results with feedback torque at the handlebars, the rider effort P_h does not decrease with increasing controller gain K_s . Rider effort without feedback and disabled lateral stability control $K_s = 0 \text{ Ns}^2/\text{rad}$ at all forward speeds is about two times higher in comparison to the feedback enabled tests.

An identical test procedure was conducted with a disabled feedback actuator. Without feedback torque to the handlebars, the steering assembly of the bicycle is subsequently controlled by the angular position of the handlebar. Free movement of the steering assembly is restricted as the steering assembly is now position controlled instead of torque controlled. Observations from the test results without torque feedback to the handlebars as shown in figure 6-6:

- ▷ Test runs at a forward speed of 5 km/h for all controller gains K_s , in comparison to the test runs with an enabled feedback torque actuator, do not show a significant decrease in rider effort P_h with increasing controller gain K_s .
- ▷ The absence of feedback torque at the handlebars show a significant increase in rider effort P_h in comparison to the feedback torque enabled tests. This applies to all forward speeds at zero and the two positive feedback gains K_s . Rider effort P_h with a destabilizing controller gain $K_s = -5 \text{ N s}^2/\text{rad}$ shows a decrease in comparison to the feedback enabled test runs. The controller induced destabilizing control action is less effective in comparison to the feedback enabled tests.
- ▷ The rider effort P_h at each individual controller gain K_s decreases with increasing forward speed. Even a position controlled steering assembly at which the bicycle shows no self stable lateral behavior, shows a decreasing rider steer effort.
- ▷ At forward speeds of $v = [5, 10, 15]$ km/h at zero and the two positive feedback gains K_s , the rider steer motion without feedback torque is dominantly centered around a steer frequency of 2 Hz. Whereas with an enabled feedback actuator the peaks in the PSD plots are more specifically centered around the weave frequencies indicated by the dotted black lines.

Comparing the test results between the feedback torque enabled and disabled test runs show some interesting results. Table 6-1 summarizes the rider effort index P_h at all forward speeds v and all feedback gains K_s with enabled- and disabled handlebar feedback torque. The rider effort index P_h with feedback to the handlebars for all test runs except the destabilizing control algorithm, show a decrease in comparison to the test runs without feedback. The destabilizing controller setting at $K_s = -5 \text{ N s}^2/\text{rad}$ shows an increase in rider effort with feedback at the handlebars in contrast to the above mentioned observation. This however is to be expected as the destabilizing control torque is transferred to the rider by the handlebar actuator. This shows the importance of steer torque feedback during bicycle riding as one of the human sensory inputs to effectively stabilize the lateral motion of the bicycle. More specifically, comparing the rider effort index between experiments with- and without feedback torque at $K_s = 0 \text{ N s}^2/\text{rad}$, the steer effort without feedback is about three times higher at 5 km/h. Rider effort without feedback is just under three times higher at 10 km/h, two and a half times higher at 15 km/h and just under one and a half times higher at 20 km/h respectively in comparison to identical experiments with steer torque feedback at the handlebar.

Both experiments with an enabled and disabled feedback actuator generally show a lower steer effort at increasing forward speeds. Test runs with enabled feedback torque at the handlebars show a decrease in steer effort due to the self stabilizing properties of the bicycle. This however is not the case for the test runs with disabled feedback torque, as the bicycle shows no self stable behavior due to the angular position control on the steering assembly. The observed

	$K_s=-5 \text{Ns}^2/\text{rad}$	$K_s=0 \text{Ns}^2/\text{rad}$	$K_s=5 \text{Ns}^2/\text{rad}$	$K_s=10 \text{Ns}^2/\text{rad}$
$v=5 \text{ km/h}$	2702 / 2989	0980 / 2890	0642 / 2057	0458 / 2495
$v=10 \text{ km/h}$	1919 / 1847	0387 / 1032	0282 / 1092	0604 / 0817
$v=15 \text{ km/h}$	1644 / 1071	0512 / 1251	0586 / 1073	0529 / 0873
$v=20 \text{ km/h}$	1050 / 0445	0420 / 0578	0367 / 0427	0342 / 0516

Table 6-1: Steer effort index P_h as shown in figure 6-5 and 6-6 which shows the effect of an enabled- and disabled handlebar feedback torque at different forward speeds v and feedback gains K_s . The feedback torque enabled steer effort index is shown in bold. A higher index relates to a larger rider handlebar input or higher rider effort to stabilize the bicycle.

decrease in steer effort at increasing forward speeds should originate from rider control based on sensory input other than feedback at the handlebars. Exclusively visual- or vestibular cues should provide the rider the required sensory information to control the lateral motion of the bicycle, as no feedback torque at the handlebars could assist the rider at its stabilizing task. Table 6-1 shows the numerical values of the rider steer effort index during each experiment with and without handlebar feedback. The contribution of the proprioceptive cues perceived at the handlebars by enabling the handlebar feedback, is primarily indicated by the numeric difference between the rider effort index. This also shows the relatively large contribution of the proprioceptive cues by the handlebar feedback at low forward speeds, in comparison to the visual- and vestibular cues as the rider effort index value difference decreases with increasing forward speeds.

The tracking performance between the handlebar- and steering assembly as a function of input frequency is visualized by investigating the power spectral density of the difference between the handlebar- and steer angle. Figure 6-7 shows the power spectral density of the error angle with feedback to the handlebars. The angular difference between the handlebar- and steering assembly is a function of the PD-controller stiffness properties and the input torque originating from the environment- and rider interaction. Figure 6-8 shows the power spectral density of the error angle without feedback to the handlebars.

The power spectral density plots between the test runs with feedback and without feedback have a very similar distribution. Both experiments show the highest error angle with a destabilizing controller action at $K_s=-5 \text{Ns}^2/\text{rad}$ and significant peaks at the peddling frequency at test runs at higher forward speeds. The total error angle summation over frequency during each run is indicated by the P_e index in each individual plot. Despite the similar frequency distribution between the feedback enabled and -disabled test runs, the total error angle summation is slightly higher for the test runs with a disabled feedback actuator. The higher frequency content in the steer motion without feedback, is probably the cause of the slightly higher angular deviation between the handlebar- and steering assembly.

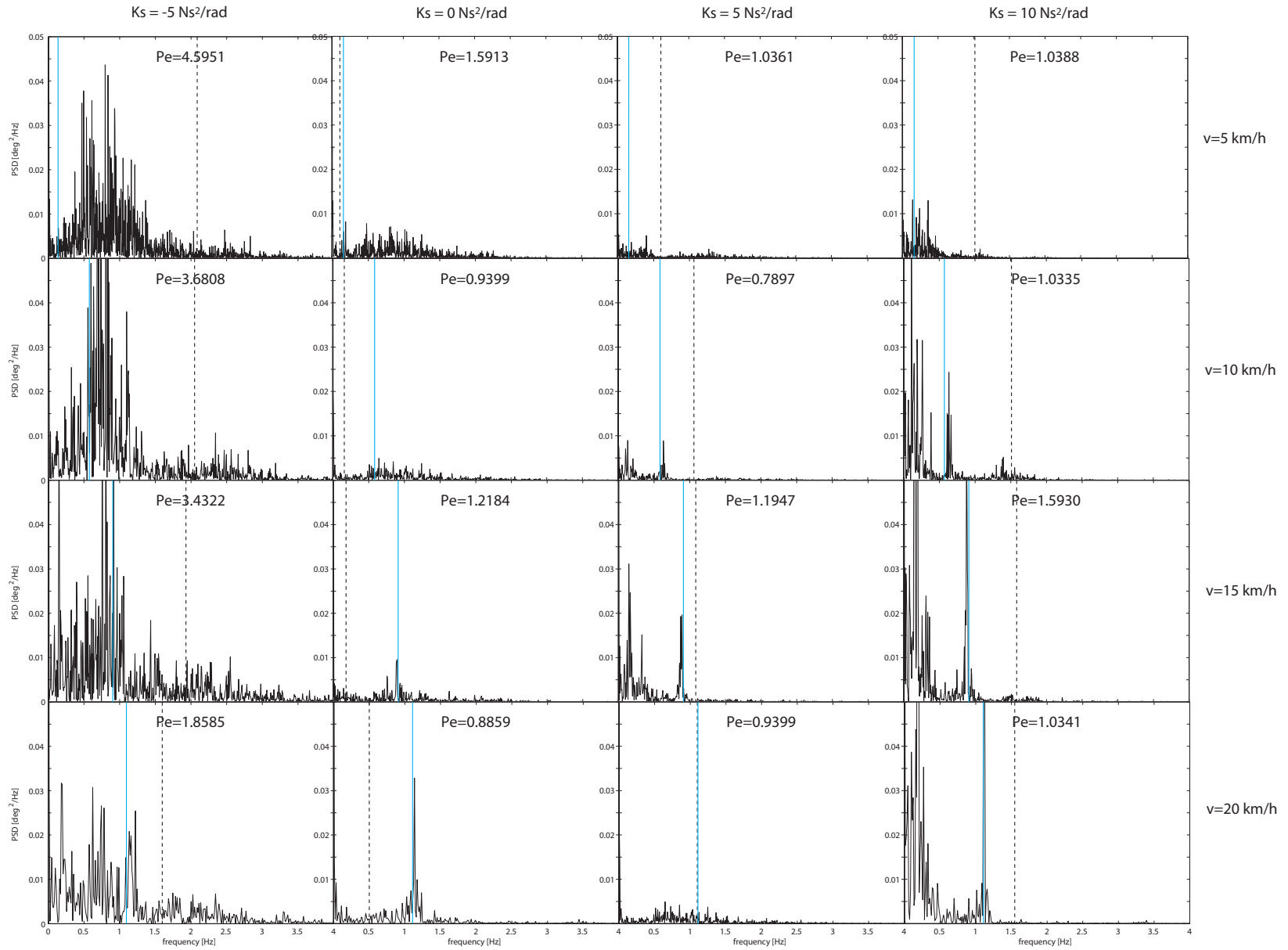
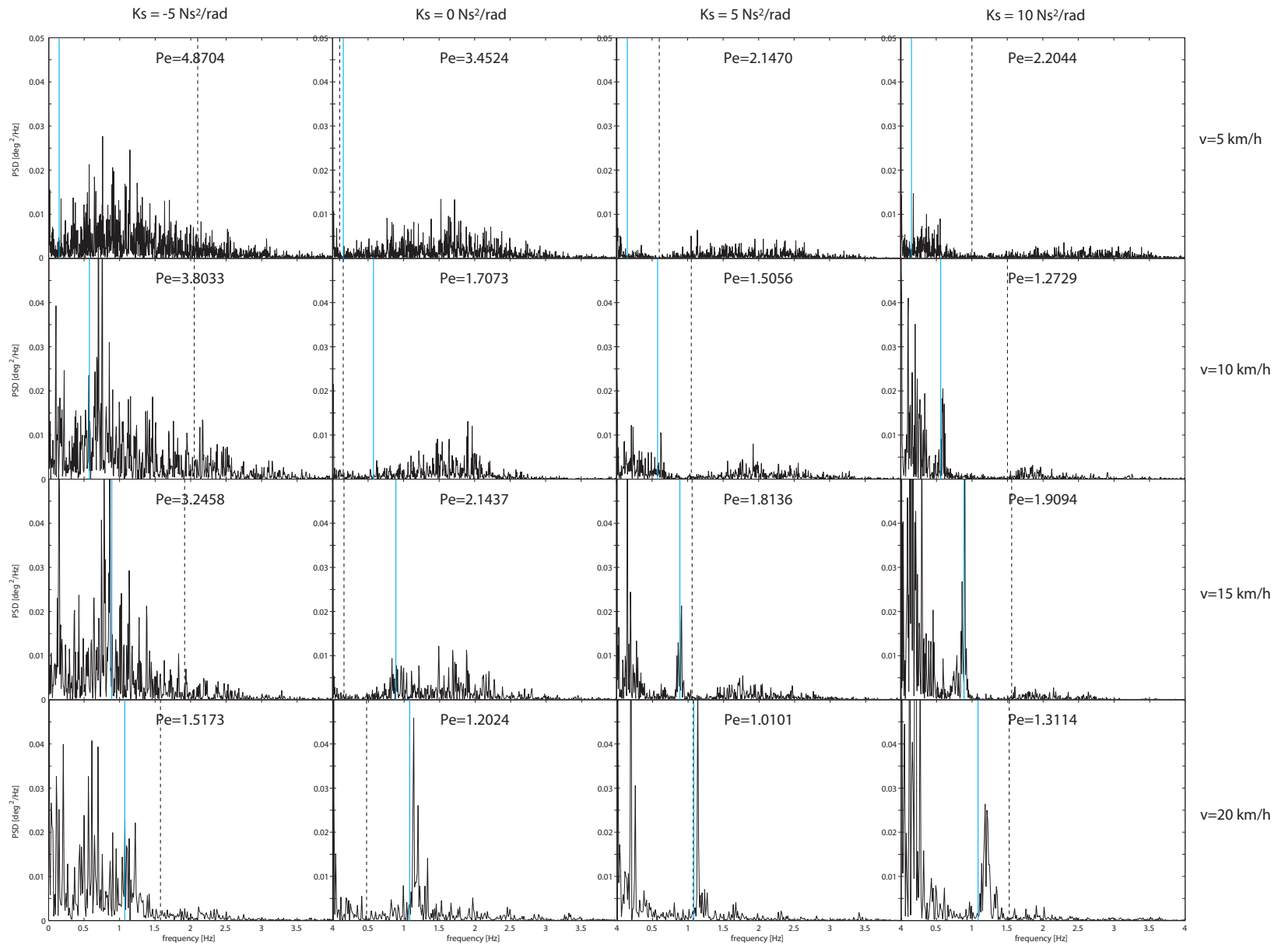


Figure 6-7: Test results of the power spectral density of the angle difference between the handlebar- and steering assembly with enabled feedback torque. The error angle between handlebar- and steer assembly is significantly higher when a destabilizing control action is used.

Figure 6-8: Test results of the power spectral density of the angle difference between the handbar- and steering assembly with disabled feedback torque. In comparison to the feedback enabled test runs the error angle is slightly higher due to a more high frequency steer motion content.



Lane change data analysis

The path following experiment shows the ability to stabilize the lateral motion of the bicycle, by applying an additional control torque at the steering assembly. By effectively steering into the direction of the fall, the bicycle will eventually upright itself again as the front wheel contact patch moves back underneath the center of gravity. Intentionally steering the bicycle in a turn causes the bicycle to roll, creating a non-zero roll rate. The stabilization control algorithm will counteract this roll motion as a function of the roll rate magnitude. The resulting stabilizing steer torque is transferred to the handlebars through the virtual stiffness created by the PD-controller. The rider subsequently receives a feedback torque which counteracts the hand torque applied by the rider. Figure 6-9a shows steer- and handlebar angle of an avoidance manoeuvre during a lane change test at a forward speed of 5 km/h without lateral stability control.

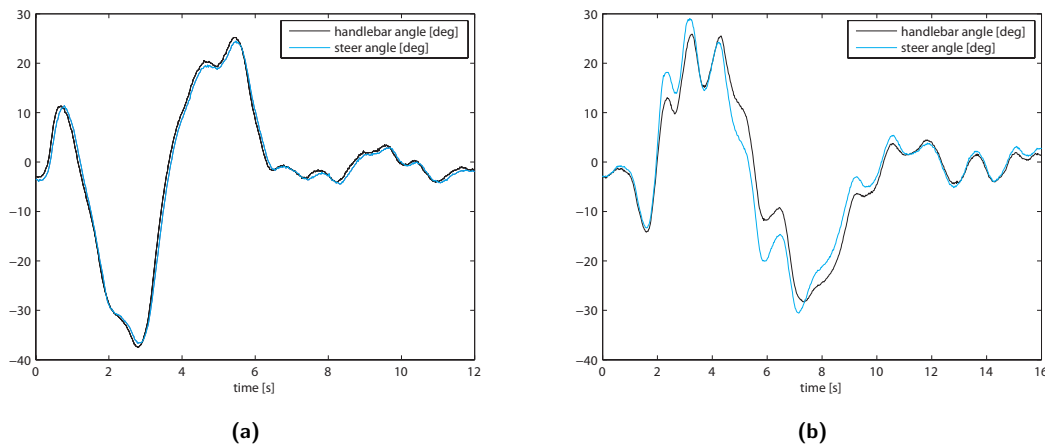


Figure 6-9: The handlebar- and steer angle of the bicycle during an obstacle avoidance manoeuvre without lateral stability control at a forward speed of 5 km/h(a). After the first counter-steer peak the left-right movement shows a satisfactory tracking performance between the handlebar- and steering assembly. An avoidance manoeuvre at an identical forward speed with enabled lateral stability control at $K_s = -5 \text{Ns}^2/\text{rad}$ shows a significant oscillation and angular deviation (b).

The first peak is the counter steer manoeuvre after which the left-right manoeuvre is initiated. After the six seconds mark in the plot the bicycle has finished the avoidance manoeuvre and the steering angle changes to a neutral position. Although a small deviation between the handlebar- and steering angle can be observed, the tracking performance shows a satisfactory steering behavior. Figure 6-9b shows the steer- and handlebar angle of an avoidance manoeuvre during a lane change test at an identical forward speed with enabled lateral stability control at a controller gain of $K_s = 10 \text{Ns}^2/\text{rad}$. In comparison to the avoidance manoeuvre without lateral stability control, the steer- and handlebar angle shows a significant oscillation as the controller tends to counteract the handlebar initiated steer motion. The relatively low stiffness created by the PD-controller allows a significant difference between the handlebar- and steering position. Figure 6-10 shows a matrix of power spectral density plots of each individual obstacle avoidance lane change test. The horizontal axis shows the frequency content of the handlebar rate signal from 0 to 4 Hz whereas the vertical axis shows the magnitude of the handlebar rate signal from 0 to 1500 $(\text{deg/s})^2/\text{Hz}$.

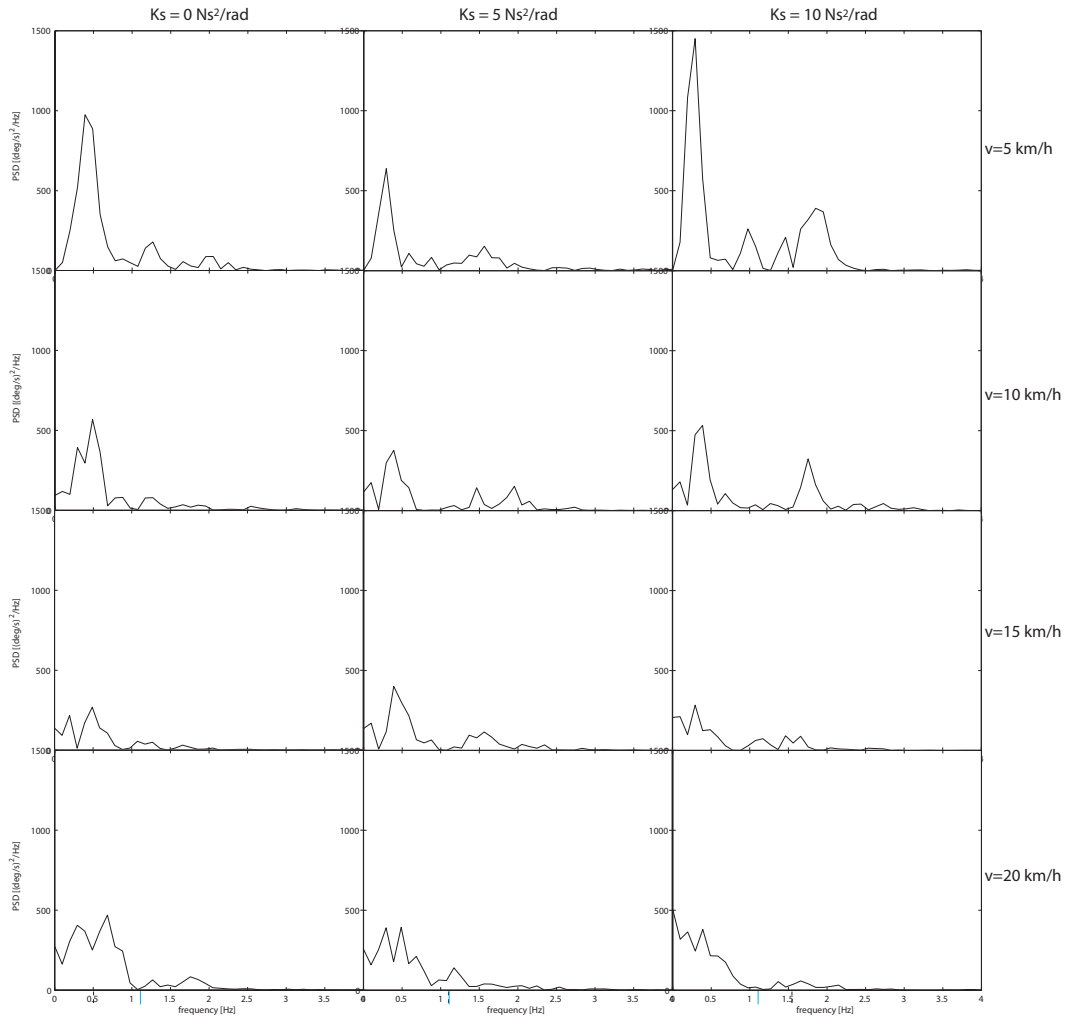


Figure 6-10: Low Speed Stabilization control algorithm test results. Each plot shows the power spectral density (PSD) of the handlebar rate during a single obstacle avoidance manoeuvre at $v=[5,10,15,20]$ km/h and $K_s=[0,5,10]$ Ns^2/rad . At a forward speed of 5 km/h and increasing stabilizing controller action K_s the handlebar motion shows an increase in high frequency content. As the stabilizing controller action reduces with increasing forward speed, the high frequency content in the handlebar motion decreases.

The limited time duration of the handlebar angle signal during a obstacle avoidance manoeuvre as indicated in figure 6-9a, causes a relatively coarse frequency distribution in the power spectral density plots. From the power spectral density plots at a forward speed of 5 km/h an increase in stabilizing controller gain K_s shows in increase in high frequency content above 1 Hz. This corresponds with the observed time signal response in figure 6-9b. At higher forward speeds the high frequency content reduces as the stabilizing controller action reduces linearly with increasing forward speed. From the time signal shown in figure 6-9b and the handlebar rate frequency distribution shown in figure 6-10, it shows that at low forward speeds and high stabilization controller settings the stabilization steer motion is undesirably opposed by the rider input on the handlebars.

An improvement which eliminates the virtual stiffness created by the PD-controller would be to apply the stabilization torque at the handlebar assembly rather than the steering assembly.

This would create a more direct connection to the rider which allows the rider to counteract the stabilizing controller action more effectively during an avoidance manoeuvre.

6-3 Self Stability

The eigenvalue plots shown in figure 6-2b, 6-2c and 6-2d from the hands-free bicycle rider combination predict self-stable lateral behavior with an increasing self-stable forward speed range. Measurements of rider effort during the path following experiments do indeed show a reduced rider steer effort with increasing controller gain. Contradictory to the eigenvalue plot simulations however, experiments with a physical hands-free riding position resulted in a mildly unstable oscillating handlebar assembly well inside the predicted self-stable forward speed range.

The un-modeled actuator-, sensor-, and controller dynamics apparently have a significant effect on the overall lateral stability of the bicycle. During the path following- and obstacle avoidance manoeuvre experiments, the unstable handlebar oscillation was effectively damped by the arms of the rider by the additional mass or stiffness. The mildly unstable free handlebar behavior did not however influence the stabilization algorithm in a normal riding position.

6-4 Summary

This chapter shows the experimental tests conducted with the steer-by-wire bicycle prototype to evaluate the low-speed stabilization control algorithm. A path following experiment and lane change obstacle avoidance manoeuvre test at four different forward speeds as well as four different stabilization gains, show the effect of the lateral stability control algorithm by analyzing the handlebar motion as a measure for rider effort during the individual experiments.

Simulations predict an increasing auto-stable forward speed range with increasing controller gain and should therefore require less rider input to stabilize the bicycle at lower forward speeds. Test results from the path following experiments at low forward speeds agree with this hypothesis, as the power spectral density of the handlebar motion signal reduces with increasing controller gain. An identical experiment without torque feedback at the handlebars does not show a significant reduction in rider-effort with increasing controller gain. This position control strategy however does show that the torque feedback at the handlebars has a positive contribution by decreasing the rider steer effort at low forward speeds.

Test results from the lane change obstacle avoidance manoeuvre experiment show that the stabilizing controller action at the steering assembly, disturbs the rider induced roll motion through the virtual stiffness at the handlebars. The inherently conflicting aspects of a stabilizing controller having to allow for a sudden, unstable avoidance manoeuvre should be more easily overruled by the rider if the stabilizing controller action is provided at the handlebar assembly instead of the steering assembly as during the experiments.

A discrepancy between the eigenvalue plots of the model and the handlebar stability behavior on the steer-by-wire bicycle, show the need for a more accurate model which includes sensor-, actuator- and controller dynamics to more accurately predict the hands free riding behavior.

Conclusions and Recommendations

The following chapter summarizes the conclusions and recommendations to conclude this research. The conclusions in the following section indicate the primary findings of the numerical modeling- and experimental evaluation of the application of a steer-by-wire system on bicycles. The recommendations in the subsequent section gives directions for future research and proposes improvements on the steer-by-wire bicycle prototype.

7-1 Conclusions

This research has shown that a steer-by-wire system on single-track vehicles, or more specifically on a bicycle, allows for new possibilities in terms of vehicle behavior and rider interaction. First, an additional control torque on the steering assembly allows a controller to change the dynamic or lateral behavior based on state information of the bicycle. Second, physical separation of the handlebar and steering assembly allows for more design freedom and a controllable handlebar feedback torque which can change the rider perception significantly.

7-1-1 Vehicle dynamics

Conclusions regarding vehicle dynamics:

- ▷ The ability to apply an additional torque on the steering assembly and the ability to measure the current state of the bicycle, allows a controller to interact and change the dynamic behavior in a way that allows for new possibilities and functionality as indicated by the case studies in the report. The auto-stable forward speed region can be expanded by lowering the weave-speed, requiring less rider-control at low forward speeds to stabilize the lateral motion of the bicycle. A more dramatic change is shown by simulation on the stabilization of a backwards driven bicycle, and a so-called identity transformation by providing a bicycle with a different virtual geometry and its corresponding dynamic behavior.

- ▷ A suboptimal implementation of the roll-angle sensor denied the physical evaluation of the identity transformation algorithms on the steer-by-wire bicycle prototype. The lateral stability enhancement algorithm however, was evaluated during experiments by riding the steer-by-wire bicycle prototype along a predefined track. Off-line analysis on the sensor data stored during the experiments, supported the rider's observation and personal perception that the bicycle was more easy to stabilize and less steer effort was required on the handlebar. More specifically, if one quantifies rider effort as the input applied on the handlebar, the stabilized steer-by-wire bicycle with a controller gain of $K_s=10 \text{Ns}^2/\text{rad}$ is as easy to control at a lowly 5 km/h as compared to an auto-stable bicycle at 20 km/h without lateral stability control. Likewise, the capability of the lateral stability control at 5 km/h is shown by a double reduction in steer effort between a controller gain of $K_s=10 \text{Ns}^2/\text{rad}$ in comparison to a disabled stability control at a gain of $K_s=0 \text{Ns}^2/\text{rad}$.

7-1-2 Bicycle-rider interaction

Conclusions regarding bicycle-rider interaction:

- ▷ Physical separation of the handlebar- and steering assembly makes it able to change the rider's perception by controlling the feedback torque at the handlebar. This also implies the need for a more advanced control strategy in comparison to the virtual PD-controller stiffness, if a comparable steering feel is desired with respect to a conventional steered bicycle. The PD-controller coefficients proposed in the report, yields a satisfactory tracking error of about 1 to 2 degrees on the steering assembly with respect to the handlebar reference input. The static feedback torque at the handlebar however, is scaled down in magnitude in comparison to the actual steer torque to prevent instability issues. Likewise the dynamic steer stiffness in general is lower on the steer-by-wire bicycle prototype in comparison to a conventional steered bicycle. The importance of steer torque feedback is shown by comparison of the steer effort results during the experiments with and without feedback torque at the handlebar. During the experiments without steer torque feedback, the steer effort is about three times higher at a low forward speed of 5 km/h in comparison to an identical experiment with enabled feedback torque. With increasing forward speed at 20 km/h, the steer effort difference factor reduces to just above unity for experiments without feedback torque in comparison to an identical experiment with feedback torque enabled. Visual- and vestibular cues at higher forward speeds presumably become more important for a bicycle rider in comparison to the more dominant proprioceptive cues at lower forward speeds.

7-2 Recommendations

This research has shown insights on the application and the convenience a steer-by-wire system can have on conventional bicycles. The following section proposes recommendations for future research and improvements to the steer-by-wire bicycle prototype.

7-2-1 Vehicle dynamics research

Recommendations regarding future steer-by-wire bicycle vehicle dynamics research:

- ▷ Future research should focus on a robust and accurate roll-sensor design in order to be able to evaluate the proposed pole-placement algorithms. For experimental purposes the proposed complementary filter design can be utilized by replacement of the low-frequency signal content from the accelerometer by a direct optical distance measurement setup. An alternative, physically more elegant and practical approach is to incorporate a more advanced estimation algorithm with the current sensor setup. Subsequent research should quantify the performance and effectiveness of a pole-placement control strategy as proposed by the Virtual Head Angle Bicycle case.
- ▷ Replacement of the current angular rate sensors on the handlebar- and steering assembly with higher bandwidth units, should provide the current dual PD-controller setup with more phase margin. This yield the opportunity to use a higher PD-controller gain at the handlebar assembly positioning control loop, thereby reducing the steer stiffness magnitude difference between the steer-by-wire bicycle and a conventional steered bicycle.

7-2-2 Bicycle-rider interaction research

Recommendations regarding future bicycle-rider interaction research:

- ▷ To provide a more realistic steering feel in comparison to a conventional steered bicycle, the instability of the positioning control loop at the handlebar assembly should be addressed which allows the use of a higher handlebar feedback torque. The Simulink firmware blockset allows for implementation of digital compensation filters, and loop shaping design techniques should be suitable to improve the dynamic response and stability of the handlebar assembly and overall vehicle response.
- ▷ Enabling or disabling the feedback torque at the handlebar as shown during the experiments, indicate the significant contribution of feedback torque for a rider to stabilize the bicycle. It remains unclear however what steer torque magnitude is perceived as optimal. Future research could focus on investigation of an optimal steer stiffness magnitude by experimental evaluation of different levels of steer torque feedback using the steer-by-wire bicycle prototype.

7-2-3 Prototype improvements

Recommendations regarding steer-by-wire bicycle prototype improvements:

- ▷ Safety issues which legally restricts the use of a steer-by-wire system in our current daily transportation becomes highly apprehensible by riding the steer-by-wire bicycle prototype. A relative simple firmware layout as currently applied on the steer-by-wire bicycle prototype is unlikely to cause undesired behavior. A sensor malfunction or

signal wire failure however, is more likely to cause serious injury as no redundancy or fault monitoring system is applied in the current design. A notching, mechanical link between the handlebar- and steering assembly for example, which provides a free, yet limited angular deviation of about 5 to 10 degrees would significantly reduce the chance of personal injury in case of an electronic failure.

- ▷ The current belt drive design on the steering- and handlebar assembly makes use of 6 mm wide polyurethane Synchroflex AT3 timing belts. In case the actuators apply their maximum output torque at an instantaneous peak current of 10 A, the normal force in the timing belts reach their maximum specified limit of 190 N. Combined with the small circumferential contact area between the timing belt and 20-teeth gearwheel on the steering assembly, a design improvement is proposed to reduce teeth deformation by using Synchroflex AT3 timing belts in a 10 mm or 16 mm width. This will provide a more robust mechanical coupling between the actuator and steering assembly.
- ▷ Data storage during the experiments with the steer-by-wire bicycle was conducted by carrying a laptop connected to the serial port of the controller. A more practical approach was examined by onboard data storage with an SD-card directly interfaced to the microcontroller. The Simulink blockset however does not provide native support for mass-storage devices or SD-card interfacing, although a specific Simulink function-block is available to read a separate C-language file which could contain the specific read- and write-functions to communicate with the SD-card. Initial testing using the proposed method did not prove to be successful, as presumably the additional compilation step required by adding a separate C-language file, interferes with the tightly specified routines required to interface an SD-card. It is therefore proposed to implement the read- and write routines using native Simulink function-blocks and SPI-communication which is fully supported by the LK-blockset. Incorporating an onboard data storage solution also allows active sensors which communicate through a serial protocol, to be used on the serial port of the microcontroller.

Bibliography

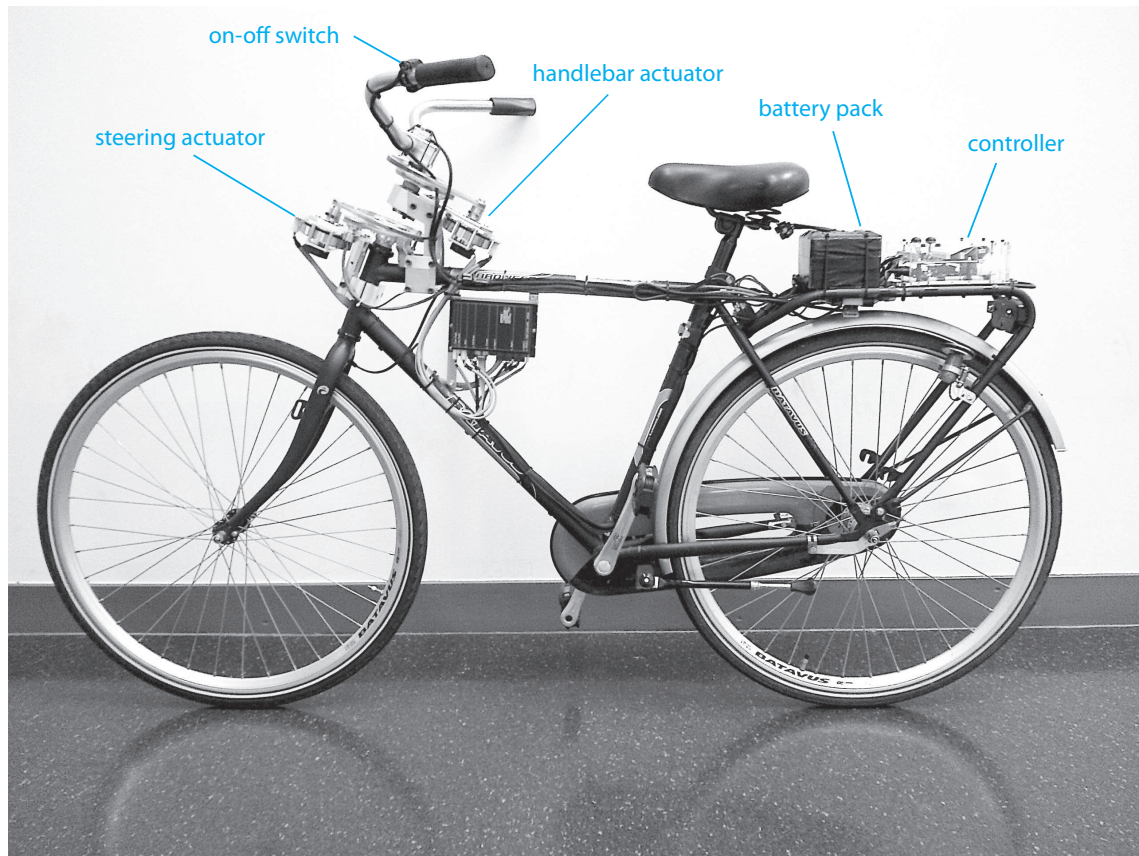
- [Amberkar et al., 2004] Amberkar, S., Bolourchi, F., Demerly, J., and Millsap, S. (2004). A control system methodology for steer by wire systems. In *Steering and Suspension Technology Symposium*, volume 3.
- [Astrom et al., 2005] Astrom, K., Klein, R., and Lennartsson, A. (2005). Bicycle dynamics and control: adapted bicycles for education and research. *Control Systems Magazine, IEEE*, 25(4):26–47.
- [Bertoluzzo et al., 2007] Bertoluzzo, M., Buja, G., and Menis, R. (2007). Control schemes for steer-by-wire systems. *Industrial Electronics Magazine, IEEE*, 1(1):20–27.
- [Boniolo et al., 2008a] Boniolo, I., Norgia, M., Tanelli, M., Svelto, C., and Savaresi, S. (2008a). Performance analysis of an optical distance sensor for roll angle estimation in sport motorcycles. In *IFAC World Congress*, pages 135–140.
- [Boniolo et al., 2008b] Boniolo, I., Tanelli, M., and Savaresi, S. (2008b). Roll angle estimation in two-wheeled vehicles. In *Control Applications, 2008. CCA 2008. IEEE International Conference on*, pages 31–36. IEEE.
- [Gordon, 1966] Gordon, D. A. (1966). Experimental isolation of the driver’s visual input. *Human Factors: The Journal of the Human Factors and Ergonomics Society*, 8-2:129–137.
- [Katagiri et al., 2009] Katagiri, N., Marumo, Y., and Tsunashima, H. (2009). Controller design and evaluation of lane-keeping-assistance system for motorcycles. *Journal of Mechanical Systems for Transportation and Logistics*, 2(1):43–54.
- [Kooijman et al., 2008] Kooijman, J., Schwab, A., and Meijaard, J. (2008). Experimental validation of a model of an uncontrolled bicycle. *Multibody System Dynamics*, 19(1):115–132.
- [Kooijman et al., 2009] Kooijman, J., Schwab, A., and Moore, J. (2009). Some observations on human control of a bicycle. In *Proceedings of the ASME 2009 International Design and Engineering Technical Conferences & Computers and Information in Engineering Conference*.

- [Marumo and Nagai, 2007] Marumo, Y. and Nagai, M. (2007). Steering control of motorcycles using steer-by-wire system. *Vehicle System Dynamics*, 45(5):445–458.
- [Meijaard et al., 2007] Meijaard, J., Papadopoulos, J., Ruina, A., and Schwab, A. (2007). Linearized dynamics equations for the balance and steer of a bicycle: a benchmark and review. *Proceedings of the Royal Society A: Mathematical, Physical and Engineering Science*, 463(2084):1955.
- [Newberry et al., 2007] Newberry, A., Griffin, M., and Dowson, M. (2007). Driver perception of steering feel. *Proceedings of the Institution of Mechanical Engineers, Part D: Journal of Automobile Engineering*, 221(4):405–415.
- [Schmitt et al., 1998] Schmitt, V., Morris, J., and Jenney, G. (1998). *Fly-by-wire: a historical and design perspective*. Society of Automotive Engineers, Warrendale, Pa.
- [Schwab et al., 2008] Schwab, A., Kooijman, J., and Meijaard, J. (2008). Some recent developments in bicycle dynamics and control. In *Fourth European Conference on Structural Control*, page 8.
- [Seidel, 2009] Seidel, F. (2009). X-by-wire. In *Operation Systems, Chemnitz University of Technology, In seminar Transportation Systems*.
- [Seiniger et al., 2011] Seiniger, P., Schroter, K., and Gail, J. (2011). Perspectives for motorcycle stability control systems. *Accident Analysis and Prevention*.
- [Tischler, 1996] Tischler, M. B. (1996). *Advances In Aircraft Flight Control*. CRC Press; 1 edition, page 219.
- [Tomayko, 2000] Tomayko, J. E. (2000). *Computers take flight: A history of NASA's pioneering digital fly-by-wire project*. National Aeronautics and Space Administration, NASA History Office, Washington D.C.
- [van den Ouden, 2011] van den Ouden, J. (2011). Inventory of bicycle motion for the design of a bicycle simulator. Master's thesis, Delft University of Technology - Department of Precision and Microsystems Engineering.
- [Whipple, 1899] Whipple, F. (1899). The stability of the motion of a bicycle. *The Quarterly Journal of Pure and Applied Mathematics*, 30(120):312–348.

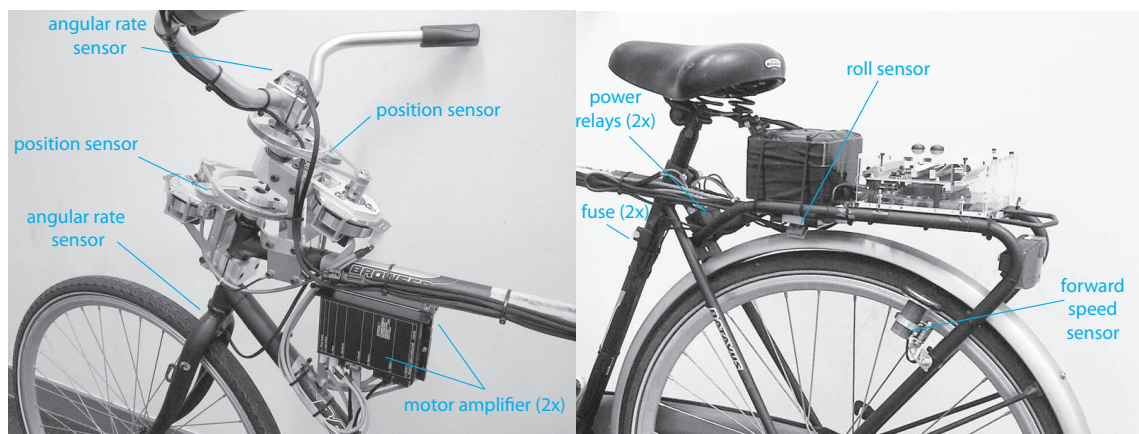
Appendix A

Steer-by-wire bicycle component layout

The physical layout of the steer-by-wire bicycle prototype is shown in figure A. The overview in figure A-1a shows the placement of the main components covered by the steering- and handlebar actuator, battery pack and controller. Figure A-1b shows a more detailed close-up indicating the angular rate- and position sensors on the steering- and handlebar assembly as well as the motor amplifier placement. Figure A-1c shows a close-up of the power relays, electrical fuses, roll- and forward speed sensor placement.



(a)



(b)

(c)

Figure A-1: Steer-by-wire bicycle component layout shows the physical placement of the steering- and handlebar assembly, battery pack and controller (a). A detailed close-up shows the physical placement of the motor amplifiers and sensors (b,c).

Appendix B

Electronic circuit layout

The following sections contain the electronic layout and component selection of the controller IO-board, as well as the layout of the power-wiring and sensor-wiring on the steer-by-wire bicycle prototype.

B-1 IO-board circuit layout

The Microchip Explorer16 microcontroller development board is equipped with an expansion connector which provides direct access to the microcontroller input- and output pins. This low-level hardware approach allows for a low-cost, simple and efficient hardware design, however it requires additional electronic circuitry to suit a more specific application. The IO-board on the steer-by-wire bicycle prototype is physically placed on top of the Explorer16 development board allowing to interface analog sensor signals with the microcontroller. The IO-board contains the required additional electronic circuitry which enables particular functionality. More specifically it will,

- ▷ Interface and scale the magnitude of the sensor signal to be able to interface with the analog-to-digital converter, without exceeding the minimum- and maximum voltage limit of the microcontroller chip.
- ▷ Integrate a digital-to-analog section to convert a digital pulse-width modulated microcontroller signal into an analog output voltage to be able to interface with the motor amplifiers.
- ▷ Incorporating a dedicated fail-safe actuator enable signal by providing a 12V enable signal to the motor amplifiers.
- ▷ Providing visual and audible status indication by utilization of a LED indicator and piëzo buzzer on the IO-board circuit board, as well as the ability to interact with the controller software by push buttons.

Figure B-1 shows the individual component layout on the IO-board. Sensor wiring on the steer-by-wire bicycle prototype is electrically connected to the interface screw-terminals on the IO-board and individually labeled A to T. The individual interface terminal functions are indicated in the figure by a small circular icon and corresponding alphabetical designator. Microcontroller input- or output pins are designated by an arrow-like block in which a corresponding port designator (B,D,F,G) and pin numbering designator (0...11) is shown. Input- or output designators in the Simulink blockset are labeled identically.

Visual status indication

A firmware controllable visual status indication is provided by dual color LED LD1 interfaced to the microcontroller output pins RF7 and RF8 by current limiting resistors R1 and R2.

Audible status indication

A firmware controllable audible status indication is provided by piëzo buzzer SG1. A low supply current of about 10 mA allows for interfacing directly to microcontroller output port RE5 which is specified up to a maximum source current of 20 mA.

Forward speed sensor interface

The voltage signal of the forward speed sensor at interface terminal C is connected to microcontroller input pin RB5. A voltage divider network R13 and R14,R15 attenuates the maximum sensor voltage to a safe voltage level at the microcontroller input pin which is specified up to a maximum of 3.3 V. The sensor voltage is a function of forward speed of the bicycle. As shown in section 5-3-1 the sensor voltage will be maximum at the highest forward speed specified at 10 m/s. The corresponding signal voltage of 10.42 V is attenuated by a factor of 3.35 by the voltage divider network and maximizing resolution on the forward speed measurement. The resolution of the forward speed sensor in combination with a 12 bit analog-to-digital converter is thereby theoretically specified at about 0.0026 m/s. D1 is a schottky diode having a relatively low voltage drop in comparison to conventional silicon diodes of about 0.2 V and protects the microcontroller input if the rear wheel of the bicycle is rotated backwards. The negative voltage of the forward speed sensor will be clamped by the schottky diode which limits the maximum negative voltage at the microcontroller input to -0.2 V within the microcontroller specified safe operating limit of -0.3 V.

Motor amplifier enable circuitry

The enable circuitry is implemented to provide a 12 V output to the motor amplifiers which enables or disables the actuators on the bicycle. The enable circuitry is implemented twofold in order to control the steering- and handlebar assembly motor amplifiers individually.

A high logic-level signal microcontroller output signal is 3.3 V which does not trigger the high signal-level threshold on the motor amplifier which is specified to be equal or higher than 9 V. In order to increase the voltage level output, transistor Q2 is utilized to switch an external

12 V source clamped by pull-down resistor R7. For safety reasons however, the 12 V output provided at interface terminal A of the IO-board should be pulled to ground if no voltage on the microcontroller is present or if the output pin is left floating, which is the case during the initialization phase just after power-up. Utilizing an NPN transistor as a switch also means the signal is inverted which is unfavorable. Subsequently PNP transistor Q1 is placed behind the NPN transistor whose base is connected to the collector of the PNP transistor and pulled high by resistor R5. A 12 V signal on the emitter of the PNP transistor is present only if the microcontroller output pin RG1 is high, otherwise the voltage on interface terminal A is pulled low by resistor R4. Resistors R3 and R6 are sized such that the transistors operate in their saturation region thereby effectively operating as a switch.

The cascaded, dual transistor setup ensures a fail-safe mechanism which disables the operation of the actuators in case the controller has not yet active control over the microcontroller enable pin RG1. An identical circuit is shown which interfaces terminal B by operation of enable pin RG9.

Push button interface

Firmware controllable push buttons S1 and S2 are pulled high by resistors R16 and R17 and interface with the microcontroller input pins RF2 and RF3 respectively.

Negative power supply circuitry

To provide a general opamp the ability to lower their output to ground level, a symmetrical power supply is required to power the DAC circuitry opamps IC2 and IC3. The negative supply voltage is created by a charge pump configuration around IC1 which is a ICL7660S voltage converter chip able to convert a positive supply voltage of 12 V at pin 8 to a negative voltage of about -12 V at pin 5. Electrolytic capacitors C1 and C2 are required for internal operation whereas the cascaded diode configuration limits the supply voltage to factory recommended specifications. The 12 V IO-board supply voltage can however be as high as 13.7 V. The unregulated output voltage of a single battery-cell during charging will be 14.4 V minus a single 0.7 V drop by the Explorer16 input protection diode. The maximum specified supply voltage of the ICL7660S however is 13.0 V therefore two cascaded 1N4007 silicon diodes D2 and D3 lower the maximum supply voltage at pin 8 to about 12.4 V.

DAC circuitry

The motor amplifiers require an analog signal voltage to control the torque to the actuators. The microcontroller however has no build-in digital-to-analog peripheral and therefore has to be included on the IO-board circuit layout. As well as the motor amplifier enable circuitry, the DAC circuitry is implemented in twofold to control the torque requirement to each actuator individually. A passive, double stage RC-filter is utilized to convert the square wave signal from the microcontroller to an analog voltage signal which is buffered by IC2 a low offset, precision opamp LT1006.

The component value selection of the individual filter stages is a critical balance between dynamic response and high frequency signal attenuation. A high signal attenuation with a

typical first- or second order low-pass filter characteristic is achieved by utilizing a as high as possible PWM-frequency. Section 5-2-2 shows that a double first-order filter stage is required to decrease the voltage oscillation at the output to a satisfactory level. The voltage oscillation magnitude has even reduced down to the noise level of about 4 mV. The dynamic response of this double first-order filter stage is characterized by the bandwidth or typical -3 dB response. The utilized double first-order filter setup has a bandwidth specified up to about 1 kHz, well above the sub 10 Hz steer frequency content experienced during bicycle riding.

A double passive low-pass RC-filter is used to filter the PWM-signal by a double resistor-capacitor pair R18,C3 and R19,C4. The 0 V to 3.3 V fixed amplitude, 100 kHz pulse-width modulated frequency signal at pin RD0 is converted by the two first-order analog RC-filters to a discrete analog output voltage ranging from 0 V to 3.3 V with a resolution of 400 steps. The analog voltage at the high impedance, positive opamp input is scaled from 3.3 V to a maximum of 5 V by the gain stage around opamp pin 2 and pin 6 in order to maximize the motor amplifier input range. Resistor network R20 and R21,R22 act as a voltage divider between the low-impedance opamp output and the inverting input in a feedback configuration. The resistor divider network by resistor R20 and R21,R22 set a gain of 1.53 to effectively increase the analog output voltage from a maximum of 3.3 V to 5.0 V.

B-2 Power-wiring layout

The power-wiring layout shown in figure B-2 covers the physical wiring from the battery pack to the controller board and motor amplifiers.

A designated 24V battery pack is based on two individual Super-B 6400E Li-Ion connected in series which provide an effective supply voltage of 26.4 V to the motor amplifiers to power the actuators. A charging connector at each individual battery is provided to charge with a constant voltage source at 14.4 V.

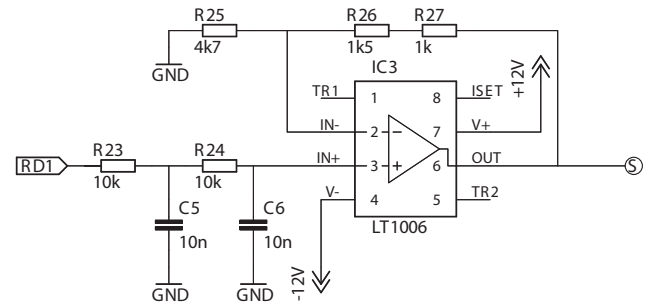
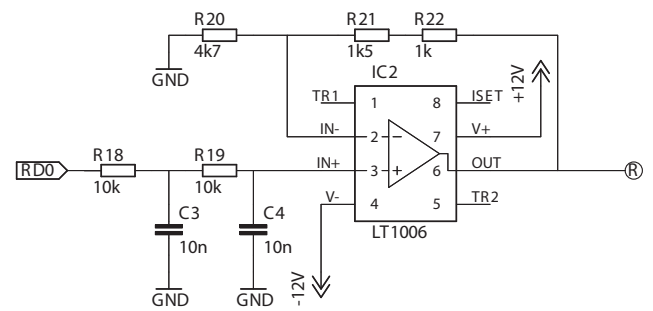
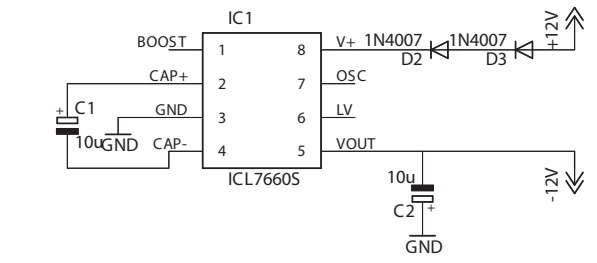
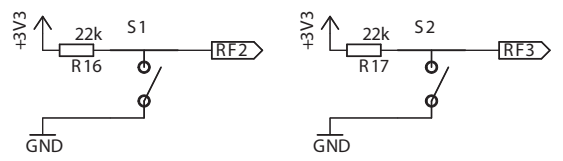
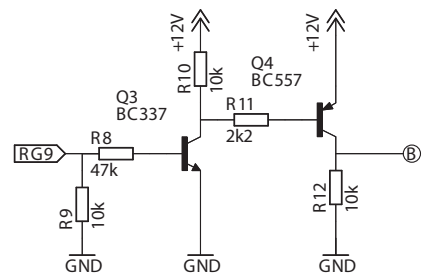
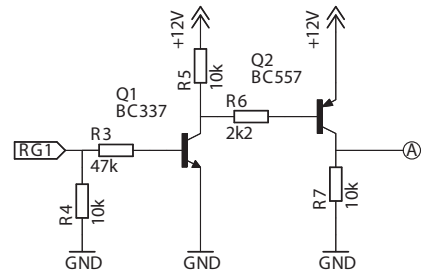
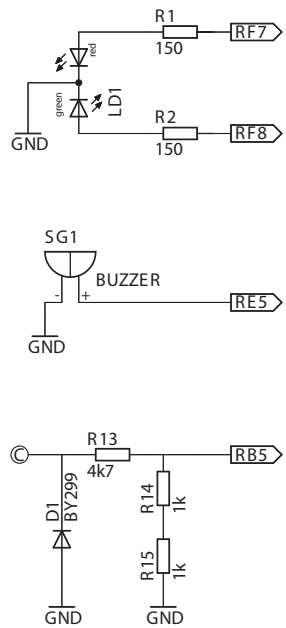
A designated 12V center-connection provide an effective 13.2 V supply voltage to the Explorer16 controller board hardware. An on-off switch located on the handlebars of the steer-by-wire bicycle prototype, actuates two power relays to physically switch the supply power to the motor amplifiers and controller hardware. Reverse-biased diodes D1 and D2 provide protection against switched inductive loads. The motor amplifiers are individually fused by a 10 A slow acting fuse for additional protection. Wiring from the IO-board interface terminals to each individual motor amplifier is color-coded.

The individual Super-B batteries hold a 6400 mAh electric charge. The battery pack consists of two batteries connected in series which yields a nominal capacity of just over 168 Wh. The power consumption by the controller and sensors is negligible in comparison to the power consumption of the actuators. The switching motor amplifier technology however provides a highly efficient energy conversion. If the handlebar- and steering actuators will be actuated continuously at their nominal current and low rotational speeds, which is a highly exaggerated assumption, the total power consumption by the actuators and motor amplifiers will be about 20 W. A rough estimate therefore yields a battery life of about 8 hours. In practise the batteries will not have a perfectly flat discharge curve and the power consumption of the actuators highly depend on the torque request and steering motions required. The battery capacity however is sufficient to provide a useable time-span for testing purposes.

B-3 Sensor-wiring layout

The sensor-wiring shown in figure B-3 covers the physical wiring from the individual sensors to the IO-board controller interface terminals. The steering- and handlebar rate sensor wiring however shows an in-line voltage divider resistor network R3,R4,R5 and R6,R7,R8 to scale the 5 V output of the angular rate sensors to a maximum of 3.3 V to satisfy the microcontroller analog-to-digital input voltage limitations. A voltage divider R9,R10 at the power input socket of the Explorer16 development board allows to measure the battery voltage of a single battery-cell. By monitoring the battery voltage of a single cell, the controller firmware can alert the rider if the battery voltage has dropped below a critical value which no longer allows a safe operation of the steer-by-wire bicycle.

Figure B-1: IO-board circuit layout.

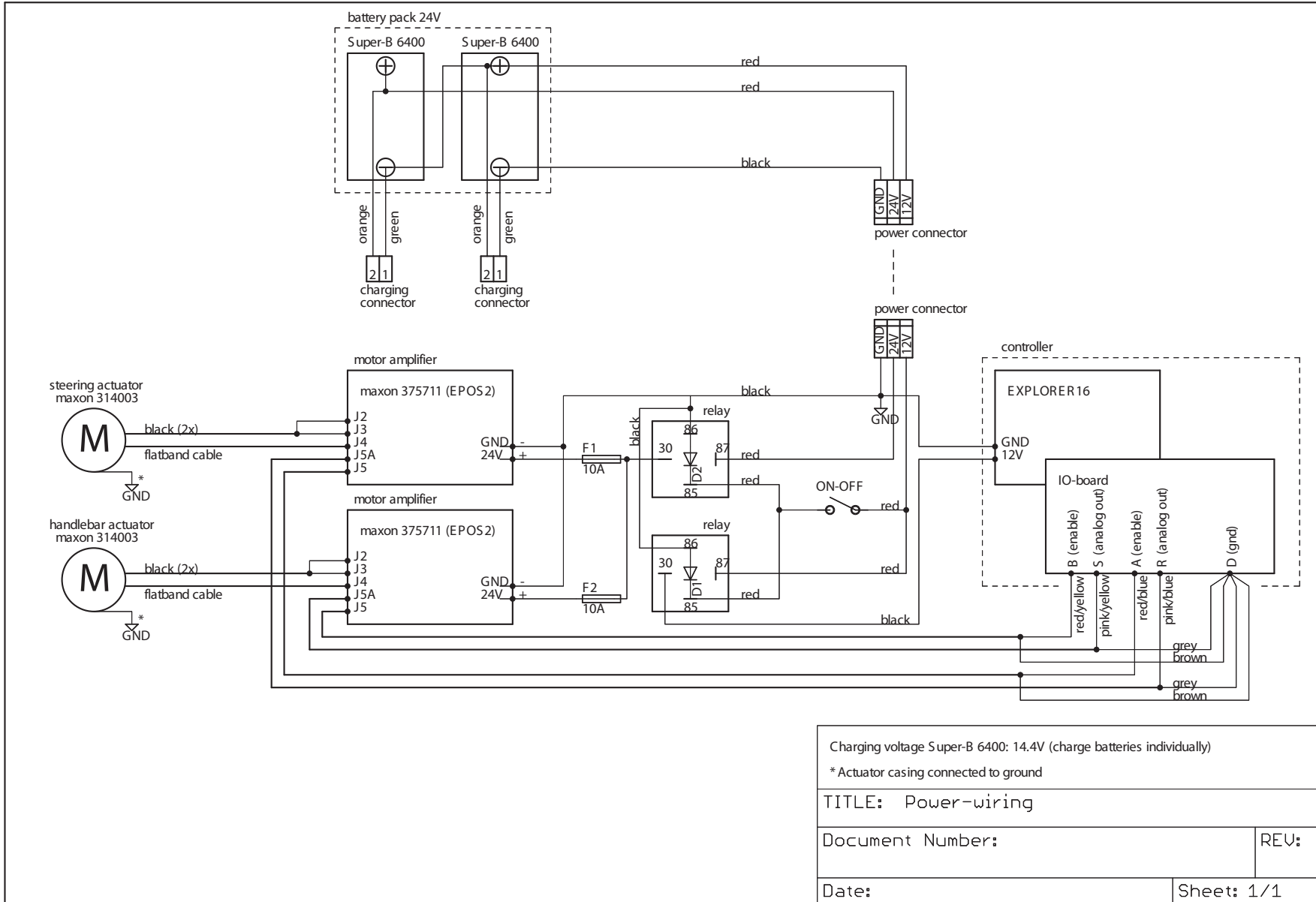


- IO-BOARD TERMINAL PINOUT
- (A) = ENABLE HANDLEBAR ACTUATOR [RG1]
 - (B) = ENABLE STEERING ACTUATOR [RG9]
 - (C) = FORWARD SPEED SENSOR [RB5]
 - (D) = GROUND
 - (E) = GROUND
 - (F) = +3.3V SUPPLY
 - (G) = STEERING POSITION SENSOR [RB1]
 - (H) = HANDLEBAR POSITION SENSOR [RB2]
 - (I) = +3.3V SUPPLY
 - (J) = ROLL SENSOR ACCELERATION X [RB3]
 - (K) = ROLL SENSOR ACCELERATION Z [RB8]
 - (L) = ROLL SENSOR GYRO [RB9]
 - (M) = GROUND
 - (N) = +5V SUPPLY
 - (O) = HANDLEBAR RATE [RB10]
 - (P) = STEERING RATE [RB11]
 - (Q) = GROUND
 - (R) = DAC STEERING ACTUATOR [RD0]
 - (S) = DAC HANDLEBAR ACTUATOR [RD1]
 - (T) = BATTERY VOLTAGE [RB4]

- (C) ——— RB1
- (H) ——— RB2
- (J) ——— RB3
- (K) ——— RB8
- (L) ——— RB9
- (O) ——— RB10
- (P) ——— RB11

	IO-BOARD INPUT TERMINAL
	MICROCONTROLLER INPUT PORT
	MICROCONTROLLER OUTPUT PORT
TITLE: IO-board	
Document Number:	REV:
Date:	Sheet: 1/1

Figure B-2: Power wiring layout.



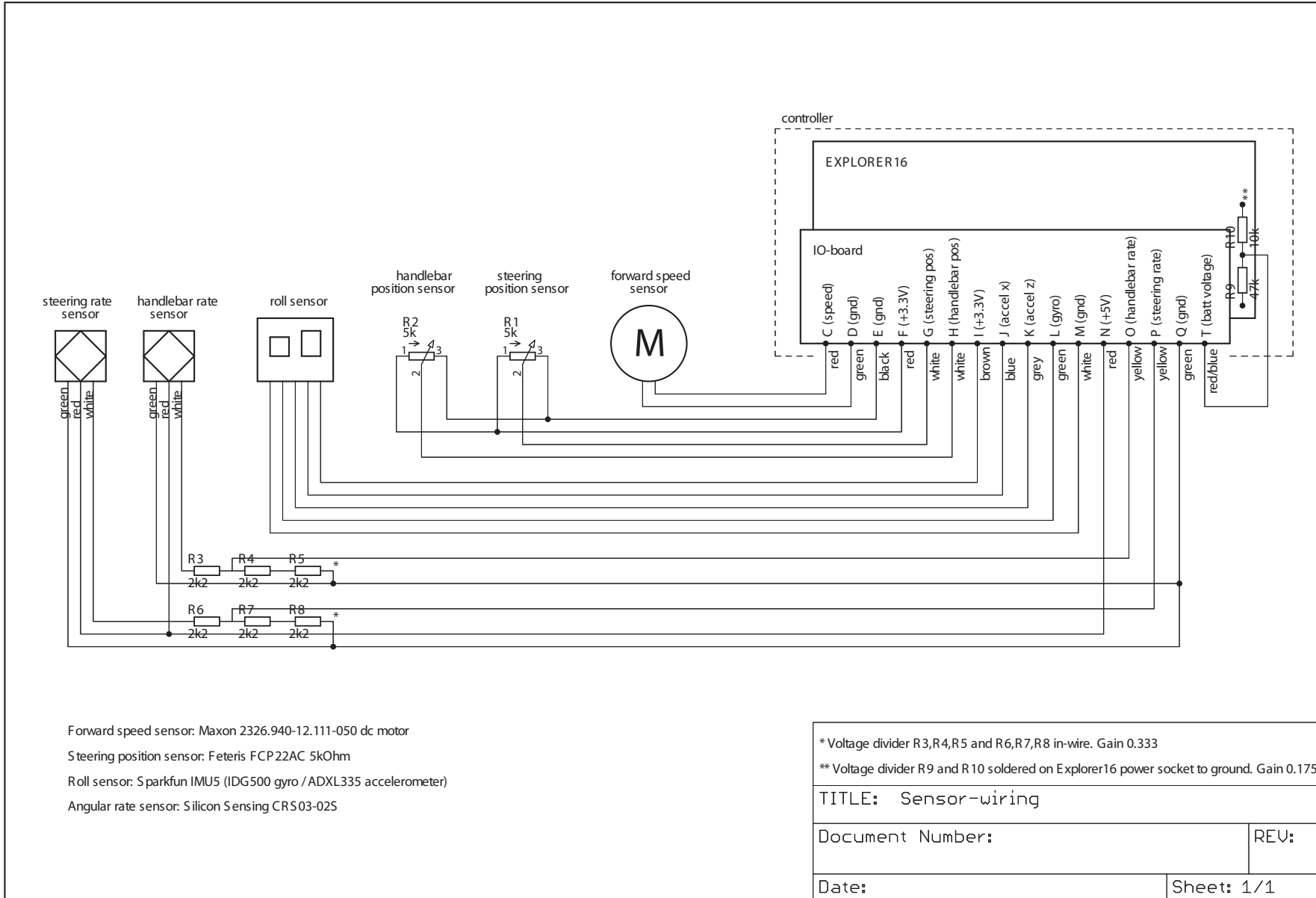


Figure B-3: Sensor wiring layout.

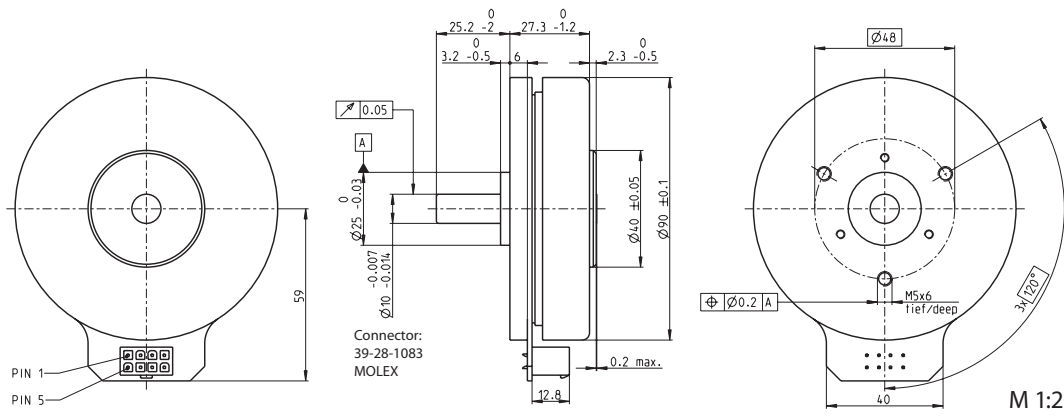
Appendix C

Component specifications

The following appendix shows specifications of the following items:

1. Steering- and handlebar actuator figure C-1
2. Motor amplifier figure C-2
3. Steering- and handlebar potentiometer figure C-3
4. Steering- and handlebar angular rate sensor figure C-4
5. Forward speed sensor figure C-5
6. Roll sensor accelerometer figure C-6
7. Roll sensor rate gyro figure C-7

EC 90 flat Ø90 mm, brushless, 90 Watt

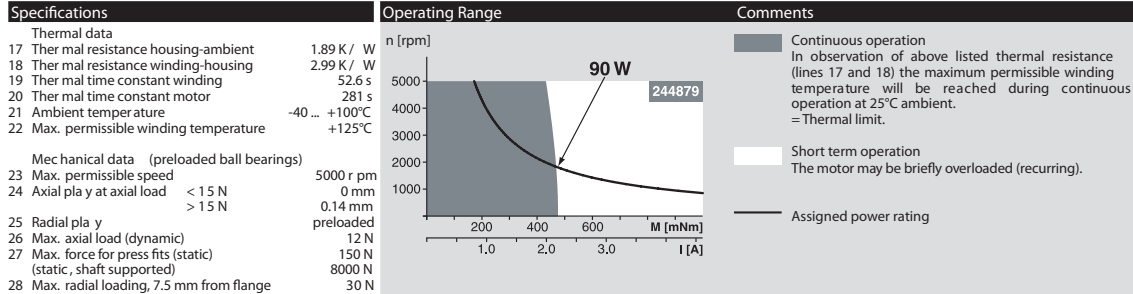


maxon flat motor

Stock program
Standard program
Special program (on request)

Order Number	
with Hall sensors	314003

Motor Data	
Values at nominal voltage	
1 Nominal voltage	V 48.0
2 No load speed	rpm 2080
3 No load current	mA 130
4 Nominal speed	rpm 1640
5 Nominal torque (max. continuous torque)	mNm 494
6 Nominal current (max. continuous current)	A 2.12
7 Stall torque	mNm 4530
8 Starting current	A 20.9
9 Max. efficiency	% 85
Characteristics	
10 Terminal resistance phase to phase	Ω 2.30
11 Terminal inductance phase to phase	mH 2.50
12 Torque constant	mNm / A 217
13 Speed constant	rpm / V 44.0
14 Speed / torque gradient	rpm / mNm 0.466
15 Mechanical time constant	ms 14.9
16 Rotor inertia	gcm ² 3060



maxon Modular System		Overview on page 16 - 21
29 Number of pole pairs	12	
30 Number of phases	3	
31 Weight of motor	600 g	Planetary Gearhead Ø52 mm 4 - 30 Nm Page 241
Values listed in the table are nominal.		
Connection Pin 1 Hall sensor 1 Pin 2 Hall sensor 2 Pin 3 4.5 ... 18VDC Pin 4 Motor winding 3 Pin 5 Hall sensor 3 Pin 6 GND Pin 7 Motor winding 1 Pin 8 Motor winding 2 Wiring diagram for Hall sensors see p.29		
Cable Connection cable Universal, L = 500 mm 339380 Connection cable to EPOS, L = 500 mm 354045		
Recommended Electronics: DECS 50/5 Page 289 DEC 50/5 291 DEC Module 50/5 291 DECV 50/5 297 DEC 70/10 297 EPOS2 24/5 305 EPOS2 70/10 305 EPOS2 P 24/5 308 Notes 20		

Figure C-1: Maxon EC90 brushless 90W actuator.

CANopen USB RS232 GUI



EPOS2 24/5
Matched with DC brush motors with encoder or brushless EC motors with Hall sensors and encoder, from 5 to 120 watts.



EPOS2 50/5
Matched with DC brush motors with encoder or brushless EC motors with Hall sensors and encoder, from 5 to 250 watts.



EPOS2 70/10
Matched with DC brush motors with encoder or brushless EC motors with Hall sensors or encoder, from 80 to 700 watts.

maxon motor control

Controller versions		
Slave version	Slave version	Slave version
Electrical Data		
11 - 24 VDC	11 - 50 VDC	11 - 70 VDC
11 - 24 VDC	11 - 50 VDC	11 - 70 VDC
0.9 x V _{cc}	0.9 x V _{cc}	0.9 x V _{cc}
10 A	10 A	25 A
5 A	5 A	10 A
50 kHz	50 kHz	50 kHz
10 kHz	10 kHz	10 kHz
1 kHz	1 kHz	1 kHz
1 kHz	1 kHz	1 kHz
25 000 rpm (sinusoidal); 100 000 rpm (block)	25 000 rpm (sinusoidal); 100 000 rpm (block)	25 000 rpm (sinusoidal); 100 000 rpm (block)
15 μH / 5 A	22 μH / 5 A	25 μH / 10 A
Input		
H1, H2, H3	H1, H2, H3	H1, H2, H3
A, A _v , B, B _v , I, I _v (max. 5 MHz)	A, A _v , B, B _v , I, I _v (max. 5 MHz)	A, A _v , B, B _v , I, I _v (max. 5 MHz)
6 digital inputs	11 digital inputs	10 digital inputs
2 analog inputs	2 analog inputs (differential)	2 analog inputs (differential)
12-bit resolution, 0 ... +5 V	12-bit resolution, ±10 V	12-bit resolution, 0 ... +5 V
configurable with DIP switch 1 ... 7	configurable with DIP switch 1 ... 7	configurable with DIP switch 1 ... 7
Output		
4 digital outputs	5 digital outputs; 1 analog 12-bit 0 ... 10 V	5 digital outputs
+5 VDC, max. 100 mA	+5 VDC, max. 100 mA	+5 VDC, max. 100 mA
+5 VDC, max. 30 mA	+5 VDC, max. 30 mA	+5 VDC, max. 30 mA
V _{cc} , max. 1300 mA	+5 VDC, max. 150 mA	+5 VDC, max. 150 mA; +5 VDC (R _{th(j-c)} = 1 k Ω)
Interface		
RxD;TxD (max. 115 200 bit/s)	RxD;TxD (max. 115 200 bit/s)	RxD;TxD (max. 115 200 bit/s)
high; low (max. 1 Mbit/s)	high; low (max. 1 Mbit/s)	high; low (max. 1 Mbit/s)
Data+; Data- (max. 12 Mbit/s)	Data+; Data- (max. 12 Mbit/s)	Data+; Data- (max. 12 Mbit/s)
Indicator		
green LED, red LED	green LED, red LED	green LED, red LED
Ambient temperature and humidity range		
-10 ... +45°C	-10 ... +45°C	-10 ... +45°C
-40 ... +85°C	-40 ... +85°C	-40 ... +85°C
20 ... 80 %	20 ... 80 %	20 ... 80 %
Mechanical data		
Approx. 170 g	Approx. 240 g	Approx. 330 g
105 x 83 x 24 mm	120 x 93.5 x 27 mm	150 x 93 x 27 mm
Flange for M3-screws	Flange for M3-screws	Flange for M3-screws
Order Number		
367676 EPOS2 24/5	347717 EPO S2 50/5	375711 EPOS2 70/10

Accessories		
309687 DSR 50/5 Shunt regulator	309687 DSR 50/5 Shunt regulator	235811 DSR 70/30 Shunt regulator
Order accessories separately, see page 310	Order accessories separately, see page 310	Order accessories separately, see page 310

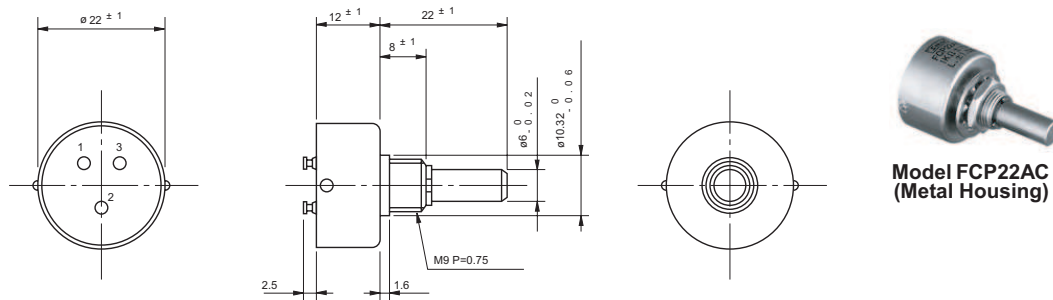
Figure C-2: Maxon EPOS2 70/10 motor amplifier.

Force, Load | Strain gauges | Civil engineering | Torque | Linear Displacement | Position | Inclination, Tilt | Pressure | Angular rate | Acceleration | Vibration | IR Temperature
 Rotary angle | Encoders | Precision Potentiometers | Heavy-duty Joysticks | Foot pedals | Trackballs | Signal conditioning | Process converters | Displays | Data loggers

FCP22AC

Conductive plastic (Busingmount) Low cost item

■ Standard dimensions



- Note: 1. 1pc. Each inner teeth washer and hex nut are attached.
 2. Please process the mounting hole on the panel to be mounted with this potentiometer by the diameter of 10.32mm

■ General Specifications

Standard

Resistance Values: 1k, 2k, 5k, 10 k (Ω)

Special Practical

Resistance Values: 500, 20k, 50k, 100k (Ω)

Total Resistance

Tolerance: Standard Class ±15% (L)
 Precision Class ±10% (K)

Independent

Linearity Tolerance: Standard Class ±1.5%
 Precision Class ±1.0%

Resolution:

Essentially infinite

Output Smoothness:

Within 0.1% against input voltage

Contact Resistance

Variation: Within 2% C.R.V.

Power Rating:

1.0W

Electrical Travel:

320° ±5°

Mechanical Travel:

360° (Endless)

Insulation Resistance:

Over 1,000MΩ at 500 V.D.C

Dielectric Strength:

1 minute at 500 V.A.C.

Starting Torque:

Within 5mN·m (50gf·cm)

Resistance

Temperature

Coefficient: ±400p.p.m./°C

Mass:

Approx. 30g

■ Special Specifications Available

Extra taps (available up to 1 tap), shaft with front and rear extension (rear shaft with 3mm dia. and 20mm length), with stopper (rotating angle becomes 320° and stopper strength is 0.9N·m [9kgf·cm]), special electrical travel, shaft dia. (ø6.35mm) bushing with inch dimensions, special machining on the shaft.

ALTHERIS bv

Scheveningseweg 15
 2517 KS DEN HAAG
 The Netherlands

+31 (0)70 3924421

+31 (0)70 3644249

Offices in : Benelux | Germany | France | UK | Italy | USA

www.altheris.com

sales@altheris.nl

LEADERS IN SENSORS & HEAVY DUTY JOYSTICKS

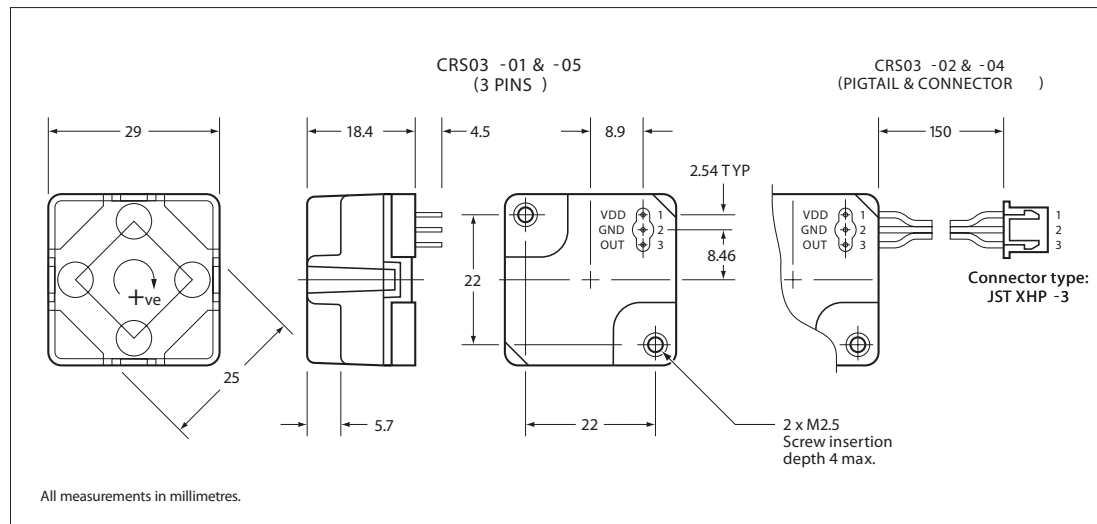
ALTHERIS
 SENSORS & CONTROLS

06/07/2011

Figure C-3: Altheris 5 kΩ FCP22AC potentiometer.

CRS03

Angular Rate Sensor



Typical Data

	-01S & -02S	-04S	-05S
Angular Rate Range	$\pm 100^\circ/s$	$\pm 200^\circ/s$	$\pm 80^\circ/s$
Output	Analogue voltage (ratiometric)		
Scale Factor			
Nominal	20mV/ $^\circ/s$	10mV/ $^\circ/s$	25mV/ $^\circ/s$
Variation over temperature range	< $\pm 3\%$		
Nonlinearity	< $\pm 0.5\%$ of full scale		
Bias			
Setting tolerance	< $\pm 3^\circ/s$	< $\pm 6^\circ/s$	< $\pm 4^\circ/s$
Variation over temperature range	< $\pm 3^\circ/s$	< $\pm 6^\circ/s$	< $\pm 4^\circ/s$
Ratiometric error	< $\pm 1^\circ/s$	< $\pm 2^\circ/s$	< $\pm 0.8^\circ/s$
Drift vs. time	< $\pm 0.55^\circ/s$ in any 30s period (after start-up time)		
g sensitivity	< $\pm 0.1^\circ/s/g$ on any axis		
Bandwidth	10Hz (-3dB)		
Quiescent Noise	< 1mV rms (3Hz to 10Hz)		
Environment			
Temperature	-40°C to +85°C		
Linear acceleration	< 100g		
Shock	200g (1ms, 1 sine)		
Vibration	2g rms (20Hz to 2kHz, random)		
Cross-axis sensitivity	< 5%		
Mass	< 18 gram		
Electrical			
Supply voltage	+4.75V to +5.25V		
Supply current	< 35mA (steady state)		
Noise and ripple	< 15mV rms (DC to 100Hz)		
Start-up time	< 0.2s		
RoHS Compliant	Yes (R & S suffix)		

Pin Connections

1	+5V
2	0V
3	Rate Output

Silicon Sensing Systems Limited
Clifford Road Southway
Plymouth Devon
PL6 6DE United Kingdom
T: +44 (0)1752 723330
F: +44 (0)1752 723331
E: sales@siliconsensing.com
W: siliconsensing.com

Silicon Sensing Systems Japan Limited
1-10 Fuso-Cho
Amagasaki
Hyogo 6600891 Japan
T: +81 (0)6 6489 5868
F: +81 (0)6 6489 5919
E: sssj@spp.co.jp
W: siliconsensing.com

Specification subject to change without notice.

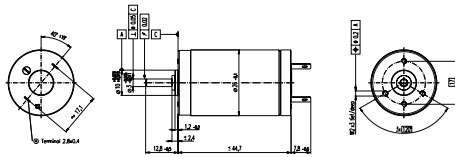

© Copyright 2009
Silicon Sensing Systems Limited
All rights reserved.
Printed in England 02/09

Silicon Sensing Systems Limited Registered in England and Wales No. 3635234 Clifford Road, Southway, Plymouth, Devon PL6 6DE
The device mark Silicon Sensing is a registered trade mark of Silicon Sensing Systems Community Trade Mark 003587664

CRS03-00-0100-131 Rev 2
DCR No. 616971

Figure C-4: Silicon Sensing CRS03-02S angular rate sensor.

Motore S 2326....-12.111-050,

Spazzole in metalli preziosi, 4 Watt, approvato 

- Gioco assiale 0.05 - 0.15 mm
 - Bronzine sinterizzate
 - Carico massimo dei cuscinetti assiale (dinamico) 1.0 N
 - radiale (5 mm dalla flangia) 4.3 N
 - Forza di calettamento (statica) 100 N
 - Gioco radiale 0.020 mm
 - Temp. ambiente -20 ... +65°C
 - Temp. max. del rotore +85°C
 - No. dei segmenti del collettore 11
 - Peso 107 g
- Può essere combinato con GS 30 (p. 194)
 Alcune versioni possono essere fornite da stock; altrimenti prodotto su richiesta con quantitativi minimi.

Codice prodotto	Tensione nominale [Volt]	Velocità a vuoto [rpm]	Corrente a vuoto [mA]	Coppia di stallo [mNm]	Coppia continua max. [mNm]	Gradiente velocità / coppia [rpm / mNm]	Costante di velocità [rpm / V]	Costante di coppia [mNm / A]	Costante di tempo meccanica [ms]	Inerzia del rotore [gcm ²]	Resistenza ai terminali [Ohm]
2326.930-12.111-050	3.0	5380	62	9.2	7.92	163	310	28	8	0.7	0.477
2326.932-12.111-050	3.6	5590	64	9.4	8.12	191	170	08	8	0.95	0.739
2326.933-12.111-050	4.5	5926	67	9.5	8.8	182	130	19	8	1.22	0.984
2326.934-12.111-050	6.0	6410	40	9.6	11.5	182	980	85	17	0.6	1.49
2326.940-12.111-050	6.0	6390	11	9.9	11.1	185	80	05	7	0.7	2.16
2326.936-12.111-050	7.2	4920	23	9.9	11.6	179	61	3.8	17	0.6	3.57
2326.937-12.111-050	9.0	5120	19	9.3	11.4	183	76	6.6	17	3	5.27
2326.938-12.111-050	12.0	5540	16	9.0	11.3	187	47	0.5	17	62	8.19
2326.945-12.111-050	12.0	5390	16	9.4	10.8	207	55	1.0	17	85	9.57
2326.939-12.111-050	15.0	5460	13	9.7	11.2	192	67	6.0	17	40	13.6
2326.946-12.111-050	18.0	6030	12	9.8	10.8	205	39	8.2	17	91	17.1
2326.940-12.111-050	18.0	5300	10	27.5	11.1	195	298	32.1	17	8.28	21.0
2326.941-12.111-050	24.0	5940	9	9.5	10.8	204	30	9.2	17	9	31.0
2326.942-12.111-050	30.0	6020	7	9.4	10.7	207	93	17.0	17	8	48.0
2326.949-12.111-050	42.0	5680	5	9.4	10.5	218	47	8.7	17	4	111

Figure C-5: Maxon 2326.940-12.111-050 brushed dc-motor.



Small, Low Power, 3-Axis $\pm 3g$ Accelerometer

ADXL335

FEATURES

3-axis sensing

Small, low profile package

4 mm \times 4 mm \times 1.45 mm LFCSP

Low power : 350 μ A (typical)

Single-supply operation: 1.8 V to 3.6 V

10,000 g shock survival

Excellent temperature stability

BW adjustment with a single capacitor per axis

RoHS/WEEE lead-free compliant

APPLICATIONS

Cost sensitive, low power, motion- and tilt-sensing

applications

Mobile devices

Gaming systems

Disk drive protection

Image stabilization

Sports and health devices

GENERAL DESCRIPTION

The ADXL335 is a small, thin, low power, complete 3-axis accelerometer with signal conditioned voltage outputs. The product measures acceleration with a minimum full-scale range of $\pm 3g$. It can measure the static acceleration of gravity in tilt-sensing applications, as well as dynamic acceleration resulting from motion, shock, or vibration.

The user selects the bandwidth of the accelerometer using the C_x , C_y , and C_z capacitors at the X_{OUT} , Y_{OUT} , and Z_{OUT} pins. Bandwidths can be selected to suit the application, with a range of 0.5 Hz to 1600 Hz for the X and Y axes, and a range of 0.5 Hz to 550 Hz for the Z axis.

The ADXL335 is available in a small, low profile, 4 mm \times 4 mm \times 1.45 mm, 16-lead, plastic lead frame chip scale package (LFCSP_LQ).

FUNCTIONAL BLOCK DIAGRAM

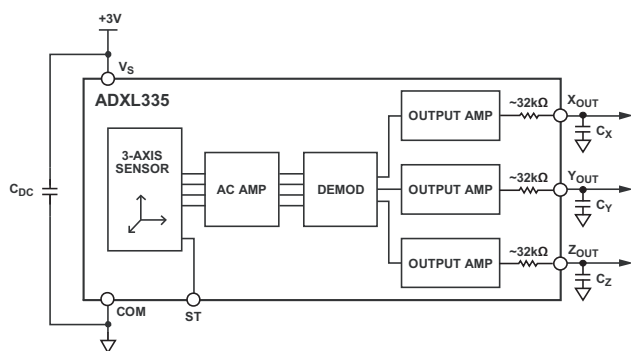


Figure 1.

Rev. 0

Information furnished by Analog Devices is believed to be accurate and reliable. However, no responsibility is assumed by Analog Devices for its use, nor for any infringements of patents or other rights of third parties that may result from its use. Specifications subject to change without notice. No license is granted by implication or otherwise under any patent or patent rights of Analog Devices. Trademarks and registered trademarks are the property of their respective owners.

One Technology Way, P.O. Box 9106, Norwood, MA 02062-9106, U.S.A.
Tel: 781.329.4700 www.analog.com
Fax: 781.461.3113 ©2009 Analog Devices, Inc. All rights reserved.

Figure C-6: Roll sensor accelerometer Analog Devices ADXL335.

InvenSense

Integrated Dual-Axis Gyro

IDG-500

FEATURES

- Integrated X- and Y-axis gyros on a single chip
- Two separate outputs per axis for standard and high sensitivity:
 - X-/Y-Out Pins: 500°/s full scale range
2.0mV/°/s sensitivity
 - X/Y4.5Out Pins: 110°/s full scale range
9.1mV/°/s sensitivity
- Integrated amplifiers and low-pass filters
- Auto-Zero function
- On-chip temperature sensor
- High vibration rejection over a wide frequency range
- High cross-axis isolation by proprietary MEMS design
- 3V single-supply operation
- Hermetically sealed for temp and humidity resistance
- 10,000 g shock tolerant
- Smallest dual axis gyro package at 4 x 5 x 1.2mm
- RoHS and Green Compliant

APPLICATIONS

- General Motion Sensing
- Vehicle Motion Analysis
- Platform Stabilization
- Inertial Measurement Units

GENERAL DESCRIPTION

The IDG-500 is an integrated dual-axis angular rate sensor (gyroscope). It uses InvenSense's proprietary and patented MEMS technology with vertically driven, vibrating masses to make a functionally complete, low-cost, dual-axis angular rate sensor. All required electronics are integrated onto a single chip with the sensor.

The IDG-500 gyro uses two sensor elements with novel vibrating dual-mass bulk silicon configurations that sense the rate of rotation about the X- and Y-axis (in-plane sensing). This results in a unique, integrated dual-axis gyro with guaranteed-by-design vibration rejection and high cross-axis isolation. It is specifically designed for demanding consumer applications requiring low cost, small size and high performance.

The IDG-500 gyro includes the integrated electronics necessary for application-ready functionality. It incorporates X- and Y-axis low-pass filters and an EEPROM for on-chip factory calibration of the sensor. Factory trimmed scale factors eliminate the need for external active components and end-user calibration. This product is lead-free and Green Compliant.

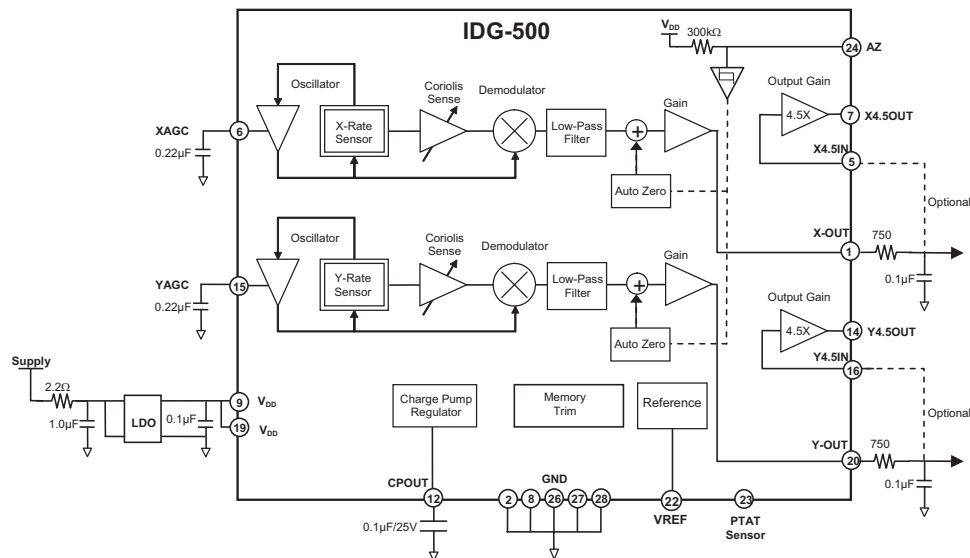


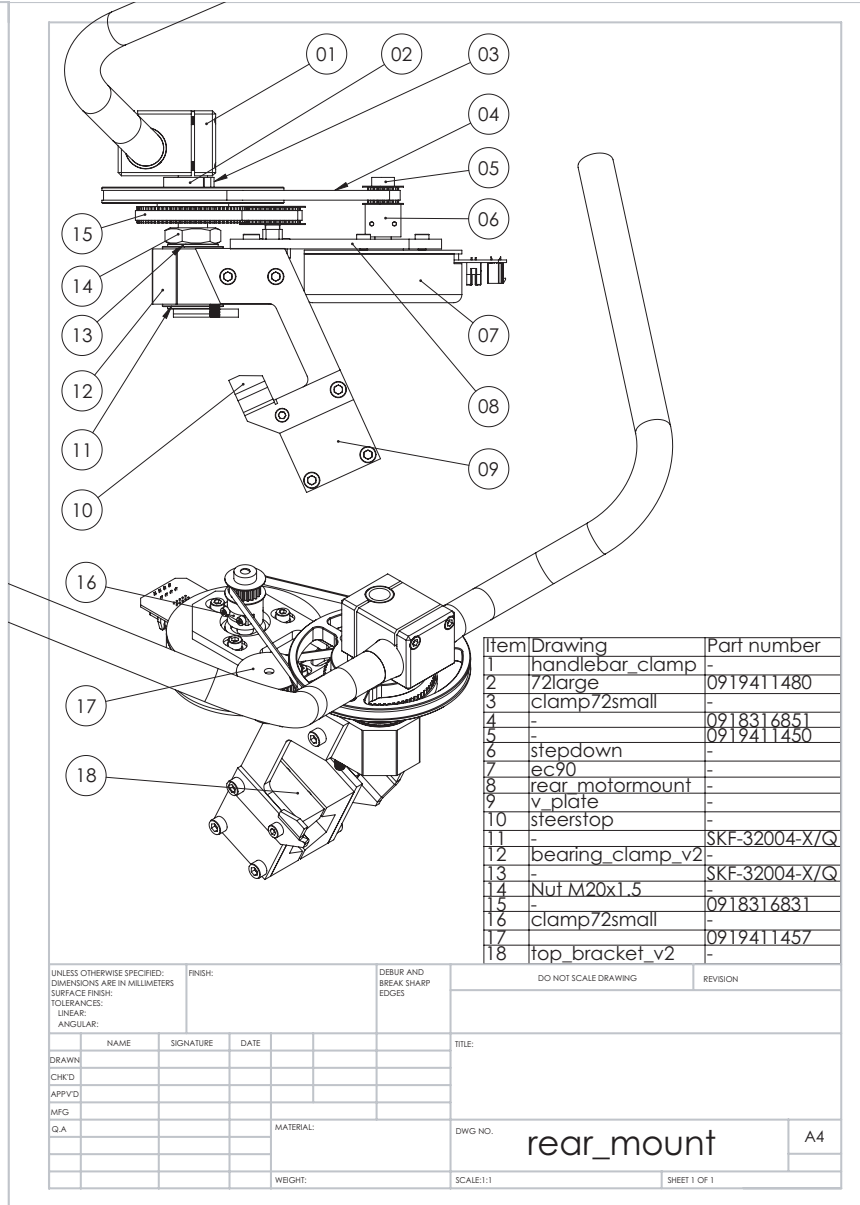
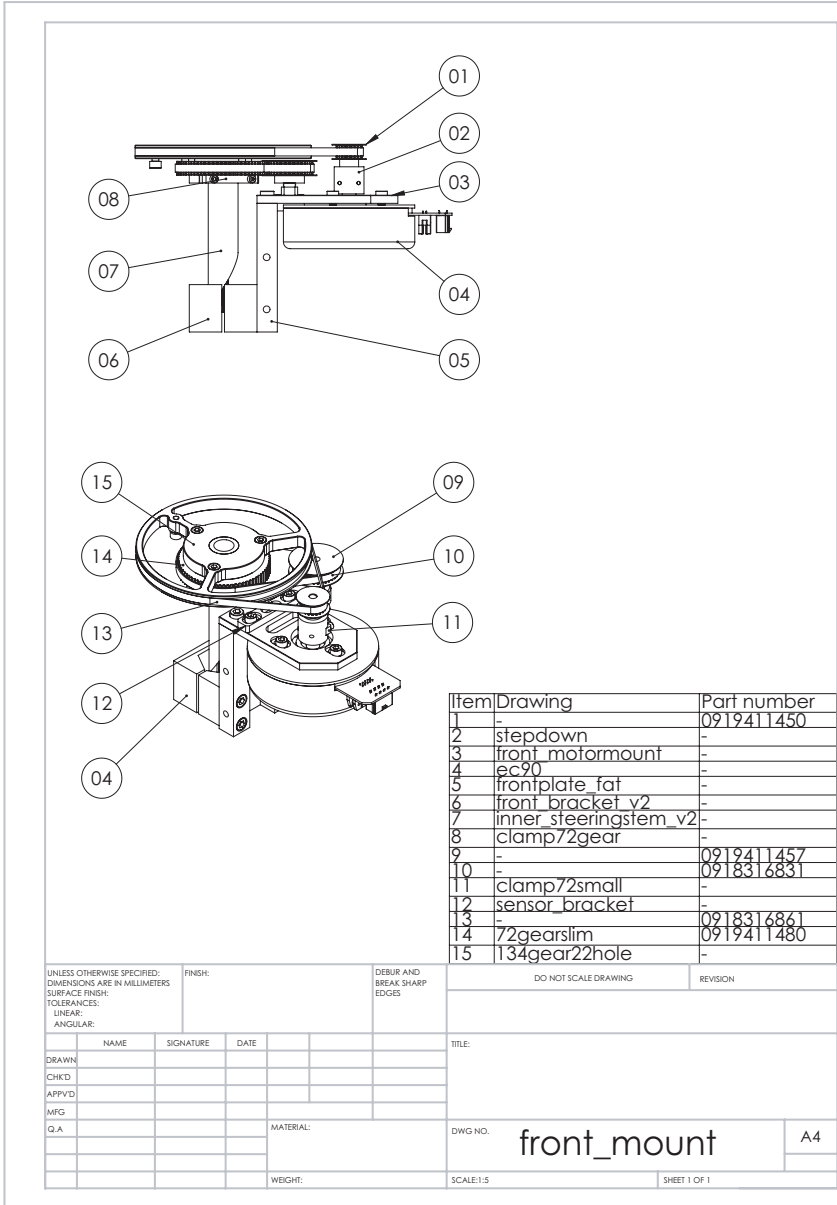
Figure C-7: Roll sensor rate gyro InvenSense IDG500.

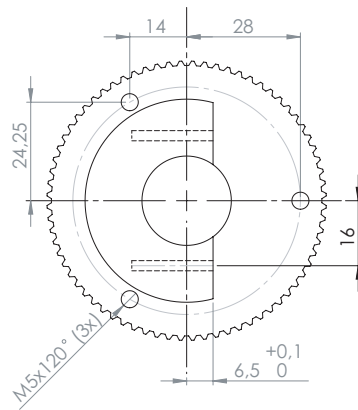
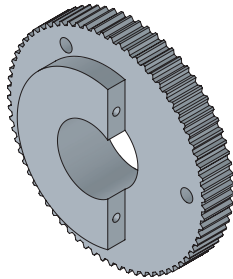
Appendix D

CAD drawings

The following appendix shows individual CAD drawings of the steering- and handlebar assembly hardware. A composition drawing in figure D-1 shows the steering- and handlebar assembly. Individual parts are indicated in the table overview as well as part numbers for timing belt components provided by Angst+Pfister. Note that fasteners are not individually indicated in the CAD drawings.

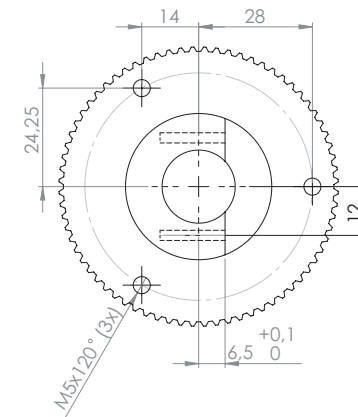
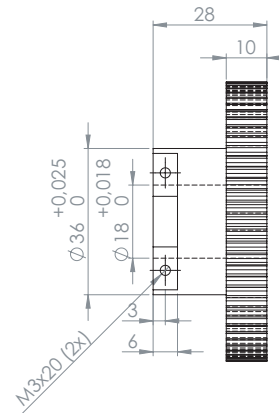
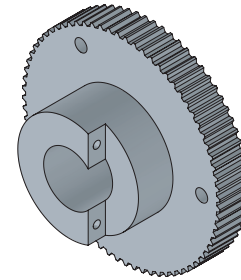
Figure D-1: Composition drawing of the steering- and handlebar assembly.





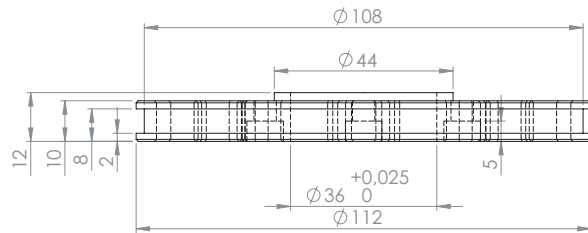
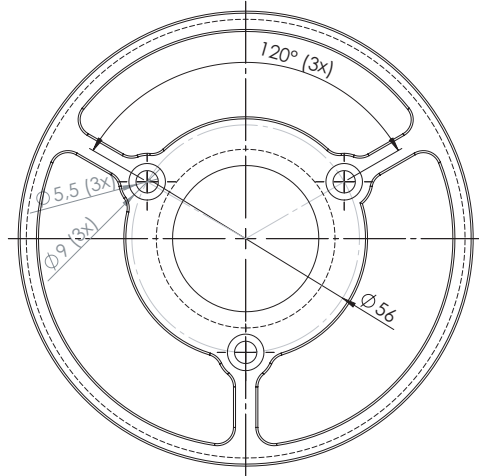
GEAR WHEEL: ANGST + PFISTER 09.1941.1480
TOLERANCES UNLESS OTHERWISE NOTED +0.5 mm

UNLESS OTHERWISE SPECIFIED: DIMENSIONS ARE IN MILLIMETERS		FINISH:		DEBUR AND BREAK SHARP EDGES		DO NOT SCALE DRAWING		REVISION	
SURFACE FINISH:		TOLERANCES:		LINEAR:		ANGULAR:		TITLE:	
DRAWN	NAME	SIGNATURE	DATE						
CHK'D									
APP'VD									
MFG									
Q.A				MATERIAL:		DWG. NO.	72gearslim		A4
				WEIGHT:		SCALE:1:1	SHEET 1 OF 1		



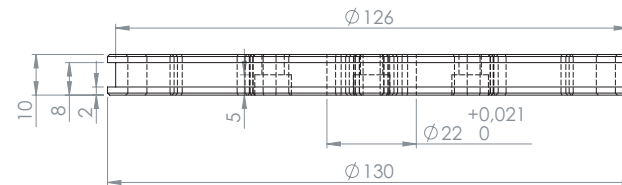
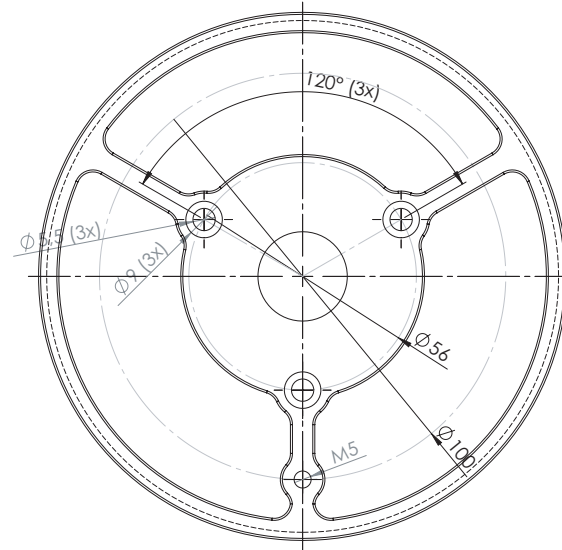
GEAR WHEEL: ANGST + PFISTER 09.1941.1480
TOLERANCES UNLESS OTHERWISE NOTED +0.5 mm

UNLESS OTHERWISE SPECIFIED: DIMENSIONS ARE IN MILLIMETERS		FINISH:		DEBUR AND BREAK SHARP EDGES		DO NOT SCALE DRAWING		REVISION	
SURFACE FINISH:		TOLERANCES:		LINEAR:		ANGULAR:		TITLE:	
DRAWN	NAME	SIGNATURE	DATE						
CHK'D									
APP'VD									
MFG									
Q.A				MATERIAL:		DWG. NO.	72large		A4
				WEIGHT:		SCALE:1:1	SHEET 1 OF 1		



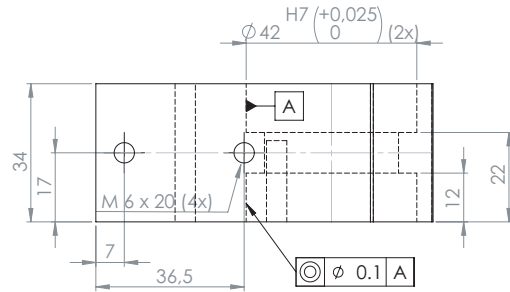
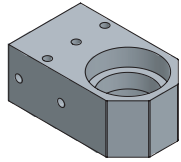
MATERIAL: ALUMINIUM $\varnothing 112 \times 12$ mm
 TOLERANCES UNLESS OTHERWISE NOTED ± 0.5 mm
 (CNC-machining)

UNLESS OTHERWISE SPECIFIED: DIMENSIONS ARE IN MILLIMETERS		FINISH:		DEBUR AND BREAK SHARP EDGES		DO NOT SCALE DRAWING		REVISION	
SURFACE FINISH:									
TOLERANCES:									
LINEAR:									
ANGULAR:									
NAME	SIGNATURE	DATE				TITLE:			
DRAWN									
CHKD									
APPVD									
MFG									
Q.A						MATERIAL:	DWG NO.	112gear50hole A4	
						WEIGHT:	SCALE:1:1	SHEET 1 OF 1	



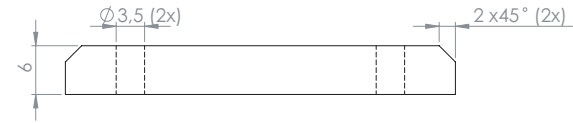
MATERIAL: ALUMINIUM $\varnothing 130 \times 12$ mm
 TOLERANCES UNLESS OTHERWISE NOTED ± 0.5 mm
 CNC-machining

UNLESS OTHERWISE SPECIFIED: DIMENSIONS ARE IN MILLIMETERS		FINISH:		DEBUR AND BREAK SHARP EDGES		DO NOT SCALE DRAWING		REVISION	
SURFACE FINISH:									
TOLERANCES:									
LINEAR:									
ANGULAR:									
NAME	SIGNATURE	DATE				TITLE:			
DRAWN									
CHKD									
APPVD									
MFG									
Q.A						MATERIAL:	DWG NO.	134gear22hole A4	
						WEIGHT:	SCALE:1:1	SHEET 1 OF 1	



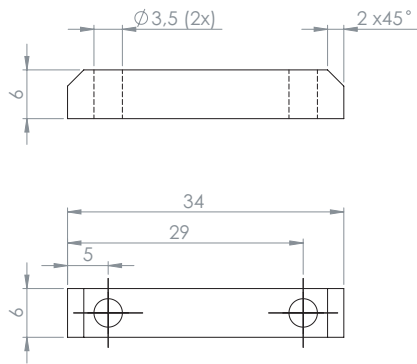
MATERIAL: ALUMINIUM 6082 T6 50x34x83 mm
TOLERANCES UNLESS OTHERWISE NOTED +0.5 mm

UNLESS OTHERWISE SPECIFIED: DIMENSIONS ARE IN MILLIMETERS		FINISH:		DEBUR AND BREAK SHARP EDGES		DO NOT SCALE DRAWING		REVISION	
SURFACE FINISH:									
TOLERANCES:									
LINEAR:									
ANGULAR:									
NAME	SIGNATURE	DATE				TITLE:			
DRAWN									
CHK'D									
APPV'D									
MFG									
Q.A									
					MATERIAL:	DWG NO.		bearing_clamp_v2 A4	
					WEIGHT:	SCALE:1:1		SHEET 1 OF 1	



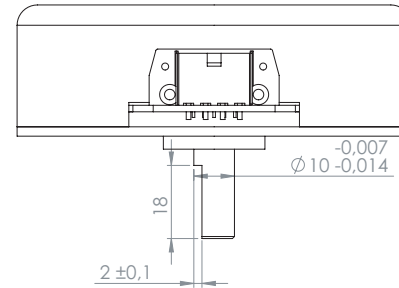
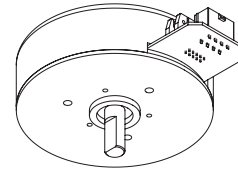
MATERIAL: STAINLESS STEEL 6x6x48 mm
TOLERANCES UNLESS OTHERWISE NOTED +0.5 mm

UNLESS OTHERWISE SPECIFIED: DIMENSIONS ARE IN MILLIMETERS		FINISH:		DEBUR AND BREAK SHARP EDGES		DO NOT SCALE DRAWING		REVISION	
SURFACE FINISH:									
TOLERANCES:									
LINEAR:									
ANGULAR:									
NAME	SIGNATURE	DATE				TITLE:			
DRAWN									
CHK'D									
APPV'D									
MFG									
Q.A									
					MATERIAL:	DWG NO.		clamp72gear A4	
					WEIGHT:	SCALE:2:1		SHEET 1 OF 1	

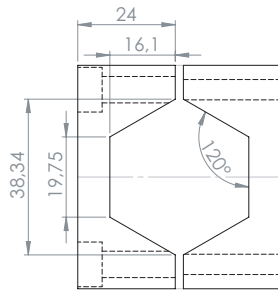
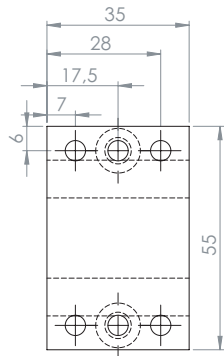
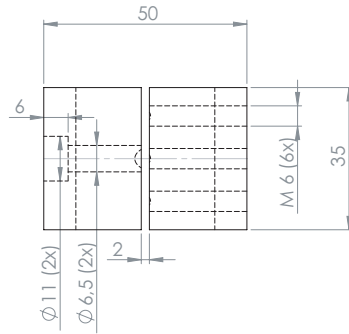
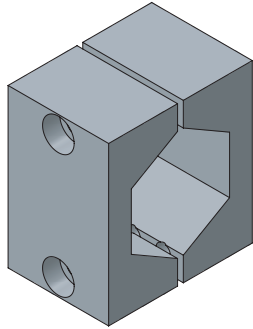


MATERIAL: STAINLESS STEEL 6x6x34 mm
 TOLERANCES UNLESS OTHERWISE NOTED ± 0.5 mm

UNLESS OTHERWISE SPECIFIED: DIMENSIONS ARE IN MILLIMETERS		FINISH:		DEBUR AND BREAK SHARP EDGES		DO NOT SCALE DRAWING		REVISION	
SURFACE FINISH:									
TOLERANCES:									
LINEAR:									
ANGULAR:									
NAME	SIGNATURE	DATE				TITLE:			
DRAWN									
CHK'D									
APPV'D									
MFG									
Q.A						MATERIAL:	DWG NO.	clamp72small A4	
						WEIGHT:	SCALE:2:1	SHEET 1 OF 1	

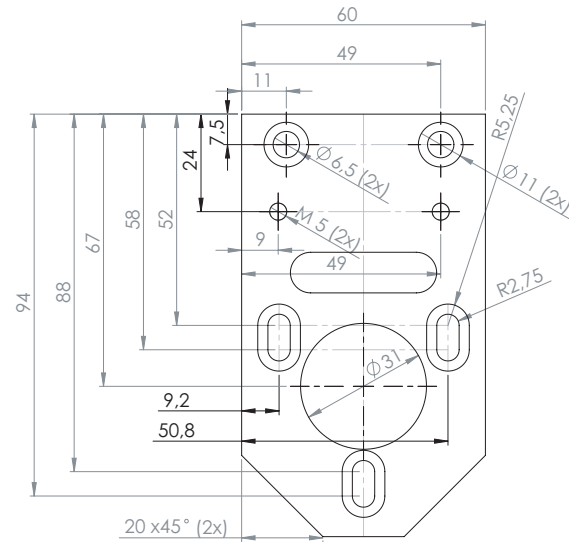
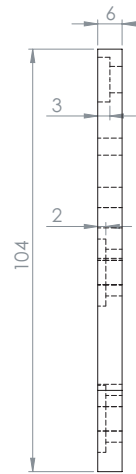


UNLESS OTHERWISE SPECIFIED: DIMENSIONS ARE IN MILLIMETERS		FINISH:		DEBUR AND BREAK SHARP EDGES		DO NOT SCALE DRAWING		REVISION	
SURFACE FINISH:									
TOLERANCES:									
LINEAR:									
ANGULAR:									
NAME	SIGNATURE	DATE				TITLE:			
DRAWN									
CHK'D									
APPV'D									
MFG									
Q.A						MATERIAL:	DWG NO.	ec90 A4	
						WEIGHT:	SCALE:1:2	SHEET 1 OF 1	



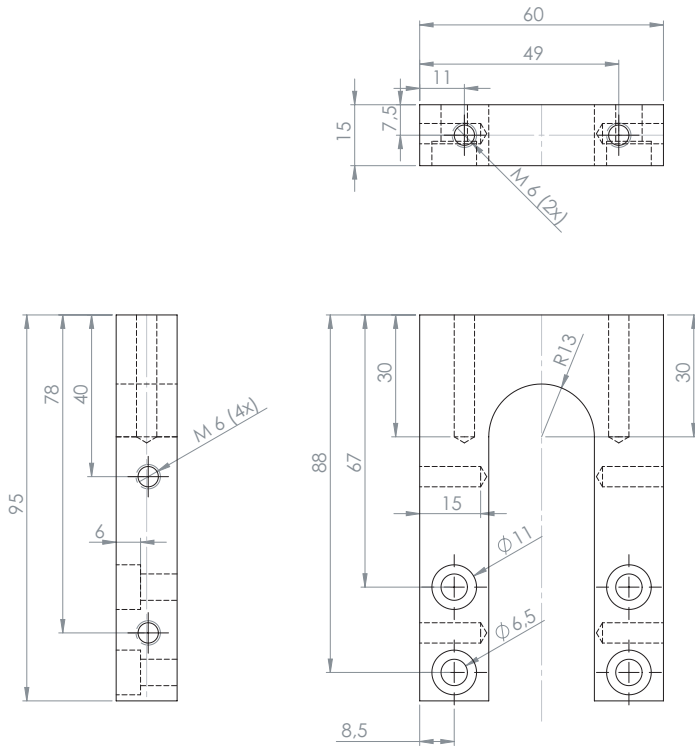
MATERIAL: ALUMINIUM 6082 T6 50x50x55 mm
TOLERANCES UNLESS OTHERWISE NOTED +0.5 mm

UNLESS OTHERWISE SPECIFIED: DIMENSIONS ARE IN MILLIMETERS		FINISH:		DEBUR AND BREAK SHARP EDGES		DO NOT SCALE DRAWING		REVISION	
SURFACE FINISH:									
TOLERANCES:									
LINEAR:									
ANGULAR:									
NAME	SIGNATURE	DATE				TITLE:			
DRAWN									
CHK'D									
APP'VD									
MFG									
Q.A						MATERIAL:	DWG NO.	front_bracket_v2 A4	
						WEIGHT:	SCALE:1:1	SHEET 1 OF 1	



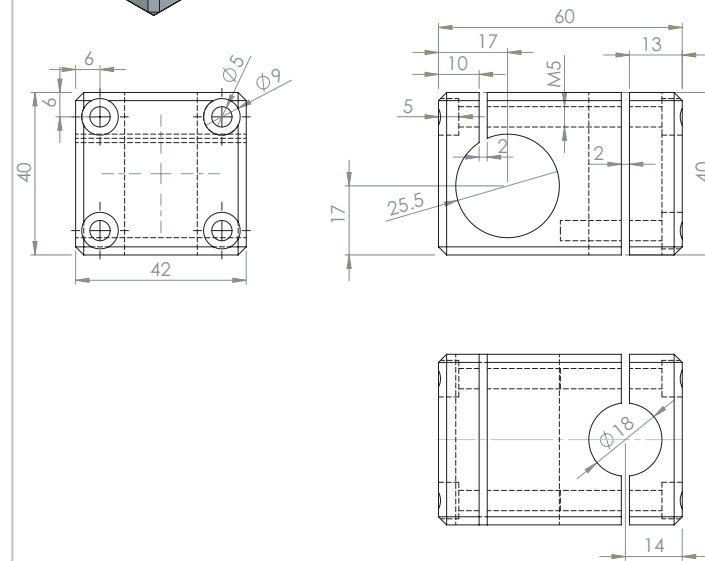
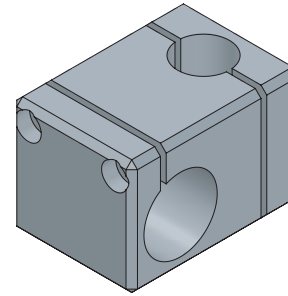
MATERIAL: ALUMINIUM 6060 T6 60x6x104 mm
TOLERANCES UNLESS OTHERWISE NOTED +0.5 mm

UNLESS OTHERWISE SPECIFIED: DIMENSIONS ARE IN MILLIMETERS		FINISH:		DEBUR AND BREAK SHARP EDGES		DO NOT SCALE DRAWING		REVISION	
SURFACE FINISH:									
TOLERANCES:									
LINEAR:									
ANGULAR:									
NAME	SIGNATURE	DATE				TITLE:			
DRAWN									
CHK'D									
APP'VD									
MFG									
Q.A						MATERIAL:	DWG NO.	front_motormount A4	
						WEIGHT:	SCALE:1:1	SHEET 1 OF 1	



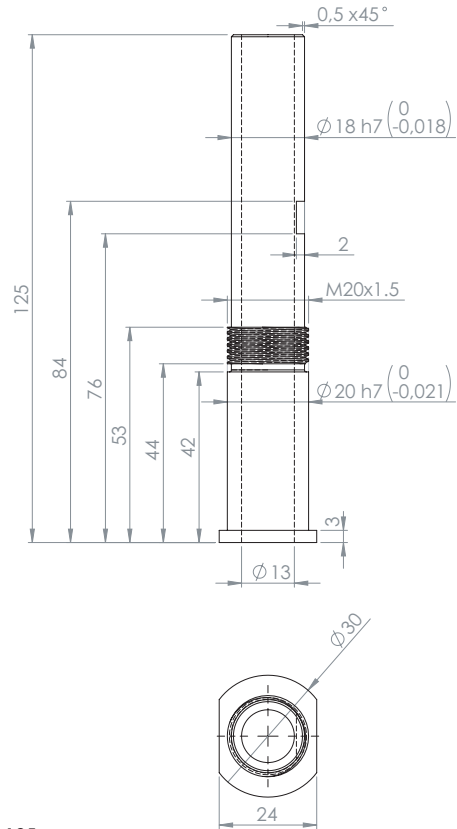
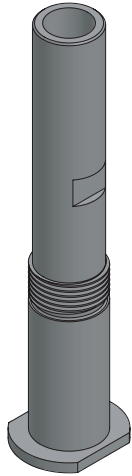
MATERIAL: ALUMINIUM 6060 T6 60x15x95 mm
TOLERANCES UNLESS OTHERWISE NOTED +0.5 mm

UNLESS OTHERWISE SPECIFIED: DIMENSIONS ARE IN MILLIMETERS		FINISH:		DEBUR AND BREAK SHARP EDGES		DO NOT SCALE DRAWING		REVISION	
SURFACE FINISH:									
TOLERANCES:									
LINEAR:									
ANGULAR:									
NAME		SIGNATURE		DATE		TITLE:			
DRAWN									
CHK'D									
APPV'D									
MFG									
Q.A									
				MATERIAL:		DWG NO. front_plate_fat		A4	
						SCALE:1:1		SHEET 1 OF 1	



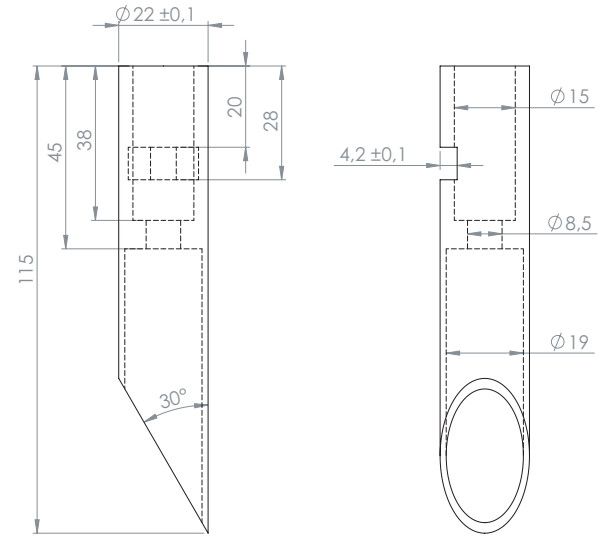
MATERIAL: ALUMINIUM 40x42x60 mm
TOLERANCES UNLESS OTHERWISE NOTED +0.5 mm

UNLESS OTHERWISE SPECIFIED: DIMENSIONS ARE IN MILLIMETERS		FINISH:		DEBUR AND BREAK SHARP EDGES		DO NOT SCALE DRAWING		REVISION	
SURFACE FINISH:									
TOLERANCES:									
LINEAR:									
ANGULAR:									
NAME		SIGNATURE		DATE		TITLE:			
DRAWN									
CHK'D									
APPV'D									
MFG									
Q.A									
				MATERIAL:		DWG NO. handlebar_clamp		A4	
						SCALE:1:1		SHEET 1 OF 1	



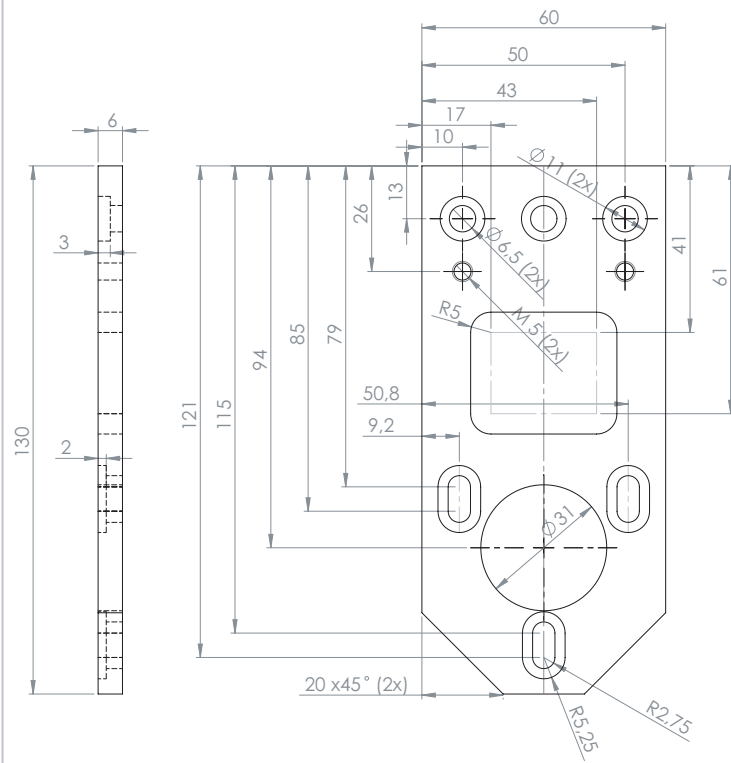
MATERIAL: STAINLESS STEEL Ø30x125 mm
TOLERANCES UNLESS OTHERWISE NOTED +/-0.5 mm

UNLESS OTHERWISE SPECIFIED: DIMENSIONS ARE IN MILLIMETERS		FINISH:		DEBUR AND BREAK SHARP EDGES		DO NOT SCALE DRAWING		REVISION	
SURFACE FINISH:									
TOLERANCES:									
LINEAR:									
ANGULAR:									
NAME	SIGNATURE	DATE				TITLE:			
DRAWN:									
CHK'D:									
APPV'D:									
MFG:									
Q.A.									
MATERIAL:					DWG NO. handlebar_pin_v2 A4				
WEIGHT:					SCALE:1:1 SHEET 1 OF 1				



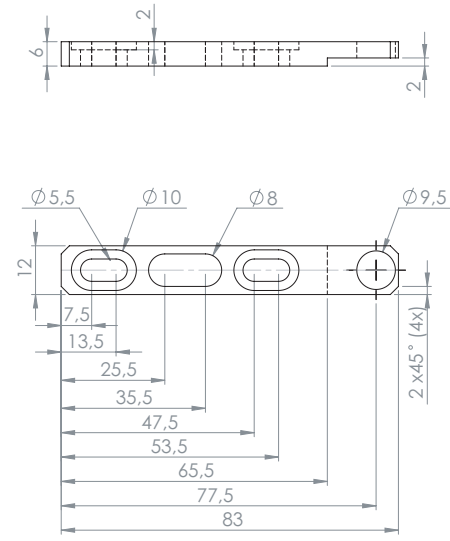
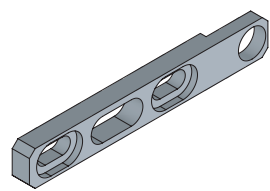
MATERIAL: STAINLESS STEEL Ø22.2x115 mm
TOLERANCES UNLESS OTHERWISE NOTED +/-0.5 mm

UNLESS OTHERWISE SPECIFIED: DIMENSIONS ARE IN MILLIMETERS		FINISH:		DEBUR AND BREAK SHARP EDGES		DO NOT SCALE DRAWING		REVISION	
SURFACE FINISH:									
TOLERANCES:									
LINEAR:									
ANGULAR:									
NAME	SIGNATURE	DATE				TITLE:			
DRAWN:									
CHK'D:									
APPV'D:									
MFG:									
Q.A.									
MATERIAL:					DWG NO. inner_steeringstem_v2				
WEIGHT:					SCALE:1:1 SHEET 1 OF 1				



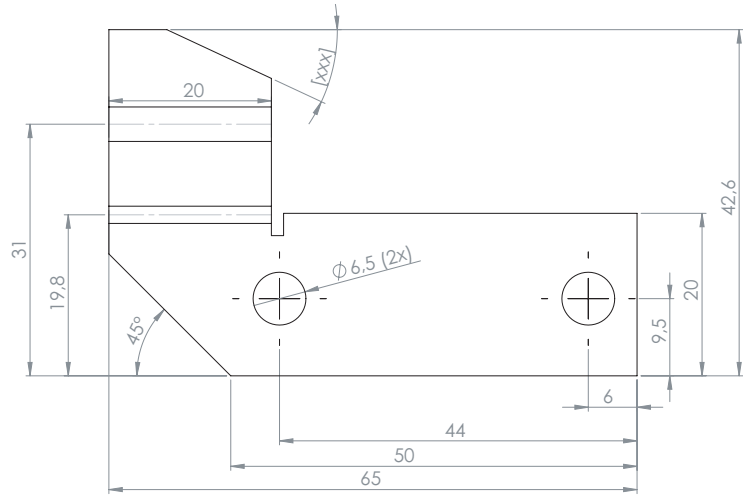
MATERIAL: ALUMINIUM 6060 T6 60x6x130 mm
 TOLERANCES UNLESS OTHERWISE NOTED +0.5 mm

UNLESS OTHERWISE SPECIFIED: DIMENSIONS ARE IN MILLIMETERS		FINISH:		DEBUR AND BREAK SHARP EDGES		DO NOT SCALE DRAWING		REVISION	
SURFACE FINISH:									
TOLERANCES:									
LINEAR:									
ANGULAR:									
NAME	SIGNATURE	DATE				TITLE:			
DRAWN:									
CHK'D:									
APP'VD:									
MFG:									
Q.A.						MATERIAL:	DWG NO.	rear_motormount A4	
						WEIGHT:	SCALE:1:1	SHEET 1 OF 1	



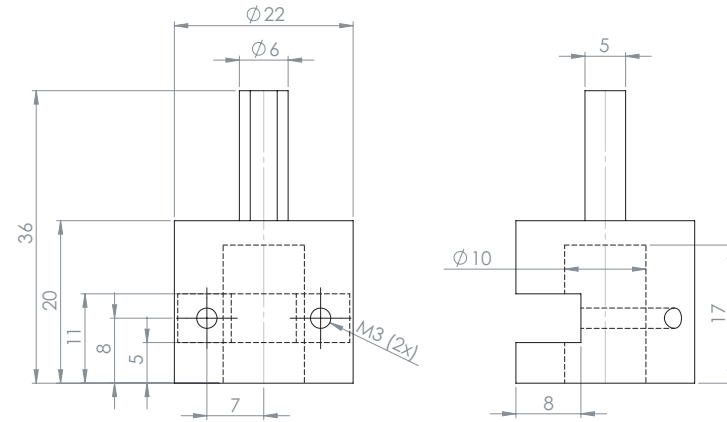
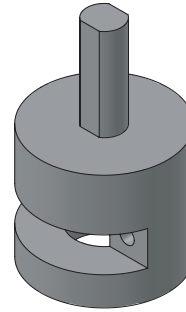
MATERIAL: ALUMINIUM 12x6x83 mm
 TOLERANCES UNLESS OTHERWISE NOTED +0.5 mm

UNLESS OTHERWISE SPECIFIED: DIMENSIONS ARE IN MILLIMETERS		FINISH:		DEBUR AND BREAK SHARP EDGES		DO NOT SCALE DRAWING		REVISION	
SURFACE FINISH:									
TOLERANCES:									
LINEAR:									
ANGULAR:									
NAME	SIGNATURE	DATE				TITLE:			
DRAWN:									
CHK'D:									
APP'VD:									
MFG:									
Q.A.						MATERIAL:	DWG NO.	sensor_bracket A4	
						WEIGHT:	SCALE:1:1	SHEET 1 OF 1	



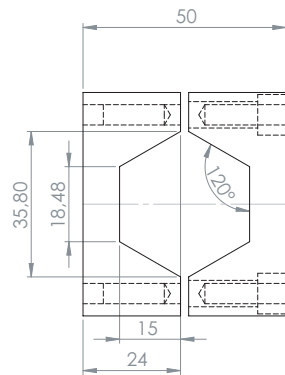
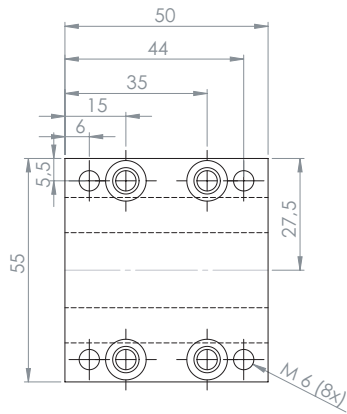
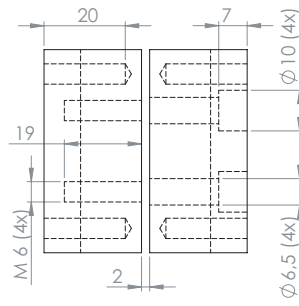
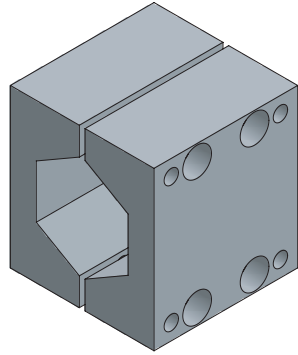
MATERIAL: ALUMINIUM 65x60x3 mm
 TOLERANCES UNLESS OTHERWISE NOTED +0.5 mm
 EXACT DIMENSIONS TO BE DETERMINED ON BICYCLE

UNLESS OTHERWISE SPECIFIED: DIMENSIONS ARE IN MILLIMETERS		FINISH:		DEBUR AND BREAK SHARP EDGES		DO NOT SCALE DRAWING		REVISION		
SURFACE FINISH:										
TOLERANCES:										
LINEAR:										
ANGULAR:										
NAME	SIGNATURE	DATE				TITLE:				
DRAWN										
CHK'D										
APPV'D										
MFG										
Q.A						MATERIAL:	DWG NO.	steerstop		A4
						WEIGHT:	SCALE:1:1	SHEET 1 OF 1		



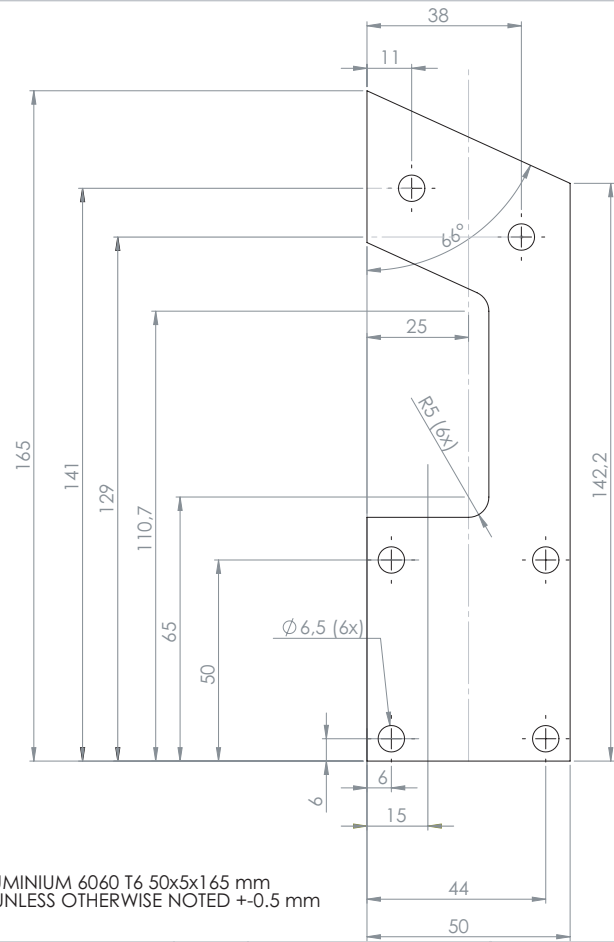
MATERIAL: STAINLESS STEEL Ø 22x36 mm
 TOLERANCES UNLESS OTHERWISE NOTED +0.5 mm

UNLESS OTHERWISE SPECIFIED: DIMENSIONS ARE IN MILLIMETERS		FINISH:		DEBUR AND BREAK SHARP EDGES		DO NOT SCALE DRAWING		REVISION		
SURFACE FINISH:										
TOLERANCES:										
LINEAR:										
ANGULAR:										
NAME	SIGNATURE	DATE				TITLE:				
DRAWN										
CHK'D										
APPV'D										
MFG										
Q.A						MATERIAL:	DWG NO.	stepdown		A4
						WEIGHT:	SCALE:2:1	SHEET 1 OF 1		



MATERIAL: ALUMINIUM 6082 T6 50x50x55
TOLERANCES UNLESS OTHERWISE NOTED +0.5 mm

UNLESS OTHERWISE SPECIFIED: DIMENSIONS ARE IN MILLIMETERS		FINISH:		DEBUR AND BREAK SHARP EDGES		DO NOT SCALE DRAWING		REVISION	
SURFACE FINISH:									
TOLERANCES:									
LINEAR:									
ANGULAR:									
DRAWN:		NAME		SIGNATURE		DATE		TITLE:	
CHK'D:									
APPV'D:									
MFG:									
Q.A:								MATERIAL:	
								DWG NO. top_bracket_v2	
								A4	
								WEIGHT:	
								SCALE:1:1	
								SHEET 1 OF 1	



MATERIAL: ALUMINIUM 6060 T6 50x5x165 mm
TOLERANCES UNLESS OTHERWISE NOTED +0.5 mm

UNLESS OTHERWISE SPECIFIED: DIMENSIONS ARE IN MILLIMETERS		FINISH:		DEBUR AND BREAK SHARP EDGES		DO NOT SCALE DRAWING		REVISION	
SURFACE FINISH:									
TOLERANCES:									
LINEAR:									
ANGULAR:									
DRAWN:		NAME		SIGNATURE		DATE		TITLE:	
CHK'D:									
APPV'D:									
MFG:									
Q.A:								MATERIAL:	
								DWG NO. v_plate	
								A4	
								WEIGHT:	
								SCALE:1:1	
								SHEET 1 OF 1	

Appendix E

Simulink firmware function-block layout

The following appendix shows the Simulink firmware layout of the steer-by-wire bicycle prototype.

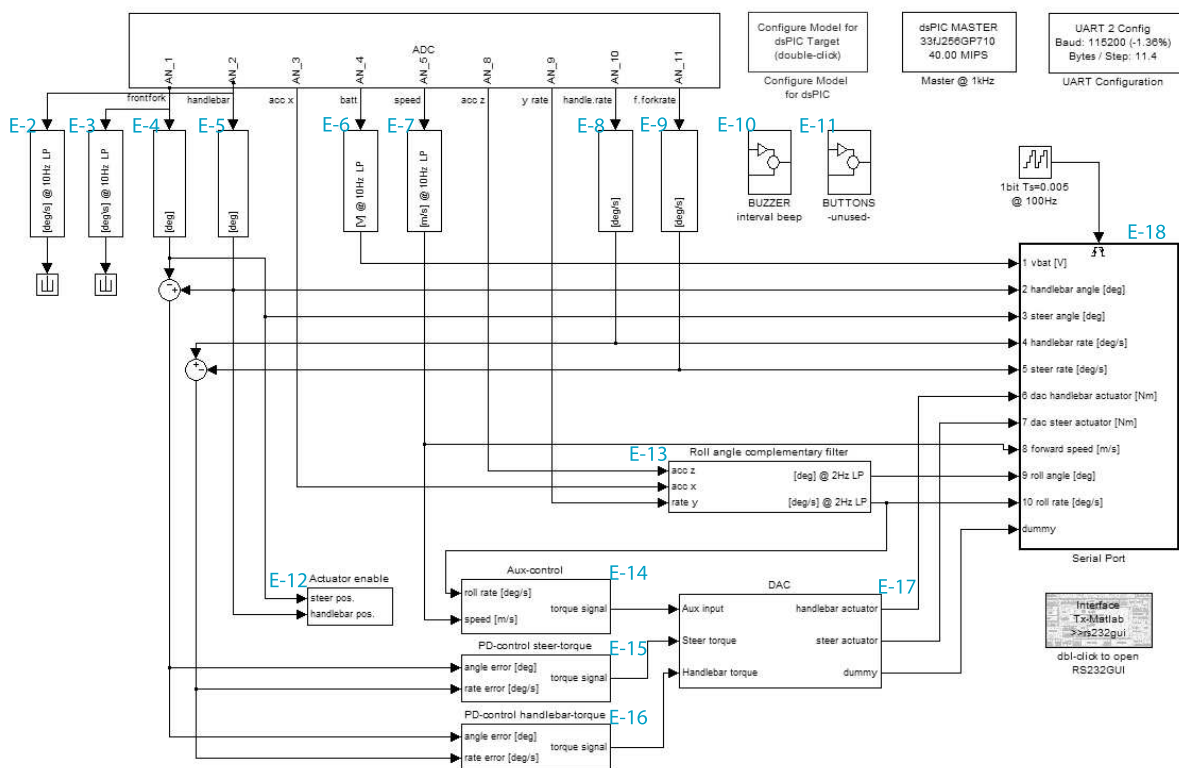


Figure E-1: The Simulink block diagram for the steer-by-wire bicycle prototype.

Figure E-1 shows the main firmware function-block layout, whereas individual subsystems or relevant system settings are shown in subsequent figures. Individual subsystems shown in figure E-1 are labeled according to the figures below.

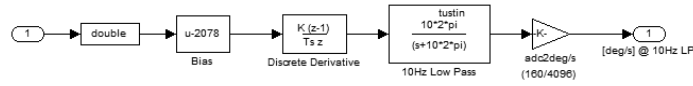


Figure E-2: Block diagram for the calculation of the handlebar rate by numerical differentiation.

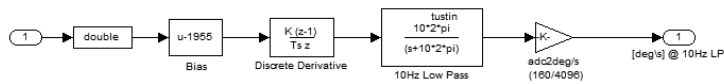


Figure E-3: Block diagram for the calculation of the steer rate by numerical differentiation.

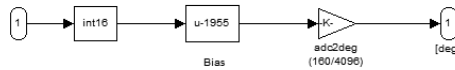


Figure E-4: Block diagram for the calculation of the steering angle.

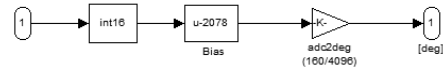


Figure E-5: Block diagram for the calculation of the handlebar angle.

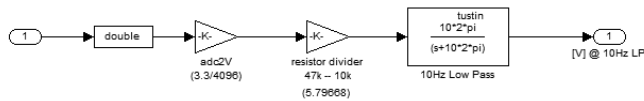


Figure E-6: Block diagram for the calculation of the battery voltage.

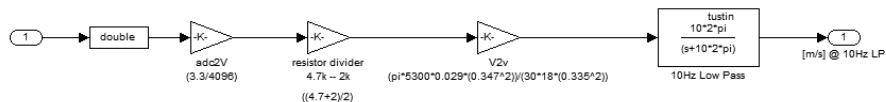


Figure E-7: Block diagram for the calculation of the forward speed.

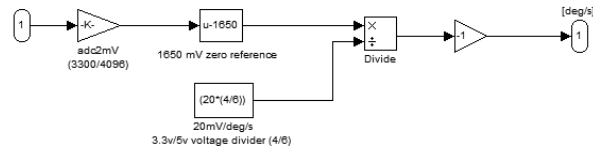


Figure E-8: Block diagram for interfacing with the handlebar rate sensor.

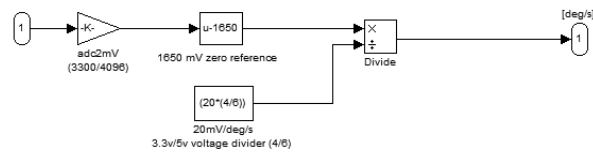


Figure E-9: Block diagram for interfacing with the steer rate sensor.



Figure E-10: Block diagram for interfacing with the audible buzzer.



Figure E-11: Block diagram for interfacing with the push buttons.

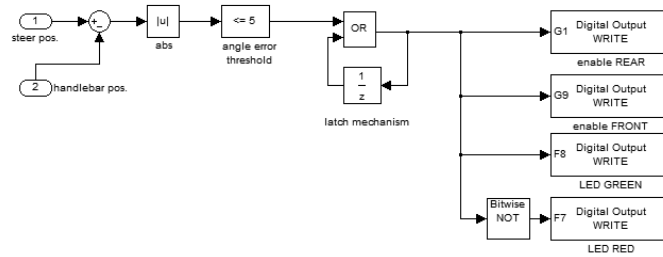


Figure E-12: Block diagram to set the enable threshold of the motor amplifiers during power-up.

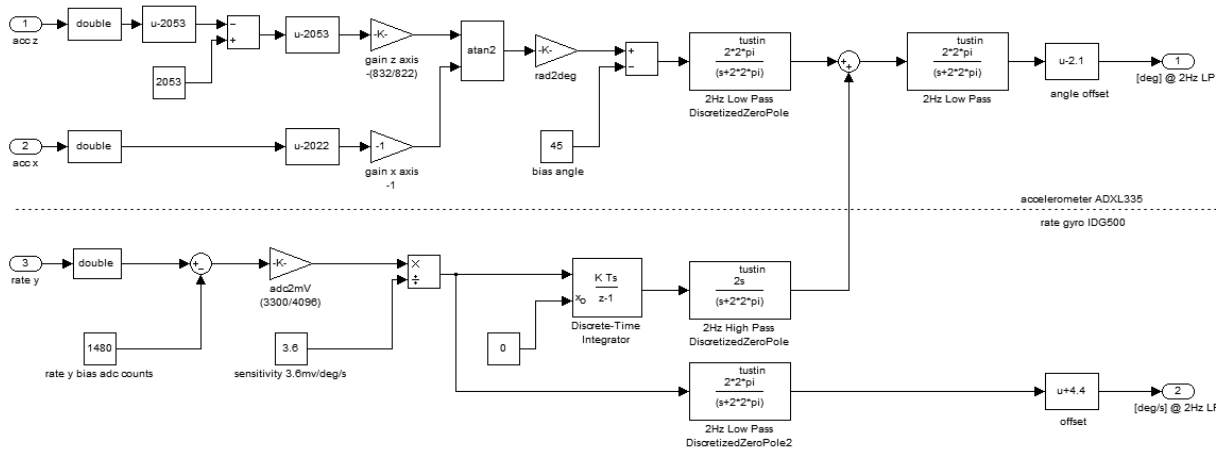


Figure E-13: Block diagram of the complementary filter to estimate the roll angle of the bicycle.

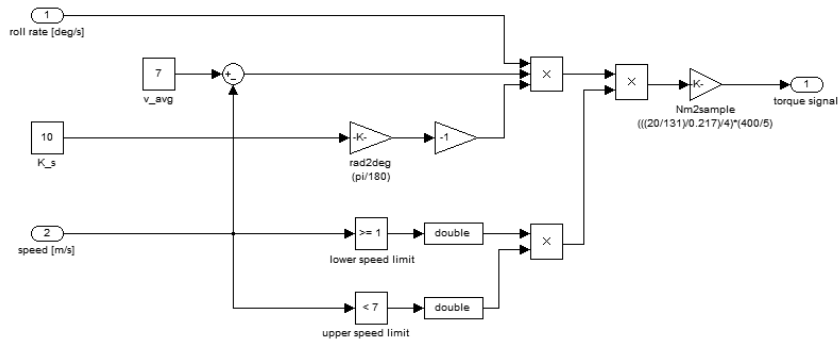


Figure E-14: Block diagram of the auxiliary stabilizing control structure.

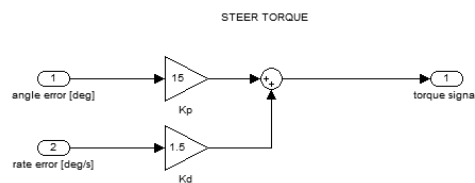


Figure E-15: Block diagram of the PD-control structure on the steering assembly.

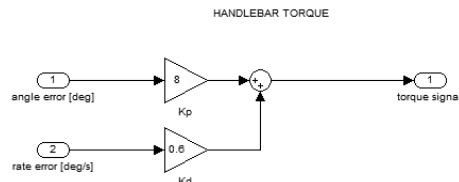


Figure E-16: Block diagram of the PD-control structure on the handlebar assembly.

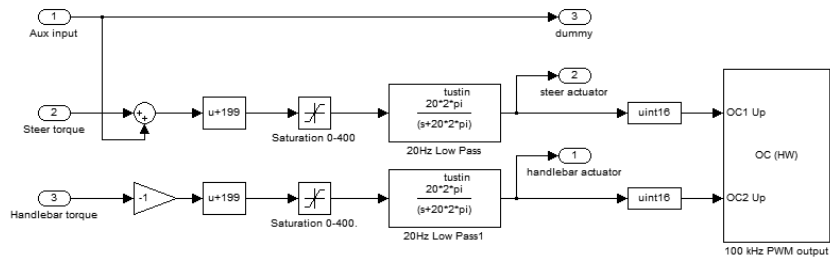


Figure E-17: Block diagram of the DAC output structure.

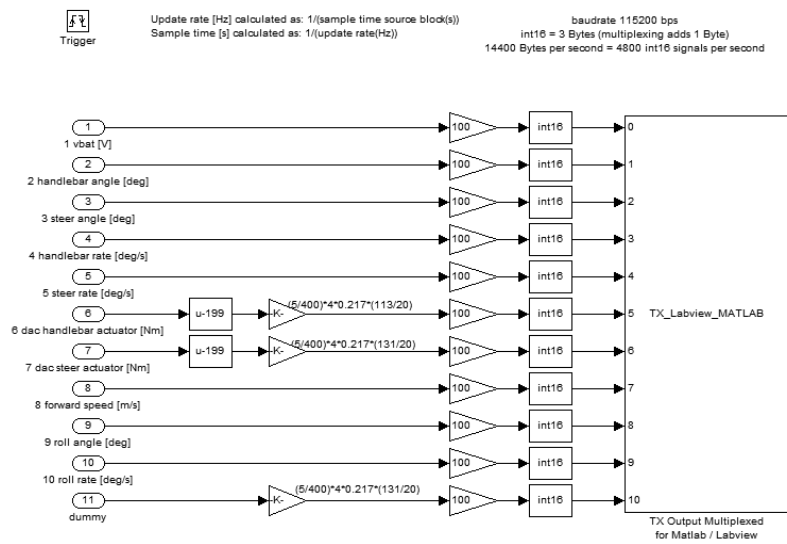


Figure E-18: Block diagram of the serial output for datalogging purposes.